

University of Texas at Arlington

**MavMatrix**

---

Bioengineering Dissertations

Department of Bioengineering

---

2023

## Lung cancer growth forecasting and classification models by machine learning using a novel 2D co-culture high throughput device

Adam Adrien Germain

Follow this and additional works at: [https://mavmatrix.uta.edu/bioengineering\\_dissertations](https://mavmatrix.uta.edu/bioengineering_dissertations)



Part of the [Biomedical Engineering and Bioengineering Commons](#)

---

### Recommended Citation

Germain, Adam Adrien, "Lung cancer growth forecasting and classification models by machine learning using a novel 2D co-culture high throughput device" (2023). *Bioengineering Dissertations*. 191.  
[https://mavmatrix.uta.edu/bioengineering\\_dissertations/191](https://mavmatrix.uta.edu/bioengineering_dissertations/191)

This Dissertation is brought to you for free and open access by the Department of Bioengineering at MavMatrix. It has been accepted for inclusion in Bioengineering Dissertations by an authorized administrator of MavMatrix. For more information, please contact [leah.mccurdy@uta.edu](mailto:leah.mccurdy@uta.edu), [erica.rousseau@uta.edu](mailto:erica.rousseau@uta.edu), [vanessa.garrett@uta.edu](mailto:vanessa.garrett@uta.edu).

**Lung cancer growth forecasting and classification models by machine learning  
using a novel 2D co-culture high throughput device**

by

Adam Germain

Presented to the Faculty of the Graduate School of

The University of Texas at Arlington in Partial Fulfillment

of the Requirements

for the Degree of

DOCTOR OF PHILOSOPHY IN BIOMEDICAL ENGINEERING

The University of Texas at Arlington

December 2023

## **Abstract**

### **Lung cancer growth forecasting and classification models by machine learning using a novel 2D co-culture high throughput device**

The University of Texas at Arlington, 2023

Supervising Professor: Dr. Young-Tae Kim.

Co-culture devices have commonly been used during in vitro experimentation to create therapeutic testing devices for lung cancer that more closely mimic the in vivo environment to gain better insights into new therapies and the reasons for inconsistency for current therapies. Moreover, AI (artificial intelligence) in the form of convolutional neural networks (CNN) and convolutional long-short term memory neural networks (convLSTM) are being used to classify, diagnose, and predict drug outcomes from the visual data provided by clinical imaging modalities, such as CT-scans, MRIs, or histopathological slides among others, or from numerical and textual data gathered from the genetic testing that has already improved clinical outcomes in the form of personalized medicine. Lung cancer is often found at late stages, so it is crucial to classify the subtype and then select the most effective therapies available for the patient in a timely manner, especially if the solutions can supplement the current standards of treatment without taxing the limited resources such as biopsy tissue. With these challenges in mind, I have created a 2D co-culture device that combines lung cancer and fibroblasts to study drug effects on the combination of cells in a high throughput manner, that is easily imaged due to the island of cancer cells formed in the center of the fibroblasts. When studying the high throughput drug screening I noticed that the cancer may be growing in patterns, so I developed a CNN model that, at this early stage, can classify between two cell lines (and subtypes) of lung cancer, A549 and H460 as early as 2 and 3 days of outgrowth. Beyond this, I co-developed a convLSTM model that can forecast lung cancer outgrowth over

fibroblasts utilizing the same 2D co-culture device. The machine learning model showed accurate reproduction of images matching the ground truth images and currently generated 5 to 10 days of forecasting images that agree with the growth extrapolation of the ground truth images.

## ACKNOWLEDGEMENTS

I would like to express my appreciation for the support my family and friends have given to me in the form of fun times, relaxation, venting, practice, and being sounding boards. I must also give thanks to my PI, Dr. Young-Tae Kim for being a wonderful mentor and collaborator, helping to prepare me for work and life after graduation through example and sound advice. Additionally, I wish to express my gratitude towards lab members Dr. Qionghua Shen and Dr. Joseph Wolf for introducing me to the lab techniques and the banter while working, towards Dr. Kytai Nguyen for running the NIHT32 program and supporting a great new group of PhD students, towards fellow graduate students Cynthia, Samira, Annie, Kelli, Tanveer, Alan, Scott, Phuc, and Mia for spending time outside the lab and helping relieve stress, and towards the undergraduates Giles, Anjani, Alexa, Sandra, and Bailey for making the lab more lively after my predecessors had graduated.

## CONTENTS

<b>ABSTRACT .....</b>	<b>II</b>
<b>ACKNOWLEDGEMENTS.....</b>	<b>IV</b>
<b>CHAPTER 1: MOTIVATIONS.....</b>	<b>1</b>
REFERENCES .....	8
<b>CHAPTER 2. CO-CULTURE DEVICE FOR IN VITRO HIGH THROUGHPUT ANALYSIS OF CANCER ASSOCIATED FIBROBLAST AND CANCER CELL INTERACTIONS.....</b>	<b>13</b>
ABSTRACT.....	14
INTRODUCTION.....	15
MATERIALS AND METHODS .....	18
RESULTS.....	22
DISCUSSION.....	30
ACKNOWLEDGEMENTS.....	31
AUTHOR CONTRIBUTIONS .....	32
REFERENCES .....	32
SUPPLEMENTARY MATERIAL .....	35
<b>CHAPTER 3: MACHINE LEARNING ENABLED CLASSIFICATION OF LUNG CANCER CELL LINES CO-CULTURED WITH FIBROBLASTS WITH LIGHTWEIGHT CONVOLUTIONAL NEURAL NETWORK FOR INITIAL DIAGNOSIS .....</b>	<b>36</b>
ABSTRACT.....	37
INTRODUCTION.....	38
MATERIALS AND METHODS .....	39
RESULTS.....	46
DISCUSSION.....	51
ACKNOWLEDGEMENTS.....	52
AUTHOR CONTRIBUTIONS .....	53
REFERENCES .....	53
<b>CHAPTER 4: FORECASTING ACCELERATED LUNG CANCER OUTGROWTH USING A CONVLSTM NEURAL NETWORK WITH A CO-CULTURED DEVICE FOR DATA COLLECTION.....</b>	<b>56</b>
ABSTRACT.....	57
INTRODUCTION.....	58
MATERIALS AND METHODS .....	60
RESULTS.....	68
DISCUSSION.....	77
ACKNOWLEDGEMENTS.....	79
AUTHOR CONTRIBUTIONS .....	79

REFERENCES .....	80
<b>CHAPTER 5: CONCLUSIONS AND FUTURE WORKS .....</b>	<b>83</b>
REFERENCES .....	86

## ***Chapter 1: Motivations***

Lung cancer continues to be the overall most deadly cancer because lung cancer is commonly uncovered at a late stage and the average age of diagnosis is around 70 years old [1,2]. The current standard of care treatments have become more personalized through improved classification of subtypes of lung cancer, including adenocarcinoma, squamous cell carcinomas, lung neuroendocrine carcinomas, large cell carcinoma, and small cell lung cancer and then further divisions of these subtypes for immunotherapy and other target treatments through more specific genetic testing protocols and yet the 73% of patients at diagnosis have a regional and distant level of spread and their 5-year survival is 35% and 8%, respectively [3,4]. These clinical outcomes demonstrate the need for increased drug screening, improved classification methods, and the ability to predict therapeutic results for patients.

In vitro co-culture devices have been a source of continual improvement for drug screening with researchers taking myriad approaches at striking the balance between increasing the complexity of system to more closely mimic in vivo conditions and maintaining the ability to both analyze and interpret the resulting data. There are several different strategies for the 2D, or two-dimensional, devices which tend to sacrifice realism in favor of simpler analysis and narrower focus. The simplest approach involves seeding the cancer cells and the chosen co-culture healthy cell type, following up with treatments, migration, or protein studies to determine how the cancer cells may be changing due to the specific healthy cell communication and interaction [5,6,7]. This approach can make it difficult to isolate the cancer cells and determine with specificity the cancer cell pathways that the healthy cells are impacting but can help gain more general information such as drug resistance modulation and migration speed changes. Researchers have used a different co-culture method to isolate paracrine signaling effects by seeding cancer cells and healthy cells in

separate areas and then circulating media between the two reservoirs or locations [7,8,9]. These studies have decreased the scope of the experimentation to better understand the generic communication effects healthy cells have on cancer cells. These are the two main types of 2D co-culture methods with some variations in technique based on the exact requirements of the study.

The three-dimensional, 3D, studies involve many different methods of co-cultures, often bespoke to labs and their research needs, but some have gained more widespread use. There are different scaffolds and gels with materials selection and construction of the devices designed with in vivo tissue features in mind such as stiffness, porosity, oxygenation, and pressure [10,11] while seeding the co-culture cancer and healthy cells in Matrigel remains a common strategy [12,13]. These systems maintain some controllability in the fact that the scaffolds are made in their own environment and then used for culturing, but synthetic materials can only mimic the natural environment to a limited extent. Instead of creating a synthetic scaffold, there are several techniques for creating ‘spheroids’ which involves the direct co-culture of two or more cell types, including cancer and at least one other healthy cell type [14]. These spheroids are created through the basic idea of not allowing the cells to contact any surface, besides other cells. The popular techniques are the hanging drop method, where cells are combined in a droplet of liquid, placed onto the lid, inverted, and suspended with higher humidity to prevent evaporation while the spheroid forms [15], utilizing repelling or “ultra-low attachment” surfaces that prevent cell adherence to the well-plate [16], or introducing magnetic nanoparticles into the spheroid cells and forcing them away from the well plate with magnetic force [17]. All the spheroid techniques can create valuable surrogate tumors, but there are many technical challenges with such culturing methods. The ratio of the different cells involved can cause instability on the spheroids, preservation and H&E staining on slices is the main method of analysis, and the all the techniques

require expense in the form of humidity control, unique well plates, or proprietary nanoparticles in the case of the magnetic method. These reasons are why 2D cell culture methods will remain relevant and continue to be improved upon, as nearly any facility can use the widely known protocols to run their own experiments.

For the co-cultures, there are a selection of healthy cell types that make up the tumor microenvironment including macrophages, epithelial cells, and fibroblasts among others with researchers selecting the combination that best suits their experimental goals [18]. Macrophages in the tumor microenvironment are correlated with poor survival outcomes due to increased tumor angiogenesis, metastasis, drug resistance, and ability to evade the body's immune response [19,20,21]. Endothelial cells tend to be associated with progression of tumors from their growth state into the more aggressive metastasis state [22]. Fibroblasts, on the other hand, are one of the major components of the tumor microenvironment and are associated with increasing cancer proliferation, angiogenesis, drug resistance, metastasis, and tumor formation while helping the cancer cells evade the immune system [23,24,25]. Many healthy cell types have value in co-culture with cancer cells for the study of the tumor microenvironment, but cancer associated fibroblasts are a compelling target for their abundance, ease of culturing in vitro, and their ability to create accelerated models by increasing cancer cell proliferation rates.

Discovering therapies that are effective at eliminating specific lung cancer subtypes with in vitro analysis requires the testing of numerous existing chemotherapeutics, repurposed drugs with FDA approval for other purposes, and novel therapeutics that are constantly being developed. Effectively testing every potential therapy against the wide array of heterogenous lung cancer cells necessitates high throughput drug screening, which is the use of automated equipment to run thousands, or even millions of tests in a short timeframe. High throughput screening is vital both

for finding lung cancer cell lines that are affected by drugs and for finding which treatments can impact patient specific lung cancers [26,27, 28]. These types of assays allow for unique discoveries with the widening of the potential therapy pool.

These improvements in the field of drug discovery combined with an ever-increasing focus on immunotherapies necessitates accuracy in classifying the lung cancer subtype for these specific treatments to be effective. Classification involves the morphological evaluation of lung cancer cells through light microscopy, histopathology, or cytopathology with the most straightforward differentiation being between non-small cell lung cancer (NSCLC) and small cell lung cancer (SCLC), the latter cells having a distinct oats-grain type shape, which is helpful because SCLC also tends to be the most aggressive in both growth rates and metastasis progression [3,29]. In some cases, patient samples do not contain enough cancer cells for histological classification, or the subtype identified by histology can benefit from an analysis of specific mutations that are exploitable for targeted therapies such as the adenocarcinoma subtype which may have epidermal growth factor receptor (EGFR), mitogen-activated protein kinases (MAPK), and phosphatidylinositol 3-kinases (PI3K) genomic alterations [3,30]. There remains some uncertainty in diagnosis for lung cancer subtypes, in part due to the expanding list of heterogenous categories within the original base subtypes where some treatments can completely eradicate one adenocarcinoma but also barely impact another variant [3].

There are many researchers investigating methods of improving the existing classification methods by taking advantage of various convolutional neural networks (CNNs) and training them on different clinical image data, such as histopathology slides and CT-scans. CNNs are particularly useful for image analysis due to their ability to not only map features but learn which features are important. CNNs function by passing filters over images to create feature maps, as can be seen in

Figure 1. The benefit of these CNNs is that they can learn features and patterns that the human eye cannot easily discern and consistently apply their rules to the classification task.

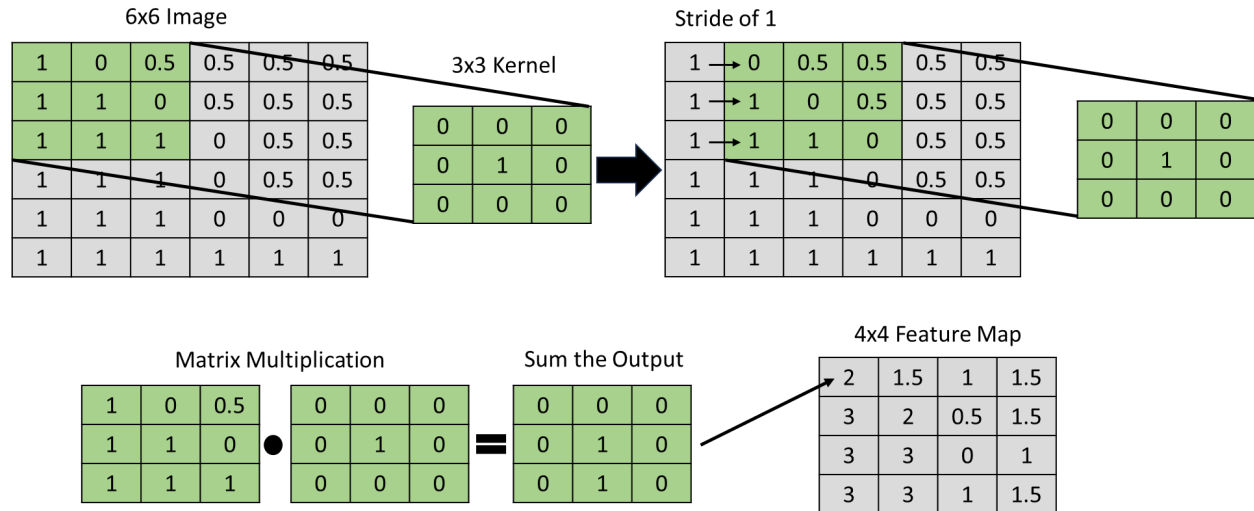


**Figure 1. Convolutional neural network basic function.** This diagram shows how convolutional blocks take the images which have been transformed into matrices of pixel values (typically normalized to 0 to 1 or -1 to 1) and then multiply smaller subsets of the image by a kernel or transformation filter to find features in the images such as edges and corners. While the kernel size is set in the model parameters, the filter itself is a variable within the CNN.

CT-scans are an interesting technology to combine with CNN learning, as the imaging modality is non-invasive and produces large amounts of data for analysis. The resulting CNN models have been able to establish the reliable diagnosis of normal, malignant, and benign tumors, but subtyping the lung cancer from CT-scans remains mostly out of reach with one study getting only achieve area under curve (AUC) of 0.71 at predicting adenocarcinoma from squamous cell carcinoma [31,32]. Histopathology slides are promising target, utilizing not only the morphology of the cells but also the intensity of the different stains in the analysis process with several studies achieving greater than 90% accuracy of classification on their datasets [33,34,35]. The struggle with machine learning and clinical data lies in the inability to aggregate a large dataset from which the CNNs can learn so that the results can be applied to a broader population.

Predicting therapeutic outcomes, such as recurrence and survival, is another avenue that can be aided by machine learning, especially time sensitive models such as long short-term memory (LSTM) neural networks which can be combined with CNNs to interpret image sequences and forms the convolutional long short-term memory (convLSTM) neural network. LSTM networks revolve around a cell which holds a hidden memory state that is updated at each time step by both forgetting old memory and storing new information and can be seen in Figure 2. The LSTM model learns how much information to forget, how much new information to store, and how much memory to utilize for the cell output. convLSTMs are the addition of convolutional blocks to the input so that image data can be used for the LSTM cell and thus it can predict pixel value changes over time.

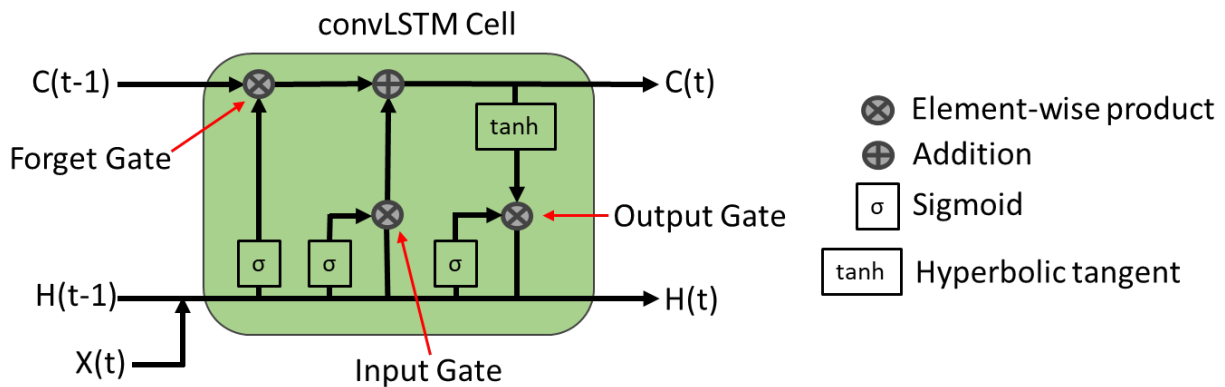


**Figure 2. A single long short-term memory cell.**  $C(t)$  is the hidden cell state,  $H(t)$  is the cell output, and  $X(t)$  is the cell input. The previous cell state  $C(t-1)$ , previous cell output  $H(t-1)$ , and the cell input  $X(t)$  determine the amount of information to remove in the forget gate, the amount of information from the input to add to the cell state in the input gate and how much information to output in the output gate. These gates utilize the sigmoid function to control the update function to the range of 0 to 1 so that, for example, 1 on the forget gate causes the cell to remember everything and 0 causes the cell to forget everything. All the functions contain learnable weights that the model adjusts over time to optimize its output.

Currently, LSTMs are being explored in different capacities regarding lung cancer with a few studies involving the detection of lung cancer in a classification model, the 3D reconstruction of

tumors from CT-scans, and predicting the development of tumors from irregular medical data over multiple patient visits [36,37,38] and other predicting the future disease prognosis and hospital stay lengths [39,40,41]. The creative uses for the LSTM architecture show that framing the problem and making sure the input is compatible with the model are important to getting the most out of machine learning.

As for convLSTMs, there are many more models that have been used for next frame prediction competitions than for lung cancer prognosis prediction [42]. The goal behind predictive studies using different models is to determine how a treatment will impact a patient's lung cancer in advance of seeing the tumor shrink, continue to grow, or recur. Studies tend to use drug binding site information [43], or lung cancer genetic data [44,45] to predict the outcome of a current treatment, but these models tend to result in binary results of whether a tumor recurrence will happen or whether a treatment will be effective or not, instead of the degree of effectiveness. One forecasting related study involves gathering 3D data from CT-scans over time to predict future volumes, but the dataset is only 33 patients [46], meaning much more work will have to go into data collection for the forecasting to reach relevant levels of generalization.

In the presented study, we created a 3D printed 2D co-culture well-plate holder with magnets that allows for distinct lung cancer and fibroblast seeding for high throughput drug screening. The device is easily made with inexpensive materials, can be customized for any size well-plate, and allows for simple quantification due to the convenient placement of the lung cancer cells in relation to the fibroblasts. Fibroblasts are important for making the tests more robust by adding a healthy cell type that can estimate healthy cell toxicity, increasing the resistance of the lung cancer cells, and by accelerating their growth to allow for quicker results. On top of this, the lung cancer cells grow in unique 2D patterns when surrounded by fibroblasts which can be exploited by a CNN to

classify the cancer cell subtype. We trained a lightweight CNN model that can classify between H460 large cell carcinoma and A549 squamous cell carcinoma cell lines at only 2 days of growth on our platform. Additionally, the cancer overgrowth pattern across the fibroblasts for 9 days was sufficient to train a convLSTM to recreate the last image of the sequence and even forecast the first 5 to 10 days of lung cancer outgrowth. A large benefit of this in vitro model is that vast amounts of data can be generated at any pace that the researcher's physical, technical, and supply capabilities allow, helping solve the problem of a dearth of clinical data. The different uses for the co-culture platform can allow for more rapid in vitro co-culture testing, improve lung cancer subtype classification, and forecast the degree of effectiveness of treatments on lung cancer within a short time frame.

For Chapter 4, Alex Sabol, the co-author for the convLSTM paper, did most of the work coding and testing the neural network and coding the artifact removal. We both worked equally on testing the rest of the data preparation and running the model. Adam Germain wrote the paper, collected the images, and analyzed the resulting data.

## References

1. Sung, H., Ferlay, J., Siegel, R. L., Laversanne, M., Soerjomataram, I., Jemal, A., & Bray, F. (2021). Global Cancer Statistics 2020: GLOBOCAN Estimates of Incidence and Mortality Worldwide for 36 Cancers in 185 Countries. *CA: A Cancer Journal for Clinicians*, 71(3), 209–249. <https://doi.org/10.3322/caac.21660>
2. Thandra, K. C., Barsouk, A., Saginala, K., Aluru, J. S., & Barsouk, A. (2021). Epidemiology of lung cancer. In *Wspolczesna Onkologia* (Vol. 25, Issue 1, pp. 45–52). Termedia Publishing House Ltd. <https://doi.org/10.5114/wo.2021.103829>
3. Nicholson, A. G., Tsao, M. S., Beasley, M. B., Borczuk, A. C., Brambilla, E., Cooper, W. A., Dacic, S., Jain, D., Kerr, K. M., Lantuejoul, S., Noguchi, M., Papotti, M., Rekhtman, N., Scagliotti, G., van Schil, P., Sholl, L., Yatabe, Y., Yoshida, A., & Travis, W. D. (2022). The 2021 WHO Classification of Lung Tumors: Impact of Advances Since 2015. In *Journal of Thoracic Oncology* (Vol. 17, Issue 3, pp. 362–387). Elsevier Inc. <https://doi.org/10.1016/j.jtho.2021.11.003>
4. State of Lung Cancer 2023 Report. (2023). <https://www.lung.org/getmedia/186786b6-18c3-46a9-a7e7-810f3ce4deda/SOLC-2023-Print-Report.pdf>

5. Prieto-García, E., Vanesa Díaz-García, C., Agudo-López, A., Pardo-Marqués, V., García-Consuegra, I., Asensio-Peña, S., Alonso-Riaño, M., Pérez, C., Gómez, C., Adeva, J., Paz-Ares, L., López-Martín, J. A., & Teresa Agulló-Ortuño, M. (2021). Tumor–stromal interactions in a co-culture model of human pancreatic adenocarcinoma cells and fibroblasts and their connection with tumor spread. *Biomedicines*, *9*(4). <https://doi.org/10.3390/biomedicines9040364>
6. Tong, H., Li, K., Zhou, M., Wu, R., Yang, H., Peng, Z., Zhao, Q., & Luo, K. Q. (2023). Coculture of cancer cells with platelets increases their survival and metastasis by activating the TGFβ/Smad/ PAI-1 and PI3K/AKT pathways. *International Journal of Biological Sciences*, *19*(13), 4259–4277. <https://doi.org/10.7150/ijbs.85986>
7. Phan, T. K. T., Shahbazzadeh, F., Pham, T. T. H., & Kihara, T. (2018). Alpha-mangostin inhibits the migration and invasion of A549 lung cancer cells. *PeerJ*, *2018*(6), 1–17. <https://doi.org/10.7717/peerj.5027>
8. Koukourakis, M. I., Kalamida, D., Mitrakas, A. G., Liouisia, M., Pouliliou, S., Sivridis, E., & Giatromanolaki, A. (2017). Metabolic cooperation between co-cultured lung cancer cells and lung fibroblasts. *Laboratory Investigation*, *97*(11), 1321–1331. <https://doi.org/10.1038/labinvest.2017.79>
9. Koh, B., Jeon, H., Kim, D., Kang, D., & Kim, K. R. (2019). Effect of fibroblast co-culture on the proliferation, viability and drug response of colon cancer cells. *Oncology Letters*, *17*(2), 2409–2417. <https://doi.org/10.3892/ol.2018.9836>
10. Unnikrishnan, K., Thomas, L. V., & Ram Kumar, R. M. (2021). Advancement of Scaffold-Based 3D Cellular Models in Cancer Tissue Engineering: An Update. In *Frontiers in Oncology* (Vol. 11). Frontiers Media S.A. <https://doi.org/10.3389/fonc.2021.733652>
11. Lewis, K. J. R., Hall, J. K., Kiyotake, E. A., Christensen, T., Balasubramaniam, V., & Anseth, K. S. (2018). Epithelial-mesenchymal crosstalk influences cellular behavior in a 3D alveolus-fibroblast model system. *Biomaterials*, *155*, 124–134. <https://doi.org/10.1016/j.biomaterials.2017.11.008>
12. Pan, H. J., Lee, C. W., Wu, L. Y., Hsu, H. H., Tung, Y. C., Liao, W. Y., & Lee, C. H. (2023). A 3D culture system for evaluating the combined effects of cisplatin and anti-fibrotic drugs on the growth and invasion of lung cancer cells co-cultured with fibroblasts. *APL Bioengineering*, *7*(1). <https://doi.org/10.1063/5.0115464>
13. Long, L., Yin, M., & Min, W. (2018). 3D Co-culture System of Tumor-associated Macrophages and Ovarian Cancer Cells. *BIO-PROTOCOL*, *8*(8). <https://doi.org/10.21769/bioprotoc.2815>
14. Rozenberg, J. M., Filkov, G. I., Trofimenko, A. v., Karpulevich, E. A., Parshin, V. D., Royuk, V. v., Sekacheva, M. I., & Durymanov, M. O. (2021). Biomedical Applications of Non-Small Cell Lung Cancer Spheroids. In *Frontiers in Oncology* (Vol. 11). Frontiers Media S.A. <https://doi.org/10.3389/fonc.2021.791069>
15. Amann, A., Zwierzina, M., Gamerith, G., Bitsche, M., Huber, J. M., Vogel, G. F., Blumer, M., Koeck, S., Pechriggl, E. J., Kelm, J. M., Hilbe, W., & Zwierzina, H. (2014). Development of an innovative 3D cell culture system to study tumour - Stroma interactions in non-small cell lung cancer cells. *PLoS ONE*, *9*(3). <https://doi.org/10.1371/journal.pone.0092511>
16. Vega, V. F., Yang, D., Jordán, L. O., Ye, F., Conway, L., Chen, L. Y., Shumate, J., Baillargeon, P., Scampavia, L., Parker, C., Shen, B., & Spicer, T. P. (2023). Protocol for

- 3D screening of lung cancer spheroids using natural products. *SLAS Discovery*, 28(2), 20–28. <https://doi.org/10.1016/j.slasd.2023.01.005>
17. Yaman, S., Anil-Inevi, M., Ozcivici, E., & Tekin, H. C. (2018). Magnetic force-based microfluidic techniques for cellular and tissue bioengineering. *Frontiers in Bioengineering and Biotechnology*, 6(DEC). <https://doi.org/10.3389/fbioe.2018.00192>
  18. el Harane, S., Zidi, B., el Harane, N., Krause, K. H., Matthes, T., & Preynat-Seauve, O. (2023). Cancer Spheroids and Organoids as Novel Tools for Research and Therapy: State of the Art and Challenges to Guide Precision Medicine. In *Cells* (Vol. 12, Issue 7). MDPI. <https://doi.org/10.3390/cells12071001>
  19. Cendrowicz, E., Sas, Z., Bremer, E., & Rygiel, T. P. (2021). The role of macrophages in cancer development and therapy. In *Cancers* (Vol. 13, Issue 8). MDPI. <https://doi.org/10.3390/cancers13081946>
  20. Bied, M., Ho, W. W., Ginhoux, F., & Blériot, C. (2023). Roles of macrophages in tumor development: a spatiotemporal perspective. In *Cellular and Molecular Immunology* (Vol. 20, Issue 9, pp. 983–992). Springer Nature. <https://doi.org/10.1038/s41423-023-01061-6>
  21. Kumari, N., & Choi, S. H. (2022). Tumor-associated macrophages in cancer: recent advancements in cancer nanoimmunotherapies. In *Journal of Experimental and Clinical Cancer Research* (Vol. 41, Issue 1). BioMed Central Ltd. <https://doi.org/10.1186/s13046-022-02272-x>
  22. Yang, D., Guo, P., He, T., & Powell, C. A. (2021). Role of endothelial cells in tumor microenvironment. *Clinical and Translational Medicine*, 11(6). <https://doi.org/10.1002/ctm2.450>
  23. Zhang, H., Yue, X., Chen, Z., Liu, C., Wu, W., Zhang, N., Liu, Z., Yang, L., Jiang, Q., Cheng, Q., Luo, P., & Liu, G. (2023). Define cancer-associated fibroblasts (CAFs) in the tumor microenvironment: new opportunities in cancer immunotherapy and advances in clinical trials. In *Molecular Cancer* (Vol. 22, Issue 1). BioMed Central Ltd. <https://doi.org/10.1186/s12943-023-01860-5>
  24. Wright, K., Ly, T., Kriet, M., Czirok, A., & Thomas, S. M. (2023). Cancer-Associated Fibroblasts: Master Tumor Microenvironment Modifiers. In *Cancers* (Vol. 15, Issue 6). Multidisciplinary Digital Publishing Institute (MDPI). <https://doi.org/10.3390/cancers15061899>
  25. Maia, A., & Wiemann, S. (2021). Cancer-associated fibroblasts: Implications for cancer therapy. In *Cancers* (Vol. 13, Issue 14). MDPI AG. <https://doi.org/10.3390/cancers13143526>
  26. Nair, N. U., Greninger, P., Zhang, X., Friedman, A. A., Amzallag, A., Cortez, E., Sahu, A. das, Lee, J. S., Dastur, A., Egan, R. K., Murchie, E., Ceribelli, M., Crowther, G. S., Beck, E., McClanaghan, J., Klump-Thomas, C., Boisvert, J. L., Damon, L. J., Wilson, K. M., ... Benes, C. H. (2023). A landscape of response to drug combinations in non-small cell lung cancer. *Nature Communications*, 14(1). <https://doi.org/10.1038/s41467-023-39528-9>
  27. Huang, L., Yi, X., Yu, X., Wang, Y., Zhang, C., Qin, L., Guo, D., Zhou, S., Zhang, G., Deng, Y., Bao, X., & Wang, D. (2021). High-Throughput Strategies for the Discovery of Anticancer Drugs by Targeting Transcriptional Reprogramming. In *Frontiers in Oncology* (Vol. 11). Frontiers Media S.A. <https://doi.org/10.3389/fonc.2021.762023>

28. Tuomainen, K., Hyytiäinen, A., Al-Samadi, A., Ianevski, P., Ianevski, A., Potdar, S., Turunen, L., Saarela, J., Kuznetsov, S., Wahbi, W., Risteli, M., Mäkitie, A., Monni, O., & Salo, T. (2021). High-throughput compound screening identifies navitoclax combined with irradiation as a candidate therapy for HPV-negative head and neck squamous cell carcinoma. *Scientific Reports*, *11*(1). <https://doi.org/10.1038/s41598-021-94259-5>
29. Semenova, E. A., Nagel, R., & Berns, A. (2015). *Origins, genetic landscape, and emerging therapies of small cell lung cancer*. <https://doi.org/10.1101/gad.263145>
30. Pao W, Girard N: New driver mutations in non-small-cell lung cancer. *Lancet Oncol* *12* (2): 175-80, 2011. [https://doi.org/10.1016/S1470-2045\(10\)70087-5](https://doi.org/10.1016/S1470-2045(10)70087-5)
31. Mohamed, T. I. A., Oyelade, O. N., & Ezugwu, A. E. (2023). Automatic detection and classification of lung cancer CT scans based on deep learning and ebola optimization search algorithm. *PLoS ONE*, *18*(8 AUGUST). <https://doi.org/10.1371/journal.pone.0285796>
32. Chaunzwa, T. L., Hosny, A., Xu, Y., Shafer, A., Diao, N., Lanuti, M., Christiani, D. C., Mak, R. H., & Aerts, H. J. W. L. (2021). Deep learning classification of lung cancer histology using CT images. *Scientific Reports*, *11*(1). <https://doi.org/10.1038/s41598-021-84630-x>
33. Anjum, S., Ahmed, I., Asif, M., Aljuaid, H., Alturise, F., Ghadi, Y. Y., & Elhabob, R. (2023). Lung Cancer Classification in Histopathology Images Using Multiresolution Efficient Nets. *Computational Intelligence and Neuroscience*, *2023*, 1–12. <https://doi.org/10.1155/2023/7282944>
34. Kanavati, F., Toyokawa, G., Momosaki, S., Takeoka, H., Okamoto, M., Yamazaki, K., Takeo, S., Iizuka, O., & Tsuneki, M. (2021). A deep learning model for the classification of indeterminate lung carcinoma in biopsy whole slide images. *Scientific Reports*, *11*(1). <https://doi.org/10.1038/s41598-021-87644-7>
35. Yang, J. W., Song, D. H., An, H. J., & Seo, S. B. (2022). Classification of subtypes including LCNEC in lung cancer biopsy slides using convolutional neural network from scratch. *Scientific Reports*, *12*(1). <https://doi.org/10.1038/s41598-022-05709-7>
36. Shaker, A. M., & Xiong, S. (2023). Lung Image Classification Based on Long-Short Term Memory recurrent neural network. *Journal of Physics: Conference Series*, *2467*(1). <https://doi.org/10.1088/1742-6596/2467/1/012007>
37. Hong, L., Modirrousta, M. H., Hossein Nasirpour, M., Mirshekari Chargari, M., Mohammadi, F., Moravvej, S. V., Rezvanishad, L., Rezvanishad, M., Bakhshayeshi, I., Alizadehsani, R., Razzak, I., Alinejad-Rokny, H., & Nahavandi, S. (2023). GAN-LSTM-3D: An efficient method for lung tumour 3D reconstruction enhanced by attention-based LSTM. *CAAI Transactions on Intelligence Technology*. <https://doi.org/10.1049/cit2.12223>
38. Wu, X., Wang, H. Y., Shi, P., Sun, R., Wang, X., Luo, Z., Zeng, F., Lebowitz, M. S., Lin, W. Y., Lu, J. J., Scherer, R., Price, O., Wang, Z., Zhou, J., & Wang, Y. (2022). Long short-term memory model – A deep learning approach for medical data with irregularity in cancer predication with tumor markers. *Computers in Biology and Medicine*, *144*. <https://doi.org/10.1016/j.combiomed.2022.105362>
39. Nunez, J. J., Leung, B., Ho, C., Bates, A. T., & Ng, R. T. (2023). Predicting the Survival of Patients With Cancer From Their Initial Oncology Consultation Document Using Natural Language Processing. *JAMA Network Open*, *6*(2), e230813. <https://doi.org/10.1001/jamanetworkopen.2023.0813>

40. Mei, X., Liu, Z., Singh, A., Lange, M., Boddu, P., Gong, J. Q. X., Lee, J., DeMarco, C., Cao, C., Platt, S., Sivakumar, G., Gross, B., Huang, M., Masseaux, J., Dua, S., Bernheim, A., Chung, M., Deyer, T., Jacobi, A., ... Yang, Y. (2023). Interstitial lung disease diagnosis and prognosis using an AI system integrating longitudinal data. *Nature Communications*, 14(1). <https://doi.org/10.1038/s41467-023-37720-5>
41. Alsinglawi, B., Alshari, O., Alorjani, M., Mubin, O., Alnajjar, F., Novoa, M., & Darwish, O. (2022). An explainable machine learning framework for lung cancer hospital length of stay prediction. *Scientific Reports*, 12(1). <https://doi.org/10.1038/s41598-021-04608-7>
42. Zhou, Y., Dong, H., & el Saddik, A. (2020). Deep Learning in Next-Frame Prediction: A Benchmark Review. In *IEEE Access* (Vol. 8, pp. 69273–69283). Institute of Electrical and Electronics Engineers Inc. <https://doi.org/10.1109/ACCESS.2020.2987281>
43. Qureshi, R., Basit, S. A., Shamsi, J. A., Fan, X., Nawaz, M., Yan, H., & Alam, T. (2022). Machine learning based personalized drug response prediction for lung cancer patients. *Scientific Reports*, 12(1). <https://doi.org/10.1038/s41598-022-23649-0>
44. Huang, R. X., Siritwanna, D., Cho, W. C., Wan, T. K., Du, Y. R., Bennett, A. N., He, Q. E., Liu, J. D., Huang, X. T., & Chan, K. H. K. (2022). Lung adenocarcinoma-related target gene prediction and drug repositioning. *Frontiers in Pharmacology*, 13. <https://doi.org/10.3389/fphar.2022.936758>
45. Luo R, Song J, Xiao X, Xie Z, Zhao Z, Zhang W, Miao S, Tang Y, Ran L. Identifying CpG methylation signature as a promising biomarker for recurrence and immunotherapy in non-small-cell lung carcinoma. *Aging* (Albany NY). 2020 Jul 28;12(14):14649-14676. doi: 10.18632/aging.103517. Epub 2020 Jul 28. PMID: 32723974; PMCID: PMC7425482.
46. Zhang, L., Lu, L., Wang, X., Zhu, R. M., Bagheri, M., Summers, R. M., & Yao, J. (2020). Spatio-Temporal Convolutional LSTMs for Tumor Growth Prediction by Learning 4D Longitudinal Patient Data. *IEEE Transactions on Medical Imaging*, 39(4), 1114–1126. <https://doi.org/10.1109/TMI.2019.2943841>

***Chapter 2. Co-culture device for in vitro high throughput analysis of cancer associated fibroblast and cancer cell interactions***

Adam Germain<sup>1</sup> and Young-Tae Kim, PhD<sup>1,2\*</sup>

<sup>1</sup>*Department of Bioengineering, University of Texas at Arlington, TX*

<sup>2</sup>*Department of Urology, University of Texas Southwestern Medical Center, Dallas, TX*

Short Title: Co-Culture for high throughput CAF and cancer interactions

Correspondence and Requests for materials should be addressed to:

\*Corresponding author:  
Young-Tae Kim, Ph.D.  
Department of Bioengineering  
500 UTA Blvd ERB244  
University of Texas at Arlington  
Arlington, TX 76010

E-mail : [ykim@uta.edu](mailto:ykim@uta.edu)  
Fax: 817-272-2251  
Phone: 817-272-5023

Keywords: H460, cancer associated fibroblasts, co-culture, high throughput

## **Abstract**

Cancers in general, and specifically lung cancer, continue to have low patient survival rates when the patient is at an advanced stage when diagnosed. It appears that the local environment, especially fibroblasts and their signaling molecules, tends to induce metastasis, increase cancer cell resistance to treatment, and aid in tumor growth rates. Since 3-D models quickly become too complex and/or expensive, and therefore rarely leave the lab they are developed in, it is interesting to develop a 2-D model that more closely mimics the clustered tumor formation and bulk interaction with a surrounding fibroblast environment.

In the present study, we utilize an off-the-shelf stereolithography 3-D printer, standard use well plates, magnets, and metallic tubes to create a customizable 2-D co-culture system capable of being analyzed quantitatively with staining and qualitatively with standard fluorescent/brightfield microscopy to determine cancer-fibroblast interactions while also being able to test chemotherapeutic drugs in a high-throughput manner with standard 96-well plates.

Comparisons from monoculture and co-culture growth rates shows that the presence of fibroblasts allows for significantly increased growth rates for H460 cancer. Additionally, viability of cancer cells can be quantified with simple cell staining methods and morphology and cell-cell interactions can be observed and studied.

The high throughput model demonstrates that boundary condition changes can be observed between cancer cells and fibroblasts based upon the different chemotherapeutics that have been administered.

## **Introduction**

Lung cancer is the third common cancer in occurrence behind skin cancer and breast cancer for women and prostate cancer for men in the United States but consists of 18% of all cancer deaths worldwide, making it the deadliest cancer [1,2,3]. While the progress in early detection and treatment combined with reduced rates of smoking are certainly helping, the problem will only improve so far for two factors – ‘vaping’ is creating a resurgence in smoking tobacco and other chemicals, especially in younger generations, and many people who develop lung cancer discover the cancer later in their lifespan and only find out when the cancer is already in stage III or IV of progression which is further along than most current treatments can handle [1,2]. Early detection for lung cancer is a promising target for research but the fact is that it is difficult to screen entire populations of people at or above 55 or even 65 years of age for a single type of cancer, so there needs to be further research into combating more aggressive versions of cancers to improve 5-year survival rates above their currently dismal percentages [2,3].

The objective of in-vitro cancer experimentation is to find a solution that both matches important aspects of the natural environment of the cancer and is relatively quick and simple to test so that meaningful results can be acquired as quickly as possible. One of the most important environmental characteristics to mimic is the combination of healthy fibroblasts and cancerous cells, and the effects of their communication. It is well established that tumor cells actively communicate with fibroblasts in their environment and the interactions between the two cell types cause greater cell growth and enhanced metastasis capabilities for the tumor cells [4,5,6]. There are studies that measured upregulation of Matrix Metalloproteinase 1 (MMP-1), Vascular Endothelial Growth Factor (VEGF), Glucose Transporter 1 (GLUT1) and others in different co-culture models demonstrating that the interactions between cancer and fibroblasts is based in some

commonly overexpressed factors in malignant tumors [6,7,8]. These malignant tumors are the deadliest, causing 86% of lung cancer patients diagnosed with distantly spread cancer to only have a 5% survival rate for 5-years [1,3]. The desire for rapid testing in a co-culture setting is to understand which drugs impact malignant tumors effectively and which drugs allow the healthy fibroblasts to survive and regrow. While there are many different proteins and pathways that need to be studied to elucidate interactions in greater detail, there is also a need to study effects of different therapeutics for these cancer models in parallel so that gains, even small ones, can be made for patient survival.

There are currently many different types of drug testing models available in both 2D and 3D. Models involving 2D testing tend to rely on mixed co-cultures or growth of one subtype followed by addition of a second after some days [9,10,11]. These methods show more of a scattered tumor model where single cells or small clusters are spread throughout the healthy fibroblast cell environment. While they do involve direct co-culture methods, standard tumors tend to grow from individual cells into large masses where they can accelerate their own malignancy with physical crowding causing excretion of specific proteins and the induction of epithelial to mesenchymal transition (EMT) [12,13]. Some researchers search for paracrine signaling and by separating the cell types in culture such as Boyden assays with trans-well inserts [14,15,16,17,18] or custom microfluid devices, allowing only media sharing with cyclic flow of media or manual switching of conditioned media [19,20]. These studies are helpful for understanding distance communication between fibroblasts and cancer cells and their results are simpler to quantify, but they lack any juxtacrine signaling taking place. Additionally, there have been attempts at creating more reliable scratch assay wound healing models that involve creating distinct spaces with polydimethylsiloxane (PDMS) inserts, but these studies have found that PDMS leaves a residue

on the surface of the well plates that significantly retards cell migration into the void after removal [21,22]. Models involving 3D testing can suffer from several different types of problems due mostly to the increasing complexity inherent in adding another dimension to the analysis. Some studies create 3D devices out of Matrigel or other novel scaffolds [23,24,25] or utilize a hanging-drop methods [12,26] of culture to generate spherical co-cultures. These devices require preparation of different scaffold materials and require increased processing, involving flow cytometry or fixing the cells and observing them outside of their live environment because 3D cultures can be difficult to image. There are magnetic microfluidic devices utilizing magnets both below and above the well plates and aim to create specific 2D patterns or 3D spherical cultures based upon prior incubation of cells with proprietary magnetic nanoparticles [26,27,28]. The magnetic devices are like those used in the proposed method but require proprietary nanoparticles and difficult media changes to create and preserve the 3D spherical structures that are grown [27,28]. While these studies are valuable to understanding different functions and features of cancer and healthy cell interactions in environments that are approaching in vivo conditions, the current 2D and 3D methods are lacking a high throughput method of quickly and simply understanding therapeutic interactions with both cancer and healthy cells simultaneously.

In the current study, we investigated the interactions between primary cell line human dermal fibroblast- $\alpha$  cells (HDF- $\alpha$ ) and epithelial lung cancer line cells (H460) in a 2D cell culture model involving simultaneous seeding of the cultures on a well plate holder embedded with magnets to create an island of H460 among the HDF- $\alpha$  via a metal tube so that we could determine the effects that migration, invasion, and cancer associated fibroblast (CAF) cell signaling would have upon various common therapeutic treatments. The importance of the well-plate holder and tube are that they enable an open space between the cell types during seeding but leave no residue behind that

might prevent the cells from crossing the boundary after the tube has been removed and they utilize any type of standard well plate so the system can be integrated into any machine that uses current well plate designs. This allows for drug studies to be initiated as early as 24 hours after initial seeding as the two cultures will have already made physical contact with each other.

## **Materials and Methods**

### *Cell Lines and Culture and Reagents*

The human dermal fibroblast  $\alpha$  (HDF- $\alpha$ ) and human NSCLC line NCI-H460 were purchased from ATCC and cultured in RPMI supplemented with 10% of Fetal Bovine serum with both cell lines grown in 37 °C and 5% CO<sub>2</sub>. The therapeutics Paclitaxel (Taxol, PHL89806), Doxorubicin (Dox, D1515), 5-Fluorouracil (5-FU, 343922), Chlorotoxin (CTX, C5238), Calcitriol (1086312), and Blebbistatin (203391) were purchased from Sigma-Aldrich. Anycubic Photon Mono and Anycubic 3D Printer 405nm SLA UV-Curing Resin purchased from Amazon. PDMS and curing agent purchased from ThermoFisher Scientific. CellTracker™ Orange CMTMR Dye (C2927) and Hoechst 33342 (H3570) purchased from ThermoFisher Scientific. Green Live/Dead Stain (6342) was purchased from Immunochemistry Technologies.

### *Device Design and Fabrication*

Lung tumor microenvironment involves a complex set of cells including endothelial cells, healthy epithelial cells, fibroblast cells, and immune cells. The co-culture devices were fabricated by utilizing stereolithography (SLA) resin 3D printing techniques, and poly (dimethyl siloxane) (PDMS) inserts for cell culture medium boundary were made with molding techniques.

A magnet embedded well plate holder was created in Solidworks design software utilizing the dimensions given online for standard 96-well, 12-well, and 6-well plates. A mock-up of the well

plate was utilized to determine if the dimensions of the holder would fit properly and if the magnets would be centered beneath each well. The magnet dimensions were measured, and slightly larger holes created in the holder to ensure a secure fit for each magnet. An AnyCubic Photon Mono resin 3D printer was utilized to create the modeled plate holder. They were set-up on a side and printed with a layer thickness of 0.05 mm, 6 bottom layers with exposure of 45 seconds, normal exposure time of 2 seconds, Z lift of 6mm, and Z lift speed of 4mm/second. No additional supports were required to generate a functional plate holder.

The PDMS inserts were created by first mixing a 10:1 ratio of polymer to curing agent, and then degassing under 500mmHg vacuum in a chamber for 30 minutes. After degassing, a silicon wafer was pre-heated on a hotplate to 75 C and the PDMS mixture was poured onto the wafer until approximately 5mm thick, then left for 2 minutes to allow any bubbles formed from pouring to be removed from the polymer. The silicon wafer was then transferred to a 150 C hotplate for 5min. Upon solidification, the wafer and PDMS were removed from the hotplate and allowed to cool for 2-5 min and the PDMS was cut out and peeled off the wafer in a single circular piece and allowed to cool and finish curing overnight. The following day, the PDMS was cut into roughly square pieces, smaller than the well sizes for the 6-well and 12-well plates, and each piece punched in the center with an 8mm diameter hole punch tool. The PDMS inserts had any larger contaminating material removed by tape and were immersed in 70% ethanol in an enclosed container for 30 min for sterilization. These were then taken into a hood and washed three times in sterile deionized water and allowed to dry inside the hood overnight before being placed into the well plates.

The co-culture device assembly requires the resin well plate-holder, the magnets to be inserted into the plate-holder, the PDMS inserts, and the metal tubes used to separate the different cell cultures for seeding. The PDMS inserts are not necessary for 96-well plates due to the small individual size

of the wells. The magnets are first placed into the magnet holder and the appropriate well plate is then placed on top of the holder. The PDMS inserts are then attached to the well plate such that the center of the hole punch aligns with the center of the magnet beneath the well followed by dropping the metal tubes onto the magnets. The PDMS inserts hold the cell culture medium and surrounding fibroblasts close to the metal tube where the cancer cells are seeded.

#### *Cell Area Measurements for growth comparisons*

Due to a lack of tracking dye retention, the HDF- $\alpha$ /H460 boundary area was utilized to estimate progressive growth over a 7-day long co-culture experiment. For this experiment, 12-well plates were prepared with sterilized PDMS boundary inserts, placed onto a magnet-holder plate, and one tube was set in the center of each well inside a biosafety cabinet. The cancer cells were stained with Texas Red cell tracker prior to seeding and were seeded at a rate of 5,000 cells/well inside the tube of each well plate. HDF- $\alpha$  cells were seeded at 20,000 cells/well on the outside of the wall of the tube and inside the PDMS insert. After allowing the cells to attach for 3 hours, the tubes and PDMS boundaries were carefully removed, and the 12-well plates were removed from the magnet holder devices. Day 0 pictures were taken at 2.5x magnification to verify that the boundary seeding was successful, and then 1mL of RPMI growth media was added to each well. The cells were tracked for 7 days with pictures taken once per day at both 2.5x and 10x magnification. For the first 3 days, the fluorescent area could be tracked and measured for the cancer area, but after this the fluorescent signal began to weaken. A distinct circular boundary formed between the H460 and HDF- $\alpha$  was utilized to measure the area of the main “tumor” progression in ImageJ software after combining the brightfield and fluorescent images.

#### *H460 and HDF- $\alpha$ Co-culture Drug Study*

A 96-well magnet holder was prepared with magnets, sterilized, and a 96-well plate was placed on top of the holder while inside a biosafety cabinet. The tubes were sterilized and placed on top of the magnets, inside the selected wells for the experiment. Using an  $n=4$ , the wells were seeded with 5,000 H460 cancer cells in  $3\mu\text{L}$  on the inside of the tube and 20,000 HDF- $\alpha$  healthy fibroblast cells in  $40\mu\text{L}$  outside of the tube. The cells were incubated for 3 hours at  $37^{\circ}\text{C}$  and 5%  $\text{CO}_2$  to allow for attachment to the well plate. The tubes were then carefully removed in the biosafety cabinet and then brightfield and fluorescent pictures were taken to verify correct seeding had occurred. Then the tubes were removed and  $200\mu\text{L}$  of fresh RPMI + 10% FBS growth media was added to each well and they were incubated for 24 hours. The following day brightfield and fluorescent images were taken of the cells and upon confirmation of the boundary formation, the media was refreshed with  $200\mu\text{L}$  of fresh media + DMSO for control and  $200\mu\text{L}$  of media plus DMSO plus one of the following drugs for each other condition: 50nM of Paclitaxel (Taxol),  $5\mu\text{M}$  of Doxorubicin (Dox),  $25\mu\text{M}$  of 5-Fluorouracil (5-FU), 300nM of Chlorotoxin (CTX),  $5\mu\text{M}$  of Calcitriol, or  $1\mu\text{M}$  of Blebbistatin. The cells were then incubated for 2 more days and with pictures taken every 24 hours of each well. Images were merged and adjusted for clarity in ImageJ software after being taken. Repeats of the experiment were done in a 48-well plate with  $500\mu\text{L}$  of fresh media/well, but were limited to the DMSO control, 50nM of Paclitaxel (Taxol),  $5\mu\text{M}$  of Doxorubicin (Dox),  $25\mu\text{M}$  of 5-Fluorouracil (5-FU), 300nM of Chlorotoxin (CTX) conditions. The  $n=4$ , CMTMR staining of H460 cancer cells prior to seeding, seeding values of H460 at 5000 cells/well in  $3\mu\text{L}$  and HDF- $\alpha$  at 20,000 cells/well in  $40\mu\text{L}$ , the duration of attachment, waiting 24 hours before adding drug conditions, and 48 hours incubation for imaging were maintained for the experiment. For cell counting after 48 hours, all conditions were stained with  $100\mu\text{L}$  of image media containing Hoechst at 1:1000 concentration (all cell stain) and Green Live/Dead Stain at

1:1000 concentration (dead cell stain) for 20 minutes. Then images were taken at 10x magnification at the center seeding location for all wells to cover the entire main “tumor” mass. Cells fluorescing blue, red, and green were counted as “dead” cancer cells and those with red and blue fluorescence were counted as total cancer cells via ImageJ particle analyzer with a low threshold to remove non-cell particles. Live cells were calculated and then averaged for each condition.

### *Statistics*

Statistical software R was used to generate statistical analysis. ANOVA and Tukey post hoc test was utilized to denote significant differences among multiple groups and a p-value of <0.05 was considered statistically significant.

## **Results**

### *Development of Low-Cost, Simple Co-culture device*

To solve the problems found in previous studies, making a device that could aid in the study of metastasis phenotype cancer, main tumor cancer cells, and healthy cells in one place appeared to be the solution. Since it is well studied that cancer associated fibroblasts (CAFs) can induce a metastasis-like phenotype on tumor cells, the idea came about to create an island of cancer surrounded by fibroblasts for a direct contact method of co-culturing and to help simplify the quantification of both cell types. The device shown in Figure 1 below is 3D printed from a standard, low-cost resin SLA printer that holds magnets in the indentations and can be easily customized for different sizes of magnet. The plate is designed so that standard well plates (from 6-well to 96-well) can be stably placed on top and the magnets will align with the center of each well plate. The location of the magnet allows magnetic, metallic tubes to be placed inside of the wells such that

they separate the plate into two distinct areas: center of the tube where the cancer cells are seeded and out of tube where fibroblasts (or other cells) are seeded. If needed for larger well plates, an additional PDMS or other device can be placed as an outer boundary to maintain a smaller distance between the healthy and cancer cells. The steps for use are as follows and can also be seen in Figure 1: First fill the magnet holder with magnets and then place the well-plate on top. Then place the desired outer boundary surrounding the magnet, but inside the well plate. Place the tubes on top of the magnet with the hole facing upwards. Seed the cancer cells inside the tube making sure to utilize an appropriate amount of carrying fluid, depending on the chosen tube size. Seed the healthy cells on the outside of the tube and then incubate for a few hours to give the cells time to attach. Carefully remove the tubes and any outer layer insert and then add the normal growth media for the cells. The cells used in the study can be transfected cells for ease of tracking, they can be differentially stained prior to seeding, or the cells can be fixed after the study and immunostained depending on the researcher's needs. From Figure 1 (E) you can see the distribution of cells, red for H460 and green for HDF- $\alpha$ , 3 hours after seeding and after removal of the tube and magnet holder. There are some cells that will move across the boundary, but the general boundary between the different cell types is kept distinct. The simplicity of the procedure, and approximate cost of ~\$200 for the materials to make one's own plates (including the purchase of a 3D printer) make this approach quite attractive.

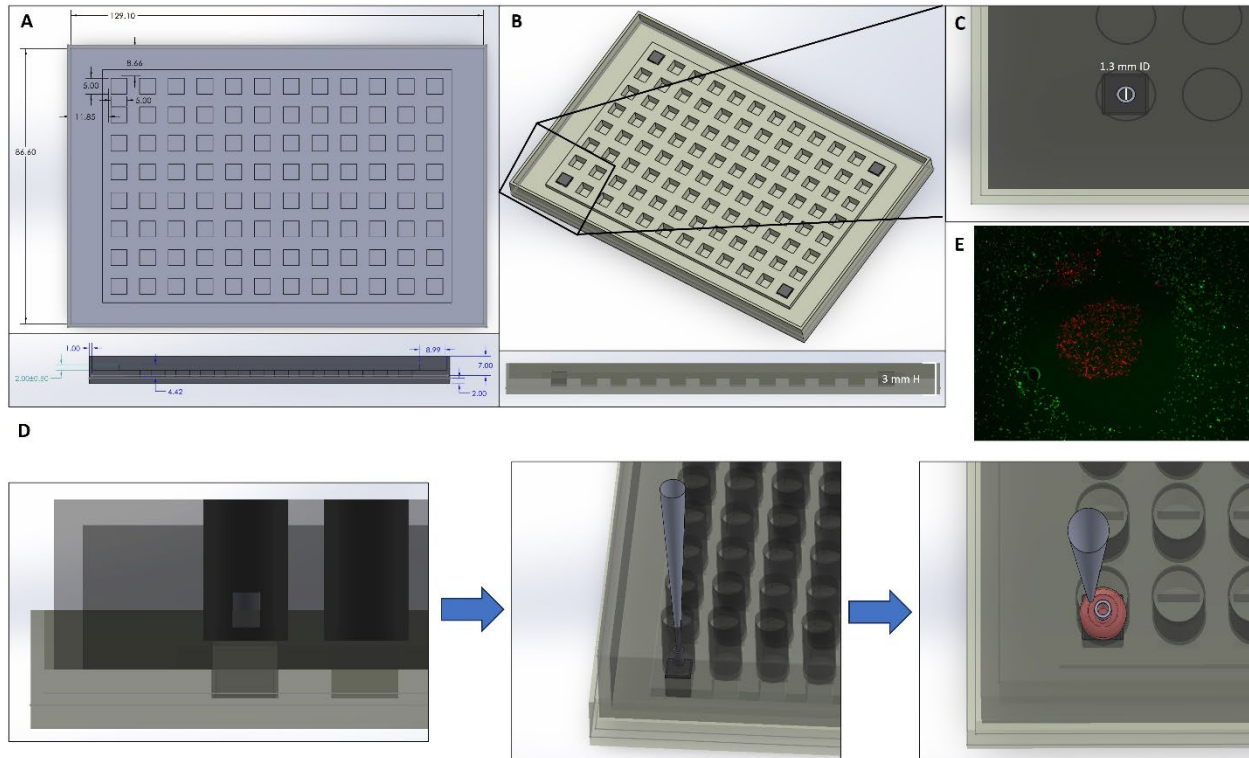


**Fig. 1. Design and Implementation of the 96-well plate holder magnetic co-culture device.** (a) Design and dimensions of well plate holder top and side view, measurements in millimeters. (b) Well plate holder with 4 small square magnets inserted to demonstrate fit and side view. (c) Enlarged view of a well with a tube secured inside of a well on top of a magnet showing that the magnet sits just below the bottom of the well plate and the tube is secured in the center of the well, from both a top and side view. (d) Demonstration of loading the inside and outside of the tube with a  $10\mu\text{L}$  pipette tip, example demonstrates  $3\mu\text{L}$  of seeding volume inside the tube and approximately  $40\mu\text{L}$  of seeding volume outside. (e) Fluorescent image taken 3 hours after seeding and removal of center tube. H460 lung cancer island (red) and HDF- $\alpha$  fibroblasts (green) with distinct space of separation between the two cultures.

### *Co-culture Accelerated Growth Model*

The first thing to note about Figure 2 is the full 360 cellular boundary formed between the H460 and HDF- $\alpha$  within 24 hours of seeding. The quick crossing of the open space between the two cell types shows that neither the magnetic approach nor the tube used for separation hinder cell motility. The growth of the H460 ‘tumor’ mass was measured over 7 total days taking advantage of the distinct ring formed by the H460 cells at the contact point with the HDF- $\alpha$  and demonstrated that

the with this model, the main mass of cancer quickly radiates outward with some satellite colonies forming clusters farther from the center mass. Figure 2 (B) shows the beginning stages of an S-curve growth pattern, expected for unchecked cancer growth in favorable conditions. The area measurement method is useful for obtaining a general impression of the cancer’s survivability in various conditions, comparable to the measurements of tumor mass in subcutaneous studies with immunocompromised mice, and the cells can be fixed and stained after such longer-term studies to confirm the extent of growth and survivability of both the healthy and cancer cells. The supplemental Figure 1 shows zoomed in images of the boundary over time. From these closer images, it can be observed that the H460 cancer cells contain both round tumor-like cells and elongated mesenchymal-like cells within the mass.

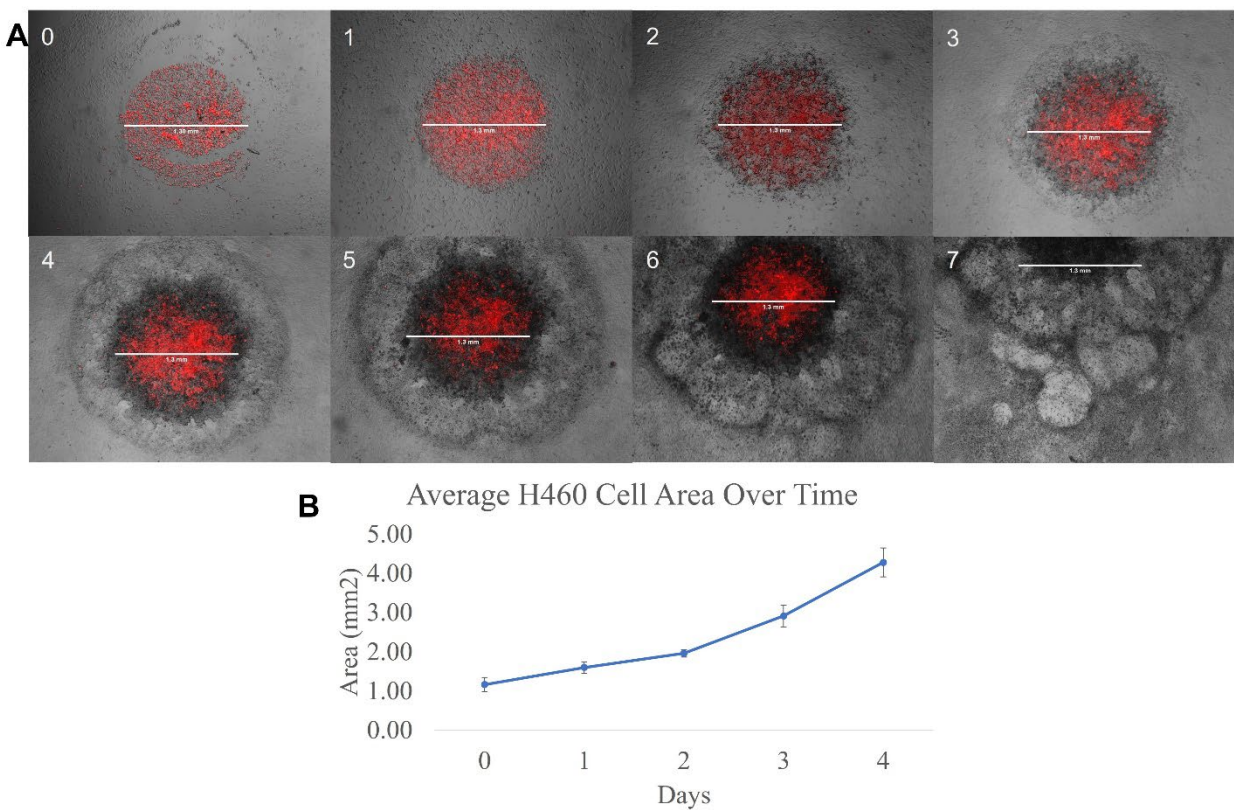


**Fig. 2. Progression of H460 lung cancer cells surrounded by HDF- $\alpha$  fibroblast cells over 7 days.** (a) Picture 0 taken 3 hours after seeding, other pictures taken daily starting 24 hours after picture 0 and ending on day 7. Red area is cell tracking dye CMTMR given to H460 cancer cells

prior to seeding and enhanced in ImageJ after fluorescent microscopy. **(b)** Average cell area measured in ImageJ from the left to the right edges of the main cancer mass over the first four days, scale bars are 1.3mm, the inner diameter of the metal tube used for separation during seeding.

### *Fibroblast and Cancer Cell Interaction*

Enhanced growth for cancer in the presence of fibroblasts found in other studies can be confirmed in this study. Seen in Figure 3, HDF- $\alpha$  increased the growth rate of the H460 cancer cells as the average island tumor mass in the co-culture device grew larger by 7% and 18% than the cancer cells grown by themselves, after normalizing for initial seeding differences. The increased growth and evident metastasis zones seen in Figure 2 Day 7 indicate that the co-culture mimics the effects seen by numerous other researchers, particularly the boosted growth and increased metastasis phenotype-like cancer cells. Under standard conditions, H460 cancer cells prefer to maintain cell to cell contact during their growth with very few cells moving away from the initial cancer mass which slows down the spread. However, H460 cancer cells robustly outgrew over the surrounding fibroblasts in the co-culture wells (Figure 2b).

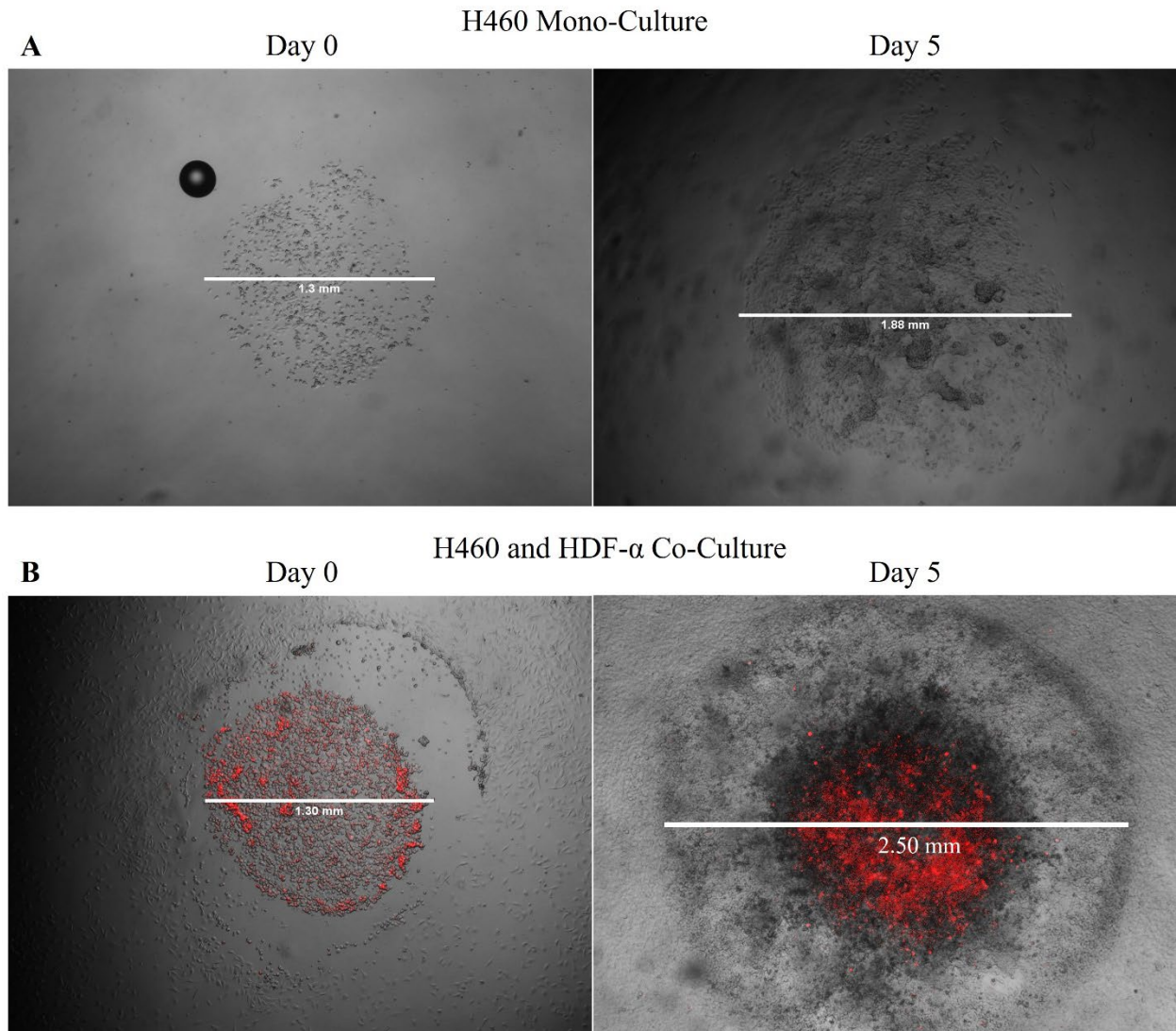


**Fig. 3. Comparison of 5 days of growth for monoculture H460 lung cancer with co-culture H460 lung cancer and HDF- $\alpha$ .** (a) Monoculture not stained and seeded at a density of 3,000 cells per well. (b) Co-culture H460 stained with CMTMR cell tracker prior to seeding and seeded at 5,000 cells per well and HDF- $\alpha$  not stained and seeded at 20,000 cells per well. Doubling time and expected area ratio normalized between the two seeding conditions. Brightfield images and fluorescent images adjusted in ImageJ.

### *Co-culture Drug Study*

A panel of drugs was selected from common anti-cancer agents to drugs that may see some use in combination therapies and included a single dose in the IC(50) range for Paclitaxel (Taxol), Doxorubicin (Dox), 5-Fluorouracil (5-FU), and Chlorotoxin (CTX). The viability chart in Figure

4b below show the H460 viability results of the 48hr drug study. Dox showed the greatest amount of cell death, but both populations of H460 and HDF- $\alpha$  cells can be seen to be suffering in the bright field image of Figure 4A. 5-FU reduced cancer cell viability by 75%, but healthy HDF- $\alpha$  cells can be seen in the brightfield image with intact nuclei, indicating that, while not as prolific as control, 5-FU may not be as universally toxic. Both Taxol and CTX mildly reduced cancer cell viability (not significantly), but clearly changed the boundary as a thinner fibroblast layer surrounding the central 'tumor' mass can be seen in the respective brightfield images. The speed of the boundary formation between the H460 and HDF- $\alpha$  cells demonstrates that the drug screening can be used for rapid determination of efficacy and quantified with differential staining protocols and cell counting procedures.

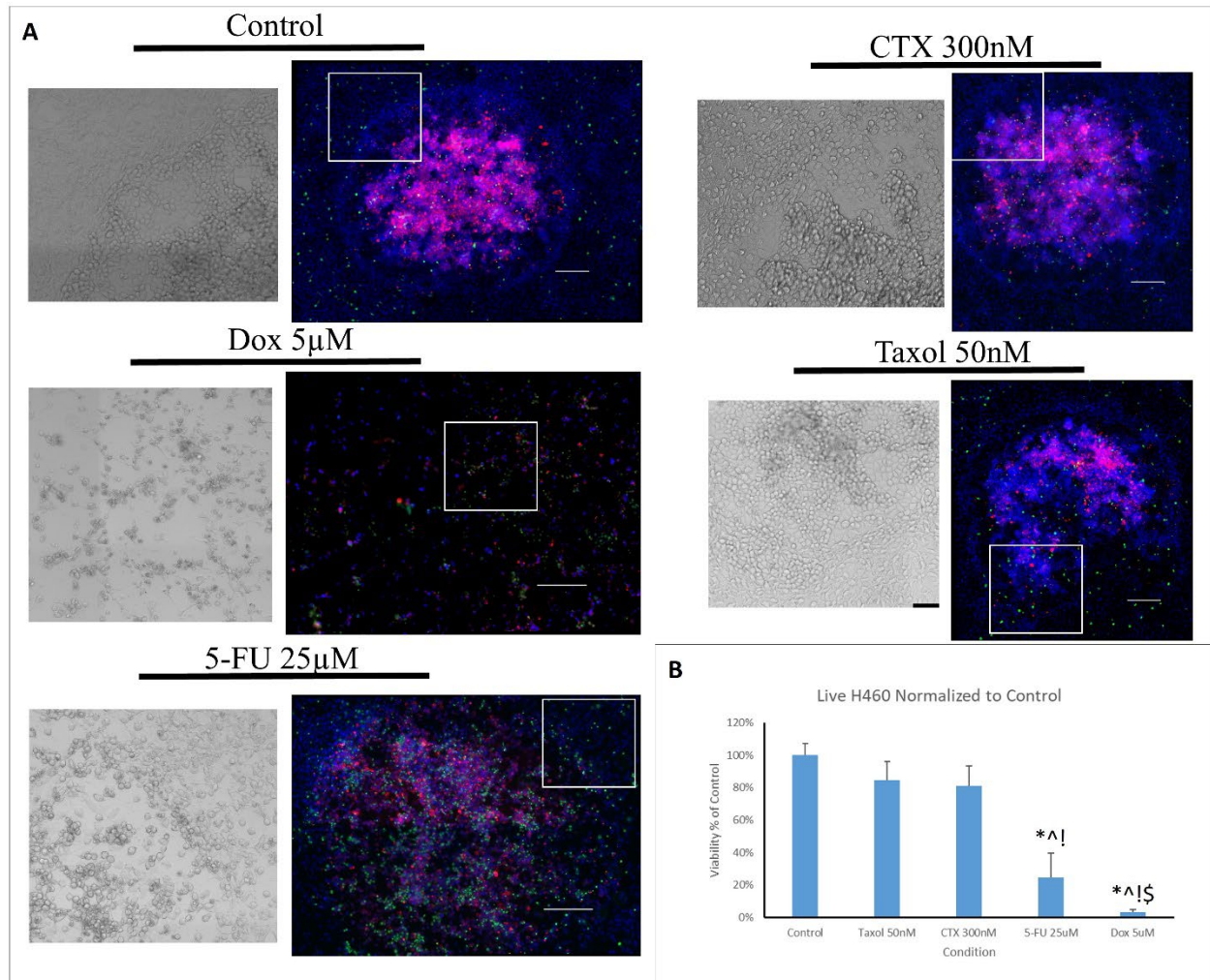


**Fig. 4. H460 and HDF- $\alpha$  viability and boundary condition affected by various drug dosages.** A. Fluorescent images include H460 cells stained with CMTMR cell tracking dye prior to seeding for fluorescent imaging and after 48 hours of incubation with drugs and no media changes, cells were stained with Hoechst and Green Live/Dead Stain for 20 minutes. Scale bar in all fluorescent images is 200 $\mu$ m. Brightfield image is a zoom in of the same image at the location indicated by the white square to observe cell viability condition and morphology. Brightfield and fluorescent images were merged and adjusted in ImageJ for clarity. B. Cell counting of live cancer cells was accomplished by utilizing ImageJ particle analyzer to count the Hoechst + CMTMR stained cells and subtracting the Green Live/Dead stained cells and then normalized to Control values to convert to percentage viability. \* indicates statistical difference from Control at  $\alpha=0.05$ . ^ indicates statistical difference from Taxol 50nM at  $\alpha=0.05$ . ! indicates statistical difference from CTX 300nM at  $\alpha=0.05$ . \$ indicates statistical difference from 5-FU 25 $\mu$ M at  $\alpha=0.05$ .

## Discussion

The cancer associated fibroblasts (CAFs) assist cancer cells in increasing their resistance and ability to metastasize from their main tumor area [10,12,29]. The current 3D co-culture devices for studying the mechanisms of the CAF action are important for guiding research informing therapeutic decisions involving more realistic CAF-cancer environments but lack simple method for testing different therapies in a quick and simple manner [19,23,26]. The present study takes advantage of a simple magnetic and 3D printable device that is adaptable to any common well-plate that facilitates rapid in vitro testing of therapeutics with a co-culture of CAF and cancer cells in a distinct island-type culture for straightforward visualization of results.

Several studies have shown increased growth in cancer cells in the presence of fibroblasts [6,8,14], including a co-culture study that delved into relationships of organ-specific fibroblasts cultured with different organ cancer cells that showed some fibroblasts are more effective than others at improving cancer cell growth [14]. The present study utilized fibroblasts and lung cancer and the co-culture lung cancer cells expanded significantly faster than monoculture lung cancer cells and formed noticeable boundary layers when contacting the fibroblasts. This accelerated co-culture tumor growth model can form these CAF-cancer relationships and allow drug studies to be completed within 72 hours of seeding time so that a large amount of information can be gathered quickly about drug-cancer-fibroblast interactions. Additionally longer length recovery studies can be run to determine if recovery of cancer and fibroblast cells occurs post-treatment.

A challenge of device is that the fibroblasts do not produce a full extra-cellular matrix (ECM) environment [30,31] and thus the full complement of metastatic cell movement and ECM degradation methods cannot be studied effectively with the current set up of the experiment. This leads the co-culture device to be stronger at determining toxicity or limiting drug studies to

targeting the mechanical movement properties of cancer cells. There are some methods of inducing ECM production from fibroblasts [32,33], but these methods will increase both the complexity of the experiment and the time required to perform each iteration and so would need to be evaluated separately for if they could improve the mimicking of in vivo conditions.

Interestingly, several studies have determined that CAFs should be a therapeutic target to help fight against the cancer growth [4,8,14]. Targeting the environment of cancer cells in conjunction with the cancer itself is a potentially effective method of dealing with cancer but may have some side effects if normal cell functions such as those demonstrated in paracrine signaling studies<sup>15,16</sup> are targeted to help suppress the cancer. Our target for therapeutics is to either allow the healthy cells to thrive or at least leave enough alive to regrow after treatments are completed and the cancer cells are eliminated. The drug study demonstrated that the Taxol dose had less toxicity for the HDF- $\alpha$  while also killing some of the H460 cells compared to the Dox and 5-FU conditions that killed all cells in the well indiscriminately. Comparing the drugs, Taxol appears to be more the attractive target to improve upon than Dox or 5-FU since the former can potentially allow regrowth of healthy cells when the treatment ends, while CTX would need synergistic drugs to take advantage of its effects on the cancer cells.

In conclusion, the results demonstrated that the co-culture device can be seeded with healthy fibroblasts and cancer cells and create an accelerated growth model with the capability of studying large amounts of therapeutics on multiple cell types simultaneously.

### **Acknowledgements**

We thank Dr. Qionghua Shen and Dr. Joseph Wolf for kindly providing training in imaging and analysis.

## Author Contributions

Y.T.K. was the principal investigator and conceived the idea. A.A.G. wrote the paper. Y.T.K. and A.A.G. developed the idea and designed the experiments. A.A.G. designed the device and provided the data. Y.T.K and A.A.G. carried out all experiments.

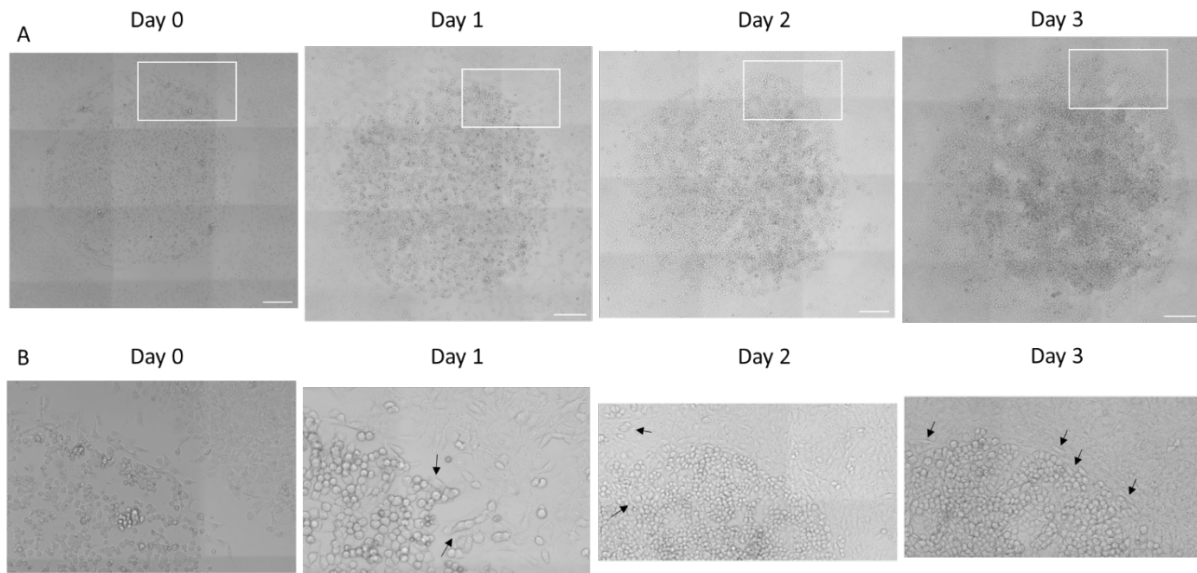
## References

1. Cancer Facts and Figures. (2022). In *American Cancer Society*. Atlanta.
2. Canadian Cancer Statistics Advisory Committee. Canadian Cancer Statistics: A 2020 special report on lung cancer. Toronto, ON: Canadian Cancer Society; 2020.
3. Sung, H., Ferlay, J., Siegel, R. L., Laversanne, M., Soerjomataram, I., Jemal, A., & Bray, F. (2021). Global Cancer Statistics 2020: GLOBOCAN Estimates of Incidence and Mortality Worldwide for 36 Cancers in 185 Countries. *CA: A Cancer Journal for Clinicians*, *71*(3), 209–249. <https://doi.org/10.3322/caac.21660>
4. Saforo, D., Omer, L., Smolenkov, A., Barve, A., Casson, L., Boyd, N., ... Beverly, L. (2019). Primary lung cancer samples cultured under microenvironment-mimetic conditions enrich for mesenchymal stem-like cells that promote metastasis. *Scientific Reports*, *9*(1), 1–16. <https://doi.org/10.1038/s41598-019-40519-4>
5. Raskov, H., Orhan, A., Gaggar, S., & Gögenur, I. (2021). Cancer-Associated Fibroblasts and Tumor-Associated Macrophages in Cancer and Cancer Immunotherapy. *Frontiers in Oncology*, *11*(May), 1–17. <https://doi.org/10.3389/fonc.2021.668731>
6. Koukourakis, M. I., Kalamida, D., Mitrakas, A. G., Liousia, M., Pouliliou, S., Sivridis, E., & Giatromanolaki, A. (2017). Metabolic cooperation between co-cultured lung cancer cells and lung fibroblasts. *Laboratory Investigation*, *97*(11), 1321–1331. <https://doi.org/10.1038/labinvest.2017.79>
7. Liu, X. Q., Kiefl, R., Roskopf, C., Tian, F., & Huber, R. M. (2016). Interactions among lung cancer cells, fibroblasts, and macrophages in 3D co-cultures and the impact on MMP-1 and VEGF expression. *PLoS ONE*, *11*(5). <https://doi.org/10.1371/journal.pone.0156268>
8. Domen, A., Quatannens, D., Zanivan, S., Deben, C., Van Audenaerde, J., Smits, E., ... Prenen, H. (2021). Cancer-associated fibroblasts as a common orchestrator of therapy resistance in lung and pancreatic cancer. *Cancers*, *13*(5), 1–22. <https://doi.org/10.3390/cancers13050987>
9. Prieto-García, E., Vanesa Díaz-García, C., Agudo-López, A., Pardo-Marqués, V., García-Consuegra, I., Asensio-Peña, S., ... Teresa Agulló-Ortuño, M. (2021). Tumor–stromal interactions in a co-culture model of human pancreatic adenocarcinoma cells and fibroblasts and their connection with tumor spread. *Biomedicines*, *9*(4). <https://doi.org/10.3390/biomedicines9040364>
10. Li, S., Ou, Y., Liu, S., Yin, J., Zhuo, W., Huang, M., ... Liu, Z. (2019). The fibroblast TIAM2 promotes lung cancer cell invasion and metastasis. *Journal of Cancer*, *10*(8), 1879–1889. <https://doi.org/10.7150/jca.30477>
11. Phan, T. K. T., Shahbazzadeh, F., Pham, T. T. H., & Kihara, T. (2018). Alpha-mangostin

- inhibits the migration and invasion of A549 lung cancer cells. *PeerJ*, 2018(6), 1–17. <https://doi.org/10.7717/peerj.5027>
12. Amann, A., Zwierzina, M., Gameraith, G., Bitsche, M., Huber, J. M., Vogel, G. F., ... Zwierzina, H. (2014). Development of an innovative 3D cell culture system to study tumour - Stroma interactions in non-small cell lung cancer cells. *PLoS ONE*, 9(3). <https://doi.org/10.1371/journal.pone.0092511>
  13. Fiorini, E., Veghini, L., & Corbo, V. (2020). Modeling Cell Communication in Cancer With Organoids: Making the Complex Simple. *Frontiers in Cell and Developmental Biology*, 8(March), 1–12. <https://doi.org/10.3389/fcell.2020.00166>
  14. Koh, B., Jeon, H., Kim, D., Kang, D., & Kim, K. R. (2019). Effect of fibroblast co-culture on the proliferation, viability and drug response of colon cancer cells. *Oncology Letters*, 17(2), 2409–2417. <https://doi.org/10.3892/ol.2018.9836>
  15. Ji, X., Ji, J., Shan, F., Zhang, Y., Chen, Y., & Lu, X. (2015). Cancer-associated fibroblasts from NSCLC promote the radioresistance in lung cancer cell lines. *International Journal of Clinical and Experimental Medicine*, 8(5), 7002–7008.
  16. Wang, L., Cao, L., Wang, H., Liu, B., Zhang, Q., Meng, Z., ... Xu, K. (2017). Cancer-associated fibroblasts enhance metastatic potential of lung cancer cells through IL-6/STAT3 signaling pathway. *Oncotarget*, 8(44), 76116–76128. <https://doi.org/10.18632/oncotarget.18814>
  17. Majety, M., Pradel, L. P., Gies, M., & Ries, C. H. (2015). Fibroblasts influence survival and therapeutic response in a 3D co-culture model. *PLoS ONE*, 10(6), 1–18. <https://doi.org/10.1371/journal.pone.0127948>
  18. Movia, D., Bazou, D., & Prina-Mello, A. (2019). ALI multilayered co-cultures mimic biochemical mechanisms of the cancer cell-fibroblast cross-talk involved in NSCLC MultiDrug Resistance. *BMC Cancer*, 19(1), 1–21. <https://doi.org/10.1186/s12885-019-6038-x>
  19. Mi, S., Du, Z., Xu, Y., Wu, Z., Qian, X., Zhang, M., & Sun, W. (2016). Microfluidic co-culture system for cancer migratory analysis and anti-metastatic drugs screening. *Scientific Reports*, 6(June), 1–11. <https://doi.org/10.1038/srep35544>
  20. Yu, T., Guo, Z., Fan, H., Song, J., Liu, Y., Gao, Z., & Wang, Q. (2016). Cancer-associated fibroblasts promote non-small cell lung cancer cell invasion by upregulation of glucose-regulated protein 78 (GRP78) expression in an integrated bionic microfluidic device. *Oncotarget*, 7(18), 25593–25603. <https://doi.org/10.18632/oncotarget.8232>
  21. Fong, E., Tzlil, S., & Tirrell, D. A. (2010). Boundary crossing in epithelial wound healing. *Proceedings of the National Academy of Sciences of the United States of America*, 107(45), 19302–19307. <https://doi.org/10.1073/pnas.1008291107>
  22. Jain, A., Bharadwaj, P., Heeg, S., Parzefall, M., Taniguchi, T., Watanabe, K., & Novotny, L. (2018). Minimizing residues and strain in 2D materials transferred from PDMS. *Nanotechnology*, 29(26). <https://doi.org/10.1088/1361-6528/aabd90>
  23. Horie, M., Saito, A., Noguchi, S., Yamaguchi, Y., Ohshima, M., Morishita, Y., ... Nagase, T. (2014). Differential knockdown of TGF- $\beta$  ligands in a interaction model of lung cancer. 1–11.
  24. Lewis, K. J. R., Hall, J. K., Kiyotake, E. A., Christensen, T., Balasubramaniam, V., & Anseth, K. S. (2018). Epithelial-mesenchymal crosstalk influences cellular behavior in a 3D alveolus-fibroblast model system. *Biomaterials*, 155, 124–134. <https://doi.org/10.1016/j.biomaterials.2017.11.008>

25. Oh, Y. S., Choi, M. H., Shin, J. I., Maza, P. A. M. A., & Kwak, J. Y. (2020). Co-culturing of endothelial and cancer cells in a nanofibrous scaffold-based two-layer system. *International Journal of Molecular Sciences*, 21(11), 1–23. <https://doi.org/10.3390/ijms21114128>
26. Bresciani, G., Hofland, L. J., Dogan, F., Giamas, G., Gagliano, T., & Zatelli, M. C. (2019). Evaluation of Spheroid 3D Culture Methods to Study a Pancreatic Neuroendocrine Neoplasm Cell Line. *Frontiers in Endocrinology*, 10(October), 1–10. <https://doi.org/10.3389/fendo.2019.00682>
27. Yaman, S., Anil-Inevi, M., Ozcivici, E., & Tekin, H. C. (2018). Magnetic force-based microfluidic techniques for cellular and tissue bioengineering. *Frontiers in Bioengineering and Biotechnology*, 6(DEC). <https://doi.org/10.3389/fbioe.2018.00192>
28. MAGNETIC 3D BIOPRINTING - HIGH-THROUGHPUT SPHEROID IMAGING AND ANALYSIS USING PERKINELMER ENSIGHTTM MULTIMODE PLATE READER. (2020). Retrieved from <http://classtap.pbworks.com/f/SkillSoft+-+Blended+Elearning.pdf>
29. Asif, P. J., Longobardi, C., Hahne, M., & Medema, J. P. (2021). The role of cancer-associated fibroblasts in cancer invasion and metastasis. In *Cancers* (Vol. 13, Issue 18). MDPI. <https://doi.org/10.3390/cancers13184720>
30. Smithmyer, M. E., Sawicki, L. A., & Kloxin, A. M. (2014). Hydrogel scaffolds as in vitro models to study fibroblast activation in wound healing and disease. *Biomaterials Science*, 2(5), 634–650. <https://doi.org/10.1039/c3bm60319a>
31. Marinkovic, M., Sridharan, R., Santarella, F., Smith, A., Garlick, J. A., & Kearney, C. J. (2021). Optimization of extracellular matrix production from human induced pluripotent stem cell-derived fibroblasts for scaffold fabrication for application in wound healing. *Journal of Biomedical Materials Research - Part A*, 109(10), 1803–1811. <https://doi.org/10.1002/jbm.a.37173>
32. Juhl, P., Bondesen, S., Hawkins, C. L., Karsdal, M. A., Bay-Jensen, A. C., Davies, M. J., & Siebuhr, A. S. (2020). Dermal fibroblasts have different extracellular matrix profiles induced by TGF- $\beta$ , PDGF and IL-6 in a model for skin fibrosis. *Scientific Reports*, 10(1). <https://doi.org/10.1038/s41598-020-74179-6>
33. van Haasterecht, L., Dsouza, C., Ma, Y., Korkmaz, H. I., de Jong, Y., Ket, J. C. F., van Zuijlen, P. P. M., Groot, M. L., & Komarova, S. v. (2023). In vitro responses of human dermal fibroblasts to mechanical strain: A systematic review and meta-analysis. *Frontiers in Mechanical Engineering*, 9. <https://doi.org/10.3389/fmech.2023.1049659>

## Supplementary Material



**Supp. Fig. 1. Progression of H460 lung cancer cells surrounded by HDF- $\alpha$  lung fibroblast cells over 3 days. (A)** Stitched images taken around entire 'tumor' cell mass in the center of the well to form a composite image in brightfield, scale bar on all images is 200 $\mu$ m. White box indicates the area of the zoomed in image in (B). (B) Close-up images of the advancing boundary of H460 lung cancer with arrows indicating cells with elongated morphology compared to the general 'tumor' mass cells.

***Chapter 3: Machine Learning enabled classification of lung cancer cell lines co-cultured with fibroblasts with lightweight convolutional neural network for initial diagnosis***

Adam Germain<sup>1</sup>, Alex Sabol<sup>2</sup>, Anjani Chavali<sup>1</sup>, Giles Fitzwilliams<sup>1</sup>, Alexa Cooper<sup>3</sup>, Sandra Khuon<sup>4</sup>, Bailey Green<sup>1</sup>, and Young-Tae Kim, PhD<sup>1,5\*</sup>

<sup>1</sup>*Department of Bioengineering, University of Texas at Arlington, TX*

<sup>2</sup>*Department of Computer Science, University of Texas at Arlington, TX*

<sup>3</sup>*Department of Biology, University of Texas at Arlington, TX*

<sup>4</sup>*Department of Nursing, University of Texas at Arlington, TX*

<sup>5</sup>*Department of Urology, University of Texas Southwestern Medical Center, Dallas, TX*

Correspondence and Requests for materials should be addressed to:

\*Corresponding author:  
Young-Tae Kim, Ph.D.  
Department of Bioengineering  
500 UTA Blvd ERB244  
University of Texas at Arlington  
Arlington, TX 76010

E-mail : ykim@uta.edu  
Fax: 817-272-2251  
Phone: 817-272-5023

Keywords: lung cancer, machine learning, co-culture, classification, diagnosis

## **Abstract**

Identification of lung cancer subtypes is critical to treatment success in patients, especially those with more advanced lung cancer stages. Many advanced and personal treatments require knowledge of specific mutations and gene up- and down- regulations for exploitation to lead to the elimination of the cancer cells. While many studies focus further on individual cell structures and going deeper into gene sequencing, the present study proposes a machine learning method of cancer classification based on low-magnification cancer outgrowth patterns in a 2D co-culture environment. The lightweight convolutional neural network model based on the TinyVGG architecture was able to achieve 100% classification accuracy on the testing dataset between A549 squamous cell carcinoma and H460 large cell carcinoma lung cancer cell types at 2-, 3-, and 9-days of outgrowth over surrounding fibroblasts. These results demonstrate that both adapting the data to take advantage of the neural network and looking at larger patterns can be valuable for classification of lung cancer subtype during diagnoses.

## Introduction

Lung cancer classification is an important step in getting the correct treatment for the patient, especially as treatments become more customized to individual patient needs. Without the correct identification of a tumor, the molecular targeted therapies and immunotherapies have much less chance of impacting the cancer growth at all [1,2,3]. While small cell lung carcinoma (SCLC) and non-small cell lung carcinoma (NSCLC) tend to be easier to separate due to the oat-like appearance of the SCLC, there are subtypes of both cancers that are not as simple to differentiate. NSCLC can be divided into adenocarcinoma (ADC), squamous cell carcinoma (SCC), large cell neuroendocrine carcinoma (LCNEC) with the remaining falling under a broader category large cell carcinoma (LCC) and SCLC containing small cell or combined small cell carcinoma types [2,4,5]. The current state of diagnosis involves looking at morphology, then immunohistochemistry, followed by genetic testing [1]. While genetic testing is important, it helps to have narrowed the scope of the genetic testing by finding a correct subtype of the cancer before continuing onto the more specific mutations that may have occurred within the tumor cells. Machine learning enabled neural networks can provide a unique opportunity for reliably catching trends in images that humans cannot easily find.

Convolutional Neural Networks (CNNs) have been utilized widely for image classification with AlexNet [6], VGGnet [7], ResNet [8], and DenseNet [9] performing very well at classifying images of different types for competitions. The reason for CNN's success in image classification comes from the ability of the convolutional blocks to learn different types of features within images through conversion of the pixels to numerical values of intensity and then applying mathematical filters that create specific patterns when applied to corners, edges, and other features that may be important. Within the CNN type of neural network numerous have been used to help with

classification of lung cancer with various data inputs. At the immunohistochemistry level, there are several papers describing CNN's that can analyze histopathological sample slides of lung cancers and classify them into appropriate subtypes at the same or higher rates of success than trained histopathologists [5,10,11,12,13]. The main benefit of these methods appears to be in providing confirmation or a second pass at classification for improved confidence in diagnosis. There are other researchers taking a genetic approach to neural network use, with gene profiles being fed into algorithms to predict subtypes of lung cancers [2,14,15]. These methods can get more specific with the subtype of cancer, for example, including the different categories of adenocarcinoma such as lepidic (LEP), papillary (PAP), acinar (ACN), micropapillary (MIP), or solid (SOL), among others, and are useful for applying targeted therapies if the appropriate gene expressions can be identified [1,15,16]. These types of CNN's all look at data at a single point of time since the cancer cells must be fixed for histopathology and lysed to gather gene expression information.

The current study investigated a method of classifying lung cancer subtypes with a lightweight CNN model called TinyVGG, starting with differentiating between H460 large cell carcinoma and A549 squamous cell carcinoma. We utilized a well plate holder that can create an island of cancer cells to generate training data of the macro-growth of both cancer types each in the presence of human dermal fibroblast- $\alpha$  (HDF- $\alpha$ ) which improves the growth rate of the cancer cells [17]. The differentiation of the cell lines by outgrowth pattern over surrounding fibroblasts allows for larger patterns to be seen and, with cancer growth being significantly higher than healthy fibroblast growth, mixed samples from patients can likely be classified easily over a short period of 1-10 days.

## **Materials and Methods**

## *2.1 Cell Lines, Culture, and Reagents*

The human dermal fibroblast  $\alpha$  (HDF- $\alpha$ ), human NSCLC line NCI-H460 (large cell carcinoma), and human NSCLC line A549 CCL-185 (squamous cell carcinoma) were purchased from ATCC and cultured in RPMI medium supplemented with 10% of fetal bovine serum with all cell lines grown in 37 °C and 5% CO<sub>2</sub>. Anycubic Photon Mono and Anycubic 3D Printer 405nm SLA UV-Curing Resin purchased from Amazon. The convolutional neural network was trained on an nVidia GeForce GTX 1050 with 4GB of video RAM, Intel i5 9300 2.4 GHz, and 8 GB of system RAM.

## *2.2 Lung Cancer Cell Lines and HDF- $\alpha$ Co-culture for Cancer Outgrowth Collection*

To briefly summarize the device from a previous study [17], a 12-well magnet holder was created from 3D printed UV-resin. Magnets were then inserted, the device was sterilized, and a 12-well plate was placed on top of the holder while inside a biosafety cabinet. The sterilized stainless-steel tubes were placed on top of the magnets, inside all wells. The wells were seeded with 5,000 H460 or A549 cancer cells in 3 $\mu$ L on the inside of the tube and 20,000 HDF- $\alpha$  fibroblasts in 40 $\mu$ L outside of the tube. The cells were incubated for 3 hours at 37°C and 5% CO<sub>2</sub> to allow for cell attachment to the well plate. The tubes were then carefully removed in the biosafety cabinet via tweezers and then brightfield pictures were taken to verify correct seeding had occurred and to note the initial state of the well (Fig. 1c). Then 1.5mL of fresh RPMI + 10% FBS growth media was added to each well and they were incubated for 9 days, with images taken each day around the same time for each well. Images were all taken in a 2x2 grid at a 2.5x magnification, centered on the seeding island formed from the tube. These images were then stitched together using the stitching program developed by Preibisch et. Al [18] followed by centering each set of time series of images for consistency and then cropping them so that the total area is uniform utilizing Adobe Photoshop. The H460 wells had an n = 86 and the A549 had an n = 42, which is low for a neural network. To

help expand our available data, we decided to perform some data augmentation in the form of rotation and mirroring of our data. All the images were reduced to 512x512 pixel image size, then flipped horizontally and vertically. Each of these transforms and the original image were then rotated 90, 180, and 270 degrees to create a dataset that is 12 times larger than the original images. The purpose of gathering as large of a dataset as possible via data augmentation is to expand the generalization of the model such that it has a greater ability to predict and forecast when given new information. These augmentations were chosen because the growth of the cells is radial and ‘random’. It is possible that if the same cells were seeded at rotated configuration, then they would have also grown at the same rotated configuration, all of which can be seen in Figure 1 below.

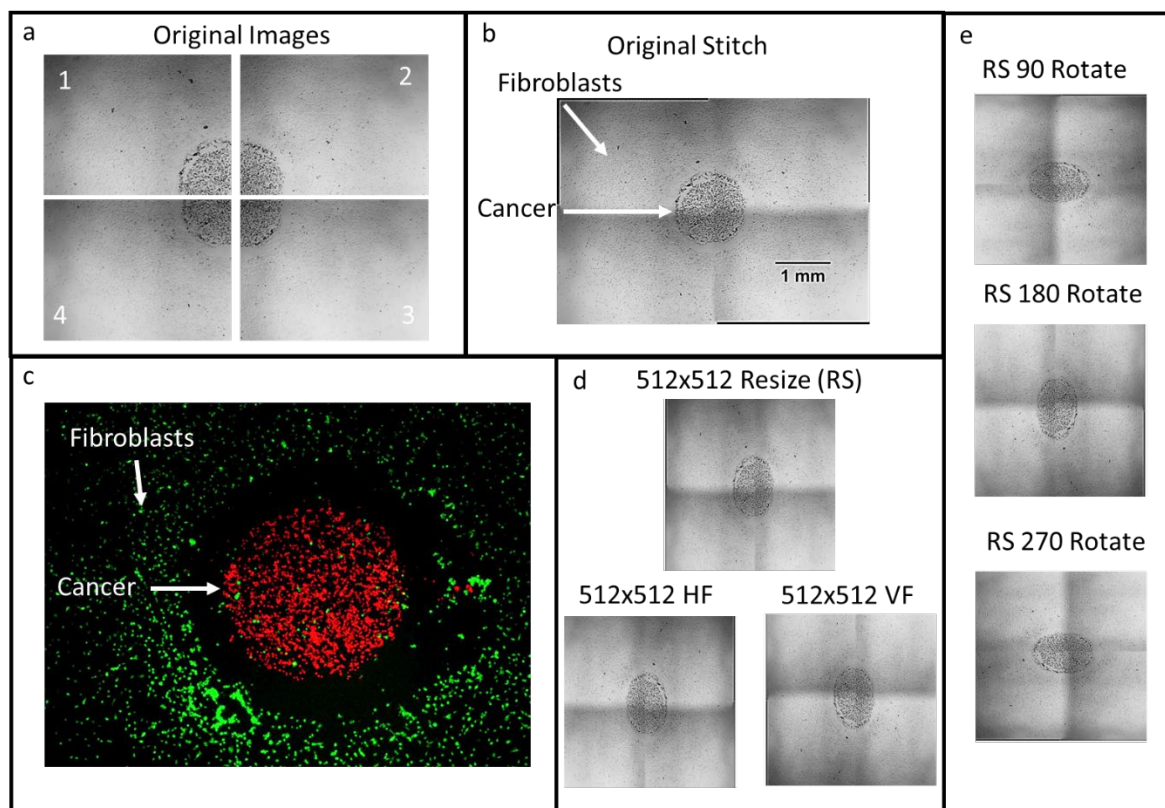


**Figure 1. Lung cancer growth collection, image modification, and augmentation for machine training.** (a) Original images taken in order of the numbers indicated in the corner (2x2 at 2.5x magnification). (b) Combined image after stitching program. Scale bar = 1 mm (c) Fluorescent image showing the cells differentially stained prior to seeding, red color denotes the cancer cell line H460, and the green color denotes the healthy HDF- $\alpha$  fibroblasts. (d) Original image resized

to 512x512 pixels (RS) and then both horizontally (HF) and vertically flipped (VF) for data augmentation. (e) Example of rotations of original image at 90°, 180°, and 270° for data augmentation.

### 2.3 TinyVGG Convolutional Neural Network Parameters for Cancer Classification

The most basic structure of a CNN model is the following, with the previous output feeding the next layer’s input: a convolutional layer, an activation function, a pooling layer, a flattening layer, a dense layer, and then the loss function. We used the TinyVGG model, the architecture shown below in Figure 2, because it was designed to perform image classification tasks while requiring less computational resources and having fewer parameters to adjust so that training would be relatively simple.

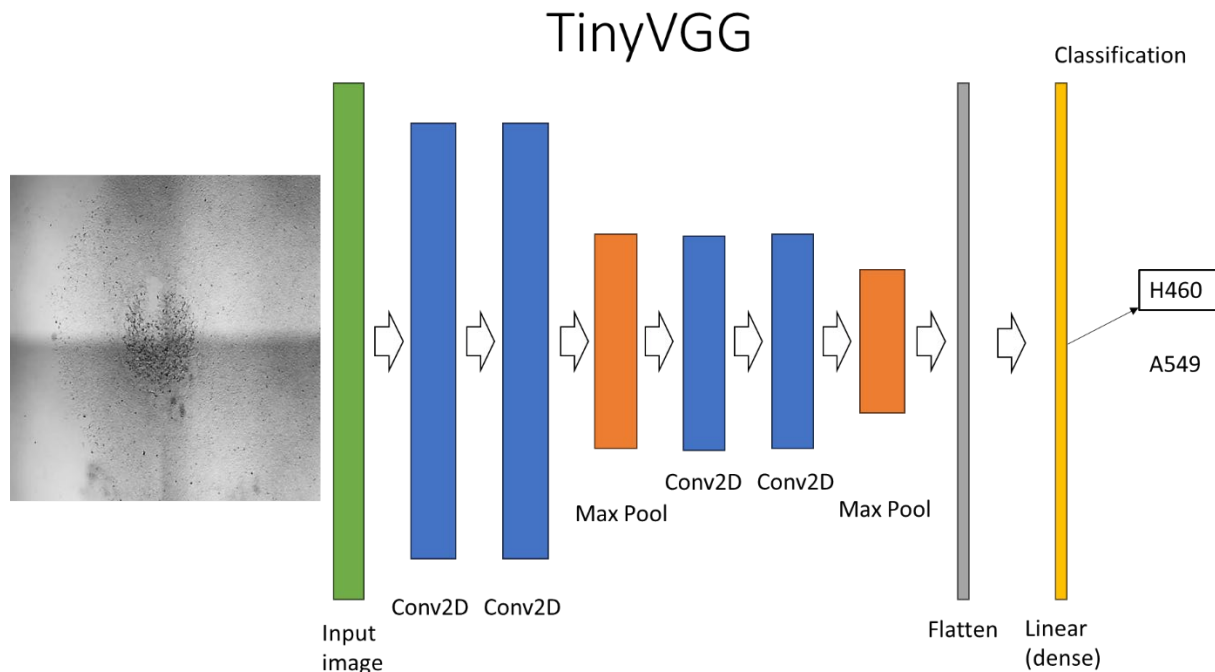


**Figure 2. Schematic of the architecture of the main blocks of the TinyVGG model [19] for lung cancer classification via machine learning.** At the start, the model is initialized with random weights. Training images (i.e., lung cancer outgrowth over surrounding fibroblasts, left) are passed through in batches for a designated number of epochs and given classifications. Batch size is the

number of images passing through the model before the random weights are updated. One epoch is a full cycle of the training images running through the TinyVGG model. At the end of each epoch, the validation set runs through the model to determine the accuracy of the model on data that the model has not seen for training. The model optimizes the weights by reducing the loss of the training data. Conv2D = 2D Convolution.

*Convolution:* The convolutional layers have customizable parameters of output-channels, kernel size, stride length, and padding to create a number of filters equal to the input channels multiplied by the output channels, of a size based on the kernel size, stride length, and padding. The kernels perform a mathematical operation on the pixels, utilizing a matrix the size of the kernel dimensions. The kernel performs the operation on the set of pixels and translates across the image a number of pixels based on the stride value. Padding adds a layer of blank pixels around the edge of the image with the purpose of both retaining image size and increasing edge effects, as without padding the edges of an image will be reduced due to fewer kernel operations applying to them. For example, the 512x512x1 pixel image input with an output-channels of 3, kernel size of 3x3 pixels, stride of 1 pixel, and padding of 1 pixel, generates an output of 512x512x3. If we change the kernel size to 4x4 pixels and stride to 2 pixels, the output feature map becomes 256x256 pixels, halving the width and height dimensions for the output tensor. The feature maps are learned based on the loss function of the model later, with more feature maps meaning more trainable parameters. For our version of the model, we have the parameters of kernel size, stride length, padding, and filters for the convolutional 2D layers shown in Table 1.

Parameters	Layer 1	Layer 2	Layer 3	Layer 4
<b>Kernel Size</b>	4x4	3x3	3x3	3x3
<b>Stride Length</b>	2	1	1	1
<b>Padding</b>	1	1	1	1
<b>Filters</b>	10	100	100	100
<b>Input Size (HxWxC)</b>	512x512x1	256x256x10	128x128x10	128x128x10
<b>Output Size (HxWxC)</b>	256x256x10	256x256x10	128x128x10	128x128x10

**Table 1. List of utilized convolutional layer parameters for lung cancer classification.** Kernel size chosen to give the largest feature maps. Layer 1 (first Conv2D in Fig. 2) kernel size, stride, and padding were chosen to reduce image size by half for the output size (i.e., 512x512x1 to 256x256x1) for model complexity reduction, while the other layers (Layers 2-4) maintain image size between input and output. Further reductions in size between Layer 2 and Layer 3 are due to the Max Pooling functions. Output channels maintain at 10 to increase filters after the initial convolution (i.e., 10 to 100 filters) to pick up on higher order features. H x W x C = Height x Width X Channel(s).

*Activation:* The activation function takes the feature map(s) of the convolutional layer and applies an element-wise operation to them and will always follow a convolutional layer. Oftentimes the activation function is assumed and is not included in the visual representation of a convolutional neural network model. The most common activation functions are ReLU (rectified linear unit), sigmoid, hyperbolic tangent functions. The ReLU function takes all values that are negative and makes them zeroes, while directly transferring the positive values ( $y=x$ ), and is the function utilized in our model.

*Pooling:* Pooling layers are utilized after convolutional blocks (multiple convolutional layers and activation functions) to reduce both the computational load of the training and overfitting that can occur. The inputs to a pooling layer are the kernel size and stride. Our model uses a 2x2 pixel kernel with a stride of 2, which reduces the output feature map to one-half of the size for both width and height, ending with 25% of the starting data. Additionally, there are two common pooling layers used called average pooling and max pooling. The average pooling takes the average of the values in the 2x2 kernel as the output for a single value while the max pooling takes the highest value of the kernel as the output. Average pooling can help preserve feature localization, while max pooling ensures that the most prominent features are conserved and is the pooling layer utilized in our model.

*Flatten and Dense Layers:* The flatten layer simply transforms the 3D matrix of data into a 1D vector of data such that the dense layer can utilize the features found and find the patterns for cancer classification. The dense layer creates the parameters to be adjusted for the resulting output classification (H460 classification in Fig. 2). In this case we utilize the Linear function in Pytorch which creates a model of  $y = xA^T + b$ , where  $x$  is the input value,  $y$  is the output value, and  $A$ ,  $T$  and  $b$  are learnable weights, for each input value in the flattened tensor. Essentially, each pixel value has a customizable linear function associated with it that the model can tune during training. These sum together to form the overall output classification of the model given an input.

*Loss Function and Accuracy:* The loss function is the tool with which the model gauges the effectiveness of the weights in the previous dense layer. We used the Cross Entropy function which compares the predicted class of an input image, based on the output of the dense layer, with the ground truth value, also known as the label, of the class of the image. The magnitude of the difference between the truth classification value and the output of the algorithm is the “Loss”. The algorithm goes through training sessions where the input data is fed into the model and the weights are periodically changed with the goal of minimizing the loss function. Accuracy is another common metric in classification which tells you how often the algorithm correctly classifies images and is not related to how far off the guesses are but is useful for diagnosing problems with the training or interpreting if a high or low loss value is acceptable.

Typically, there is a split of the dataset to use for training and validation, commonly with 80% of the data being set aside for training and the balance for validation. The training dataset is used to inform the weights of the algorithm and the validation dataset is utilized as the optimization metric. The purpose of this is to try to reduce overfitting of the data as the validation dataset should be

“unknown” to the algorithm, as far as the weighting is concerned, and should provide initial feedback as to the potential efficacy of the model.

## **Results**

For this convolutional neural network (CNN), we wanted to determine how well the model could be trained to classify between different lung cancer subtypes. Initially, we ran tests on H460 growth sequences, while continuing to collect data, to see if the model had the capability to classify growth of the same cancer. There is inherently some variability as though cancer cells consistently grow fast, they do still vary in growth rate. Once these tests were run, we decided to test how many days of growth were necessary before the model could classify between A549 and H460. The same days of growth for each cancer subtype were paired so that a standard number of days of incubation could be used in the future in a clinical setting for the model.

### *3.1 Classification of different days of growth within each cell line*

The first test was to see how well the model could differentiate between the different days of growth of the same type of cancer. If the model had too much trouble classifying days of growth, differences would need to be quite large between cell types for their classification. As can be seen in Figure 3a, the largest visual difference between days occurs days 3-4-5, after the cancer has fully occupied the center starting area and has had time to grow in multiple layers in the starting location, which causes a significant darkening of the center pixels. An outer ring of slightly darkening pixels also forms, giving the model two significant features to the human eye, at least, to learn.

The model was trained with a batch size of 128, learning rate of 0.001, and weight decay of 0.003 for 25 epochs. The convolutional neural network training results can be seen in Figure 3b. In Fig.

3b on the left, the model was trained to differentiate among all days of growth, 0-9 (i.e. 10 total classes), for either A549 (Fig. 3b left-top) or H460 (Fig. 3b left-bottom) and was able to reach around 50% accuracy. This means given any single day of an entire sequence of growth, the models have a 50% chance to correctly predict that day. The A549 time sequences had a loss of around 1, meaning that the model was able to score around  $\pm 1$  day or that it was not able to easily distinguish between consecutive days of growth. The H460 cells had a continually increasing loss in the validation dataset (Fig. 3b left-bottom; green line), showing that the tuning parameters were being adjusted such that the correct guesses were being fit more accurately, but the incorrect guesses were becoming farther from the real day. Every other day classifications were very similar for each of the cancer cell types. A549 cells days of growth could be predicted for even and odd days at 87.7% (Fig. 3b, middle-top; training and validation accuracy) and 95.4% (Fig. 3b. right-top), respectively, showing that if the difference (between days) is great enough, the certainty of the algorithm will increase drastically. H460 cells days of growth could be predicted for even and odd days at 85.0% % (Fig. 3b, middle-bottom; training and validation accuracy) and 86.1% (Fig. 3b. right-bottom), respectively. The model performed lightly worse when classifying H460 days of growth, but still performed similarly to the A549 classifications of every other day.

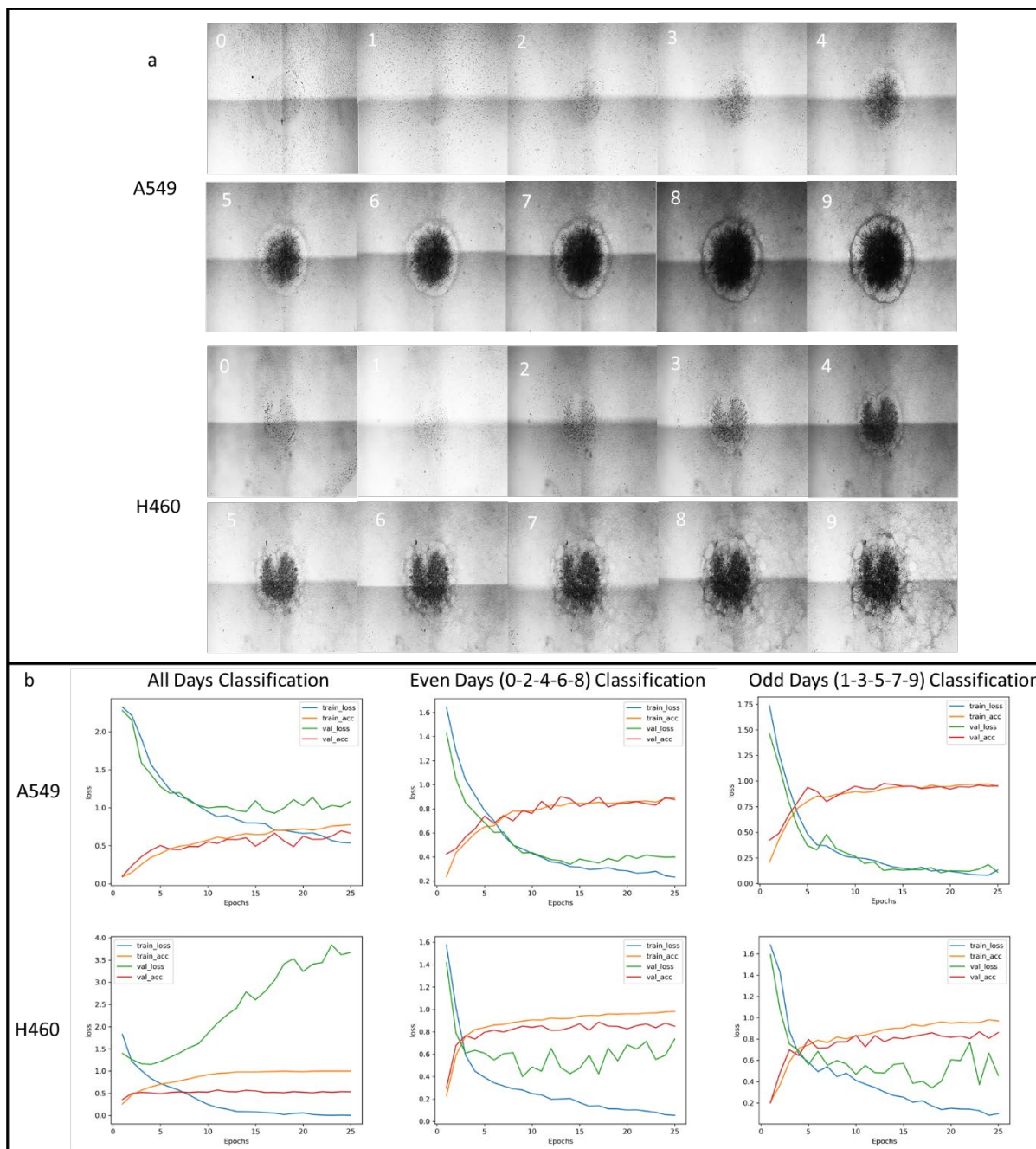


**Figure 3. A549 and H460 Time Series Differentiation.** (a) Example sequences of data for both A549 and H460 cancer cells over 9 days of growth with day labels located in the corner of each image. 0: 3 hours after seeing both lung cancer cells at the center and surrounding fibroblasts. 1-9: 1-9 days after seeding. (b) A549 and H460 time sequences of day 0 to day 9 of growth trained on the TinyVGG model for 25 epochs, or full cycles of training data (x-axis). The graphs show the training loss (blue), training accuracy (orange), validation loss (green), and validation accuracy (red) achieved for classification of all days (left), and then the two every other day methods of even days (middle) and odd days (right). Loss is the difference between the predicted classification and the true classification (from the label; y-axis). Accuracy is simply the count of correct

classifications divided by total classifications. The model modifies parameters based on the training data and reports the metrics at the end of every epoch. As an example, H460 all days classification (left-bottom) shows an increasing validation loss while all other metrics (training accuracy, training loss, and validation accuracy) stay the same. This means that the model is making small adjustments to attempt to improve the training loss, but they are resulting in the incorrect classifications of the validation data being farther from correct while not meaningfully impacting the correct classifications.

### *3.2 A549 and H460 Classification at the same day of growth*

From Figure 3a, we can see that there appear to be different patterns in growth between A549 and H460 that, to the human eye, become more prevalent as the cells progress from Day 0 to Day 9 of outgrowth. A549 squamous cell carcinoma appears to have a thicker contact border that remains intact for the duration of the outgrowth over the fibroblasts. H460 large cell carcinoma, on the other hand, forms small individual pockets at its border and more satellite colonies that presumably migrated out from the main mass of cells created in the initial seeding. Days 0-2 (Fig. 3a) appear nearly equal in growth rate with a similar pattern of density increase from Day 0 to Day 1 followed by a thin border formation in addition to a center mass density increase from Day 1 to Day 2. Day 2 to Day 5 (Fig. 3a) shows a slightly faster boundary formation and faster darkening of the center cancer mass in the H460 cells compared to the A549 cells. After this point, Day 5 to Day 9 (Fig. 3a) shows the H460 cells losing their distinct round boundary by smaller circular growths and then the formation of numerous satellite growth locations while the A549 cells continue to thicken the boarder and limited satellite growth is observed. From these observations, we hypothesized that the CNN model would have a gradually increasing classification accuracy by day of cancer outgrowth, likely starting near 50% (which is the equivalent of a random guess with only 2 classes, H460 or A549), as our human eyes can notice more differences by the day, with Day 0-2 being indistinguishable. Instead, while Day 0 was slightly better than a random guess at 61.9% accuracy,

Day 1 increased dramatically to 90.9% accuracy, Day 2 and Day 3 both had a 100% accuracy, Day 4-6 decreased to around 95% accuracy, Day 7 and Day 8 following the negative trend at 91.3% and 90.9%, respectively, and then a jump back to 100% accuracy at Day 9 (Figure 4b). The CNN model was able to quickly learn features that allowed it to classify between the two cell lines, H460 and A549, meaning that it may be possible to create model that requires only 2 days of cell incubation after harvesting to return a lung cancer subtype classification. Days 4, 5, 7, and 8 all showed a much higher ending validation loss (Fig. 4a; green line) compared to training loss (Fig. 4a; blue line) Of note, the model could accurately predict the cell >90% of the time given at least 24 hours of outgrowth, and then also had 100% classification accuracy at Day 9 of outgrowth. If adding other lung cancer subtypes begins to reduce the accuracy at the early days of outgrowth, then the model still may be able to classify very accurately at later days of outgrowth, giving the CNN model a decent range to work with that is still able to give a lung cancer classification answer within 1.5 weeks. Interestingly, the CNN model is clearly capable of learning features that are not readily discernible to the naked eye (Fig. 3a; cancer outgrowth comparison between A549 and H460 at Day 1, 2), which means we may be missing some details on the patterns of cancer outgrowth.

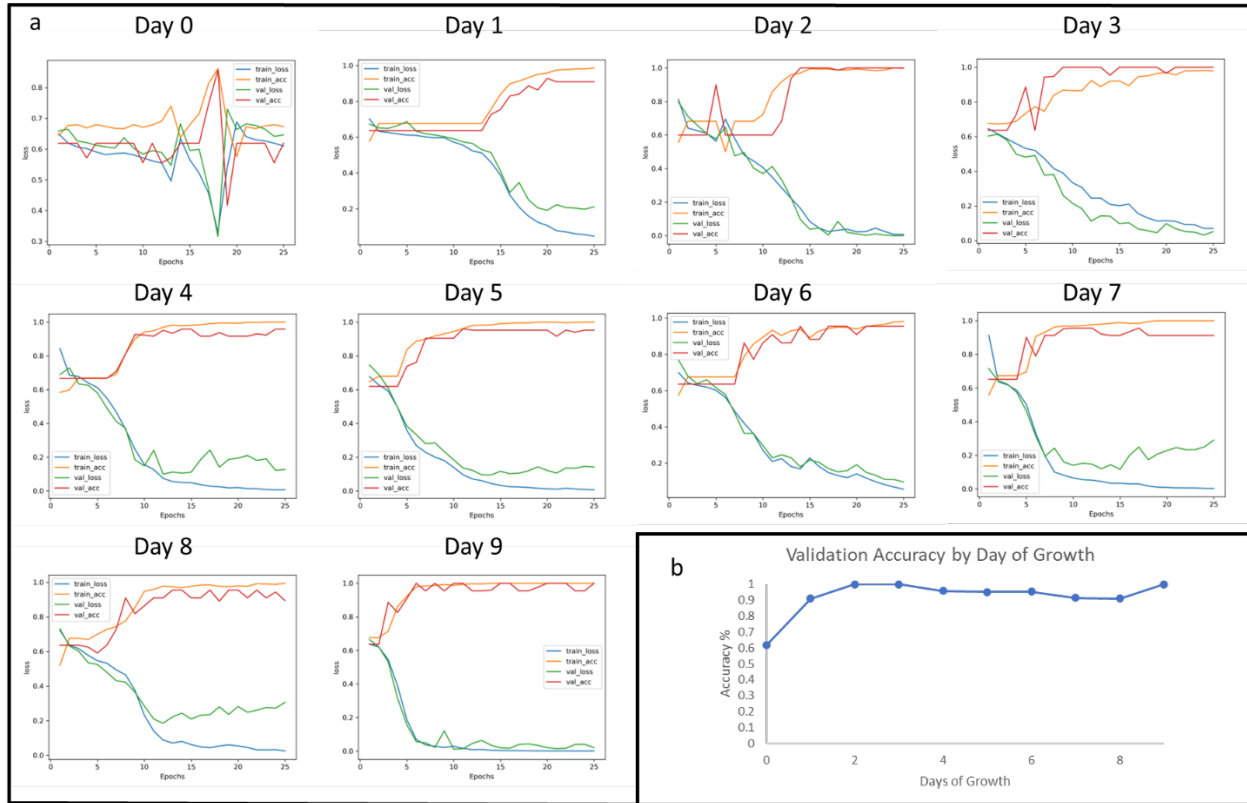


**Figure 4. A549 and H460 classification by day of growth to determine how many days of growth are necessary for reliable classification between A549 and H460.** Two classes trained for 25 epochs on the TinyVGG model, one for A549 and one for H460 of the given day. All parameters maintained the same across all 10 sets of training. (a) The same days (Day 1-9) of growth for each cancer subtype are paired (e.g., Day 1: H460 cancer outgrowth at one day after seeding is paired with A549 cancer outgrowth at one day after seeding). The graphs show the training loss (blue), training accuracy (orange), validation loss (green), and validation accuracy (red). (b) The classification accuracy of the validation dataset at the different days (e.g., Day 0 validation accuracy is 61.9% after 25 epochs of training) with the Day on the x-axis and the Classification accuracy in the y-axis.

## Discussion

CNNs are helpful with increasing the ability of researchers and clinicians to detect patterns and features of images that are difficult to see or notice upon visual inspection [3,5,10,11,12]. While there many complex and deep neural networks [6,7,8,9], changing the input dataset to take advantage of machine learning occurs can help reduce the need for extreme computing power and allow more researchers access to the technology without needing to spend time and resources on

acquiring high power GPUs for neural network training. The present study utilized 512x512 greyscale images designed to classify the cancer cells by their positions of overgrowth and thus darkening of pixels and was able to run the lightweight TinyVGG model on a computer with 4 GB of video RAM and achieved very high rates of classification accuracy between two subtypes of lung cancer (Fig. 4).

There are still some challenges that need to be overcome with machine learning, such as the quality of the input data and the size of the training dataset. There are many articles and reviews that discuss the need for preparing the input dataset for optimal machine learning, including labeling the dataset, cropping and resizing the images, and cleaning the images and then also emphasizing the need for robust data that includes as many varied versions of the input data as possible, including augmentation to change orientation of data to ensure that the model can learn weights that will apply to the broadest number of cases [20,21,22,23]. The present study could use some testing on lighting normalization, artifact removal (bubbles/debris/scratches in images) to ensure that the CNN is learning to differentiate based on the cancer outgrowth over surrounding fibroblasts rather than an unrelated feature being present. Additionally, an increase in the represented subtypes of lung cancer cells, including multiple variants of each subtype, would ensure that the classification could be generalized to all lung cancer subtypes and that the categories were more robust.

In conclusion, the results demonstrated that even simple CNN architecture can create a model that is capable of classifying lung cancer cell lines based upon their outgrowth patterns in the presence of surrounding fibroblasts.

### **Acknowledgements**

We would like to acknowledge the University of Texas at Arlington for facility support.

## Author Contributions

Y.T.K. was the principal investigator. A.A.G. wrote the paper. Y.T.K. and A.A.G. developed the idea and designed the experiments. A.A.G. coded and trained the neural network and provided the data. Y.T.K., A.A.G., A.C., G.F., A.C., S.K., and B.G. carried out all experiments.

## References

1. Nicholson, A. G., Tsao, M. S., Beasley, M. B., Borczuk, A. C., Brambilla, E., Cooper, W. A., Dacic, S., Jain, D., Kerr, K. M., Lantuejoul, S., Noguchi, M., Papotti, M., Rekhtman, N., Scagliotti, G., van Schil, P., Sholl, L., Yatabe, Y., Yoshida, A., & Travis, W. D. (2022). The 2021 WHO Classification of Lung Tumors: Impact of Advances Since 2015. In *Journal of Thoracic Oncology* (Vol. 17, Issue 3, pp. 362–387). Elsevier Inc. <https://doi.org/10.1016/j.jtho.2021.11.003>
2. Fauteux, F., Surendra, A., McComb, S., Pan, Y., & Hill, J. J. (2021). Identification of transcriptional subtypes in lung adenocarcinoma and squamous cell carcinoma through integrative analysis of microarray and RNA sequencing data. *Scientific Reports*, *11*(1). <https://doi.org/10.1038/s41598-021-88209-4>
3. Jain, D., Nambirajan, A., Chen, G., Geisinger, K., Hiroshima, K., Layfield, L., Minami, Y., Moreira, A. L., Motoi, N., Papotti, M., Rekhtman, N., Russell, P. A., Prince, S. S., Schmitt, F., Yatabe, Y., Eppenberger-Castori, S., Bubendorf, L., Beasley, M. B., Berezowska, S., ... Wistuba, I. (2022). NSCLC Subtyping in Conventional Cytology: Results of the International Association for the Study of Lung Cancer Cytology Working Group Survey to Determine Specific Cytomorphologic Criteria for Adenocarcinoma and Squamous Cell Carcinoma. *Journal of Thoracic Oncology*, *17*(6), 793–805. <https://doi.org/10.1016/j.jtho.2022.02.013>
4. *What Is Lung Cancer? About Lung Cancer*. (n.d.). American Cancer Society. Last Revised: January 12, 2023
5. Yang, J. W., Song, D. H., An, H. J., & Seo, S. B. (2022). Classification of subtypes including LCNEC in lung cancer biopsy slides using convolutional neural network from scratch. *Scientific Reports*, *12*(1). <https://doi.org/10.1038/s41598-022-05709-7>
6. Krizhevsky, A., Sutskever, I., & Hinton, G. E. (2012). ImageNet Classification with Deep Convolutional Neural Networks. *Advances in Neural Information Processing Systems*, *25*. [https://proceedings.neurips.cc/paper\\_files/paper/2012/file/c399862d3b9d6b76c8436e924a68c45b-Paper.pdf](https://proceedings.neurips.cc/paper_files/paper/2012/file/c399862d3b9d6b76c8436e924a68c45b-Paper.pdf)
7. Simonyan, K., & Zisserman, A. (2014). *Very Deep Convolutional Networks for Large-Scale Image Recognition*. <http://arxiv.org/abs/1409.1556>
8. He, K., Zhang, X., Ren, S., & Sun, J. (2015). *Deep Residual Learning for Image Recognition*. <http://arxiv.org/abs/1512.03385>
9. Huang, G., Liu, Z., van der Maaten, L., & Weinberger, K. Q. (2016). *Densely Connected Convolutional Networks*. <http://arxiv.org/abs/1608.06993>
10. Li, M., Ma, X., Chen, C., Yuan, Y., Zhang, S., Yan, Z., Chen, C., Chen, F., Bai, Y., Zhou, P., Lv, X., & Ma, M. (2021). Research on the Auxiliary Classification and Diagnosis of

- Lung Cancer Subtypes Based on Histopathological Images. *IEEE Access*, 9, 53687–53707. <https://doi.org/10.1109/ACCESS.2021.3071057>
11. Kosaraju, S., Park, J., Lee, H., Yang, J. W., & Kang, M. (2022). Deep learning-based framework for slide-based histopathological image analysis. *Scientific Reports*, 12(1). <https://doi.org/10.1038/s41598-022-23166-0>
  12. Al-Jabbar, M., Alshahrani, M., Senan, E. M., & Ahmed, I. A. (2023). Histopathological Analysis for Detecting Lung and Colon Cancer Malignancies Using Hybrid Systems with Fused Features. *Bioengineering*, 10(3). <https://doi.org/10.3390/bioengineering10030383>
  13. Hamed, E. A. R., Salem, M. A. M., Badr, N. L., & Tolba, M. F. (2023). An Efficient Combination of Convolutional Neural Network and LightGBM Algorithm for Lung Cancer Histopathology Classification. *Diagnostics*, 13(15). <https://doi.org/10.3390/diagnostics13152469>
  14. Niemira, M., Collin, F., Szalkowska, A., Bielska, A., Chwialkowska, K., Reszec, J., Niklinski, J., Kwasniewski, M., & Kretowski, A. (2020). Molecular signature of subtypes of non-small-cell lung cancer by large-scale transcriptional profiling: Identification of key modules and genes by weighted gene co-expression network analysis (WGCNA). *Cancers*, 12(1). <https://doi.org/10.3390/cancers12010037>
  15. Hu, F., Zhou, Y., Wang, Q., Yang, Z., Shi, Y., & Chi, Q. (2020). Gene Expression Classification of Lung Adenocarcinoma into Molecular Subtypes. *IEEE/ACM Transactions on Computational Biology and Bioinformatics*, 17(4), 1187–1197. <https://doi.org/10.1109/TCBB.2019.2905553>
  16. Tsao, M. S., Marguet, S., le Teuff, G., Lantuejoul, S., Shepherd, F. A., Seymour, L., Kratzke, R., Graziano, S. L., Popper, H. H., Rosell, R., Douillard, J. Y., Le-Chevalier, T., Pignon, J. P., Soria, J. C., & Brambilla, E. M. (2015). Subtype classification of lung adenocarcinoma predicts benefit from adjuvant chemotherapy in patients undergoing complete resection. *Journal of Clinical Oncology*, 33(30), 3439–3446. <https://doi.org/10.1200/JCO.2014.58.8335>
  17. Germain, A., Young-Tae, K. Co-culture device for in vitro high throughput analysis of cancer associated fibroblast and cancer cell interactions. *Oncology*. DOI: 10.1159/000533773
  18. Preibisch, S., Saalfeld, S., & Tomancak, P. (2009). Globally optimal stitching of tiled 3D microscopic image acquisitions. *Bioinformatics*, 25(11), 1463–1465. <https://doi.org/10.1093/bioinformatics/btp184>
  19. Wang, Z. J., Turko, R., Shaikh, O., Park, H., Das, N., Hohman, F., Kahng, M., & Chau, D. H. (2020). *CNN Explainer: Learning Convolutional Neural Networks with Interactive Visualization*. <https://doi.org/10.1109/TVCG.2020.3030418>
  20. Alzubaidi, L., Zhang, J., Humaidi, A. J., Al-Dujaili, A., Duan, Y., Al-Shamma, O., Santamaria, J., Fadhel, M. A., Al-Amidie, M., & Farhan, L. (2021). Review of deep learning: concepts, CNN architectures, challenges, applications, future directions. *Journal of Big Data*, 8(1). <https://doi.org/10.1186/s40537-021-00444-8>
  21. Belcher, B. T., Bower, E. H., Burford, B., Celis, M. R., Fahimipour, A. K., Guevara, I. L., Katija, K., Khokhar, Z., Manjunath, A., Nelson, S., Olivetti, S., Orenstein, E., Saleh, M. H., Vaca, B., Valladares, S., Hein, S. A., & Hein, A. M. (2023). Demystifying image-based machine learning: a practical guide to automated analysis of field imagery using modern machine learning tools. In *Frontiers in Marine Science* (Vol. 10). Frontiers Media S.A. <https://doi.org/10.3389/fmars.2023.1157370>

22. Adam, R., Dell'Aquila, K., Hodges, L., Maldjian, T., & Duong, T. Q. (2023). Deep learning applications to breast cancer detection by magnetic resonance imaging: a literature review. In *Breast Cancer Research* (Vol. 25, Issue 1). BioMed Central Ltd. <https://doi.org/10.1186/s13058-023-01687-4>
23. Shah, A. A., Malik, H. A. M., Muhammad, A. H., Alourani, A., & Butt, Z. A. (2023). Deep learning ensemble 2D CNN approach towards the detection of lung cancer. *Scientific Reports*, 13(1). <https://doi.org/10.1038/s41598-023-29656-z>

***Chapter 4: Forecasting accelerated lung cancer outgrowth using a convLSTM  
neural network with a co-cultured device for data collection***

Adam Germain<sup>1\*</sup>, Alex Sabol<sup>2\*</sup>, and Young-Tae Kim, PhD<sup>1,3\*\*</sup>

<sup>1</sup>*Department of Bioengineering, University of Texas at Arlington, TX*

<sup>2</sup>*Department of Computer Science, University of Texas at Arlington, TX*

<sup>3</sup>*Department of Urology, University of Texas Southwestern Medical Center, Dallas, TX*

*\*Co-first authors with equal contributions*

Correspondence and Requests for materials should be addressed to:

**\*\*Corresponding author:**  
Young-Tae Kim, Ph.D.  
Department of Bioengineering  
500 UTA Blvd ERB244  
University of Texas at Arlington  
Arlington, TX 76010

E-mail : [ykim@uta.edu](mailto:ykim@uta.edu)  
Fax: 817-272-2251  
Phone: 817-272-5023

Keywords: forecasting, lung cancer, machine learning, co-culture, LSTM, prognosis

## **Abstract**

Accelerated lung cancer outgrowth forecasting can transform the ability for clinicians to evaluate patient treatments. Many lung cancers are found in later stages of growth and require quick evaluation and treatment to help combat tumor masses and the existing or potential metastases. Having a scalable in vitro model to forecast how a treatment may impact a patient's lung cancer will influence both the number of potential treatments and the amount that will likely succeed. This study proposes an accelerated convLSTM machine learning model that is capable of forecasting cancer outgrowth over fibroblasts through a recursive method that uses a high throughput 2D co-culture data collection method and only requires 9 days of cancer outgrowth. The convLSTM model was trained for 1600 epochs achieved an SSIM score of 0.813 and LPIPS score of 0.046 when comparing ground truth data to model generated data. The model was also able to forecast cancer outgrowth following the extrapolated growth curve for 5 days for the control on the 1600 epoch model and 10 days for the Taxol 50nM condition when the model was further trained using the Taxol 50nM treatment dataset. These results demonstrate that with greater computing resources and data collection the recursive convLSTM model could produce forecasts much farther than 10 days into the future.

## **Introduction**

Lung cancer continues to have a high incidence rate and high mortality rate due to its clinical discovery tending to occur in both older individuals and at later stages of growth with about a 1 in 16 chance of a person developing lung cancer in their lifetime [1]. A key method of increasing patient survivability has been the focus on genetic testing for personalized medicine, as particular mutations can be selectively targeted with either immunotherapies or protein specific inhibiting agents [2]. The method of obtaining genetic information of the tumor continues to be the various biopsy methods, including but not limited to open lung biopsy, video-assisted thoracic surgery, and transbronchial biopsy which utilize direct surgery, endoscopy, and flexible bronchoscopy [3]. Both new biopsy techniques and new gene sequencing methods share the same goal of reducing the size of biopsy samples to reduce patient impacts from the specimen removal, and so the biopsy sample itself is a very precious resource that must be conserved for known diagnostic methods [2,4,5].

One important aspect of the chosen technology for machine learning enabled models is the prevalence of data. CT scans and are being taken advantage of by researchers and their machine learning algorithms, in part because they are very simple to acquire and large amounts of data can be produced relatively easily compared to most other imaging regimes, which makes them simultaneously more difficult for the human eye and more suitable for machine analysis [6,7]. In this track of machine learning for CT scans, they are being used for recurrence risk prediction [8], survival prediction and prognosis confirmation [9], and even for performing competitions for lung cancer detection through the screening CT scans [10]. There are many others, but these examples show that the methods of imaging that can be exploited for deep learning are gaining a lot of attention.

Additionally, models that can predict the outcome of drug studies on a personalized basis, especially if they do not require additional biopsy sampling and can enhance the current histopathological and genetic testing, are becoming much more valuable. Machine learning has become a popular avenue for drug effectiveness predictions, as there are many ways to utilize data from the biopsy samples to compare trends learned either in vitro in labs or by running models with public health information [11]. Recent studies have explored the ability to predict drug effectiveness by using drug binding site information and patient data [12], to predict new potential drugs specifically for lung adenocarcinoma based on graph attention networks which genes can be targeted [13], and to predict immunotherapy targeting effectiveness of NSCLC and its recurrence through methylation markers [14] among other strategies. The immense amount of data collected from clinical and lab settings has caused some researchers to hypothesize the implementation of a ‘digital biopsy’ to aid in clinical decisions in the future [15]. As of now, lung cancer drug future information is limited to simple predictions of responses from time series CT-images from time series information or forecasting 1D data such as incidence and mortality rates [16,17], though there is recognition that forecasting cancer growth like forecasting weather could occur in the near future and with emphasis on convolutional long short-term memory (convLSTM) models for the image and time series properties [18,19].

With increasing data and data sources comes the requirement of preparing this data for machine learning. Since the machine learning algorithms are learning their own features with which to give weight, researchers need be sure that they are not allowing unrelated pieces of data to influence machine decisions. Data preparation refers to the resizing, modifying, the annotating or labeling of the data, and other necessary changes or augmentations required to ensure the data is suitable for input to a machine learning model. This topic is important enough that there are guides and

tools available for people entering the medical research space [20,21] and data preparation should always be a consideration when utilizing image data as there can be artifacts such as bubbles or metadata tags, lighting inconsistencies, blurriness, digitization, etc. that an algorithm can determine is an important feature in decision making.

In the present study, we propose a (convLSTM) algorithm that can begin to forecast lung cancer outgrowth over fibroblasts on a well plate, both with and without the influence of chemotherapeutics. Fibroblasts are utilized for their effects of both increasing growth rate and drug resistance of cancer cells such that the model is accelerated and more realistic with regards to drug efficacy. Using a 3D printed magnet holder and tubes for seeding segregation, we created an island of cancer growth within fibroblasts that enabled time series images of nine days to be taken in large quantities for model training to forecast the baseline outgrowth of lung cancer over fibroblasts in addition to the forecasting of lung cancer outgrowth treated with low doses of Paclitaxel to predict whether the drug at the dose may have a positive outcome. We also performed a comparative analysis on model performance with raw data and various levels of data preparation to emphasize its importance.

## **Materials and Methods**

### *Cell Lines and Culture and Reagents*

The human dermal fibroblast  $\alpha$  (HDF- $\alpha$ ) and human NSCLC line NCI-H460 were purchased from ATCC and cultured in RPMI medium supplemented with 10% of fetal bovine serum with all cell lines grown in 37 °C and 5% CO<sub>2</sub>. The therapeutic Paclitaxel (Taxol, PHL89806) was purchased from Sigma-Aldrich. Anycubic Photon Mono and Anycubic 3D Printer 405nm SLA UV-Curing Resin purchased from Amazon. Neural network was trained on an T4 High RAM computer via Google Colabatory with 15GB of GPU RAM and 52 GB of system RAM.

### *Lung Cancer Cell Lines and HDF- $\alpha$ Co-culture for Data Collection*

To briefly describe the well plate holder from a previous paper [22], a 12-well magnet holder was created in SolidWorks and 3D printed with UV cured resin. Magnets were inserted, the entire device was sterilized, and a 12-well plate was placed on top while inside a biosafety cabinet. The stainless-steel tubes were sterilized and placed inside all wells, held in the center of each by the magnets. The wells were seeded with 5,000 H460 cancer cells in 3 $\mu$ L on the inside of the tube and 20,000 HDF- $\alpha$  healthy fibroblast cells in 40 $\mu$ L outside of the tube. The cells were incubated for 3 hours at 37°C and 5% CO<sub>2</sub> to allow for cell attachment to the well plate. The tubes were carefully removed in the biosafety cabinet via tweezers followed by brightfield images being taken to verify correct seeding had occurred and for Day 0 of data collection. Then 1.5mL of fresh RPMI medium + 10% FBS growth media was added to each well and they were incubated for 9 days, with images taken each day around the same time for each well. Images were all taken in a 2x2 grid at a 2.5x magnification, centered on the seeding island formed from the tube. For the drug conditions, the only addition to the procedure is that media was changed after 24 hours of incubation, containing either 10nM or 50nM of Taxol. The duration of the drug studies was also 9 days.

### *Data Preparation*

These images were then stitched together using the stitching program developed by Preibisch et. Al [23] followed by centering each set of time series of images for consistency and then cropping them so that the total area is uniform utilizing Adobe Photoshop. The H460 wells had a sequence number of  $n = 86$ , the Taxol 10nM condition had an  $n = 20$ , and Taxol 50nM condition had an  $n=21$ . The original data contained numerous potential issues with regards to inconsistent lighting, shadows, bubbles, and other artifacts that could confuse the convLSTM learning and have it place more importance in useless information. Normalizing the lighting required the division of the

images by the gaussian blur of the image, which averages every pixel value with the surrounding pixel values. It was noticed that the image artifacts were mostly white/black bars from stitching or cropping, or black debris/black bubbles with white centers, and the cell parts of the images tended to contain values at neither the white (255) nor the black (0) end of the pixel value range. As such, the image artifact removal is a more complicated function, but the basic idea is that a mask is applied to the images which replaces the pixels that are much darker or much brighter than the rest of the image and those pixels are replaced by their reflection across x axis, their reflection across the y axis, pixels from the previous image in the sequence, or pixels from the next image in the sequence, based on which result ends up with lowest standard deviation. The artifact removal was only applied to the control H460 images. As a last change, the reduction in size down to 64x64 was creating occasional images that were significantly different from the original, particularly with the earlier days of growth where the cancer cells and fibroblasts have a more uniform appearance. The default bilinear interpolation method was utilized on both the original images and the lighting normalized images before being changed to the inter area interpolation method to preserve as much original image quality as possible for the fixed images and later steps. On top of the data preparation, we needed more data to help train our neural network, so we decided to perform some data augmentation in the form of rotating and mirroring our data. Large data sets allow for the best ability for a model to form a more generalized algorithm so that it can more accurately deal with unseen circumstances rather than being too specific towards the training data. All the images were reduced to both 64x64 and 512x512 pixel image size, after original images were fixed, then flipped horizontally and vertically. Each of these transforms and the original resized image were then rotated 90, 180, and 270 degrees to create a dataset that is 12 times larger than the original dataset, giving us around one thousand sequences of 9-days of H460 cell outgrowth. These augmentations

were chosen because the growth of the cells is radial and ‘random’. It is possible that if the same cells were seeded at rotated configuration, then they would have also grown out at that same rotated configuration compared to the original image. Examples of all steps can be seen in Figure 1.

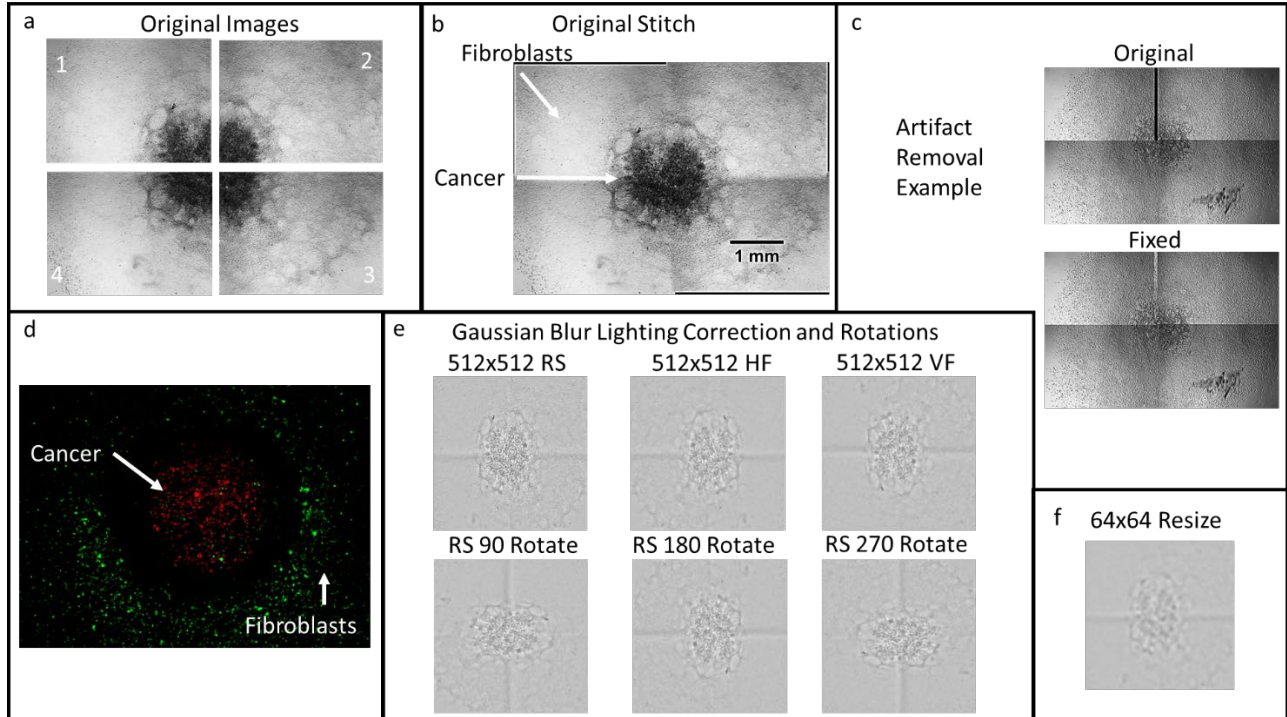


**Figure 1. Data collection, image preparation, downsizing, and augmentation.** (a) Microscope images taken in order of the numbers indicated in the corners (2x2 at 2.5x magnification). (b) Combination of images after stitching program. Scale bar = 1 mm. (c) Artifact removal program demonstrating black bar removal from lack of overlap during original image capture, original image on top and fixed image below. (d) Fluorescent image demonstrating the island seeding method 3 hours after seeding with the cell lines differentially stained red (H460 lung cancer) and green (HDF- $\alpha$  fibroblasts) prior to the seeding. (e) Division of fixed images by gaussian blur averaging to remove lighting gradients, followed by the resizing (RS) from 2592x1728 pixels to 512x512 pixels, then both horizontally flipping (HF), vertically flipping (VF), and image rotation of versions by 90°, 180°, and 270°. (f) Lighting normalized and fixed images resized to 64x64 pixel size. All the same augmentations have been applied to 64x64 images.

### *convLSTM Architecture and Parameters*

A convLSTM neural network is best understood by first explaining the convolutional blocks and the LSTM blocks separately, then the overall function of the model can be explained more effectively.

A 2D convolutional block utilizes a matrix, called a kernel, which creates filters from the input image. The neural network learns the different values of the kernel matrix through feedback from the loss function later in the model. The main parameters for the block are the output channels, which will be equal to our filters since the number of filters is equal to input channels multiplied by output channels, kernel size, stride length, and padding. Stride length is the distance the kernel travels between operations and the padding is the number of blank pixels added around the image, used to both maintain the original image size and to increase edge pixels effects.

The LSTM neural network is a recurrent neural network that holds a memory state throughout a time series, can forget and update the cell state at each time step, and can be ‘taught’ with external data inputs being given to their respective time steps. Each LSTM block consists of a number of LSTM cells that is based upon the number of time steps of the input data. The premise behind this type of recurrent neural network is that the cell state can avoid both accumulating too much information and forgetting too much information, which cause exploding and vanishing gradients respectively, due to the gating systems at the different steps. The inputs to an LSTM cell are the memory from previous cell, the output of the previous cell, and the input for the current cell. The outputs of a cell are the memory and information output which in this case is in the form of an image. The memory is what is known as the “hidden state” because it is only contained internally within the LSTM and will influence the output of the cell but is not directly shown. The important pieces of the LSTM cell are the cell state, forget gate, input gate, and output.

The cell state is the current hidden state of the model, held continuously through the consecutive LSTM cells for the entire LSTM network. If nothing is changed, the cell state at time  $t=t$  will be the same as the cell state at time  $t=0$ . The hidden state is adapted by the learning in the forget and input gates and the applies this learning of the hidden state to the output.

The forget gate determines how much of the old memory from the previous state needs to be forgotten, ranging from forgetting the entirety of the prior memory to forgetting nothing based upon the combination of the hidden state, the previous output and the input. Weights here are learned over time by minimizing the loss function.

The input gate then performs the function of determining how much of the new memory is allowed to influence the hidden state by utilizing a merge of the three inputs to determine how much of the new input combined with the previous output will influence the hidden state. Weights here are learned over time by minimizing the loss function.

The output of the cell is the output image from the model at that time point and is also fed into the next LSTM cell in the sequence. The output is a quantity of the hidden state which is determined by combining the cell state after the forgetting and updating steps with the input and previous cell output.

The loss function is the tool that the model uses to gauge the ability of the model to accurately output images. The convLSTM model uses a combined loss function of equal weights mean squared error (MSE) and mean absolute error (MAE) to compare the generated images to the ground truth images. MSE measures the average of the squares of the difference between the generated pixel values and the ground truth pixel values. MAE measures the absolute average distance between the generated pixel values and the ground truth pixel values. The combined

function is utilized so that MSE penalizes larger pixel differences while MAE can help give more weight to smaller pixel differences.

The convLSTM is simply the combination of convolutional 2D blocks with the LSTM cells, and a schematic of the architecture used can be seen in Figure 2. The input images are passed through conv2D blocks to extract and learn features and then these are passed as inputs to the LSTM, where the hidden state of the LSTM learns which features to add and forget over time. At first, the convLSTM learns through a process called “teacher forcing”, which allows the convLSTM to see the ground truth images as inputs. Over time, there is a decay function on the teacher forcing that gradually reduces the amount of ground truth images being seen, and slowly moves the learning over to a recursive process where the only inputs to the convLSTM become the output of the previous cell and the hidden state. This is important because the convLSTM needs to be capable of recursive function to output forecasted images as they inherently have no ground truth basis to input.

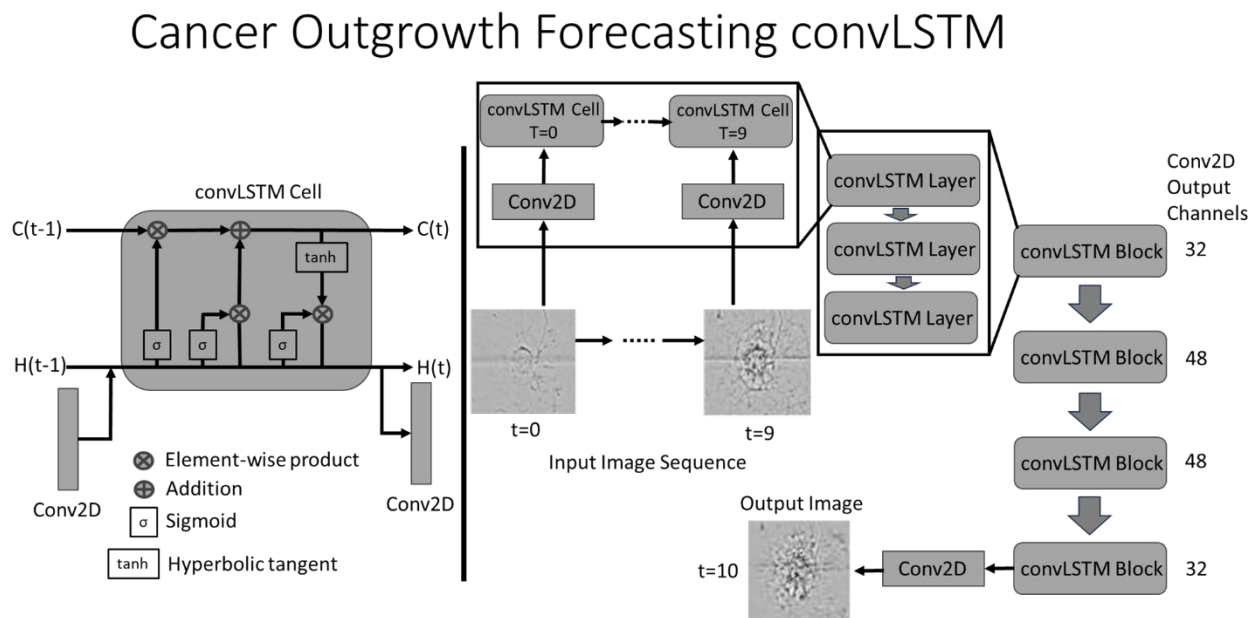


**Figure 2. Schematic of the architecture of the convLSTM model for lung cancer forecasting, based on convLSTM by Su, J and Byeon, W et al [24].** The convLSTM cell takes Conv2D inputs to influence the cell state,  $C(t)$ , by means of the forget gate, the input gate, and the output gate, which passes on an output state,  $H(t)$ , that can be converted into an image. The number of convLSTM cells in each layer is equal to the number of images in the input time sequence, in this case 10 images from Day 0 to Day 9 of cancer growth. Each convLSTM layer then outputs a sequence of outputs to feed into the next convLSTM layer. All convLSTM cells in a given block have the same number of Conv2D output channels, denoted on the right side of the image. Each block passes outputs to the next block in the same serial manner. The final convLSTM block outputs to a Conv2D block that converts the output back to a single channel grey scale image, in this case at  $t=10$  for the time sequence, forecasting the 10th day of cancer growth. The convolutional blocks before each input allow the model to learn features, such as edges, lines, and corners, and their relationships in a time dependent manner with later convLSTM block learning higher order features such as circles, squares, and other shapes. The model is recursive, meaning that the outputs can continue past the original time series length by utilizing the output image,  $H(t-1)$ , as the input image to the next convLSTM cell and then output the  $t=11$  image in the sequence.

We use a split of the original dataset to use for training and validation, with 80% of the time sequences being set aside for training and the balance for validation. To avoid any potential learning oddities from the rotations, a well sequence and all its augmentations were either in training or in validation. The training dataset is used to inform the weights of the algorithm and the validation dataset is utilized as the optimization metric. The purpose of this is to try to reduce overfitting of the data as the validation dataset should be “unknown” to the algorithm, as far as the weighting is concerned, and should provide initial feedback as to the potential efficacy of the model. Model parameters can be seen in Table 1.

convLSTM Model Parameters				
<b>Input Channels</b>	1	<b>Batch Size</b>		36
<b>Learning Rate</b>	0.001	<b>Weight Decay</b>		0.0003
<b>Optimizer</b>	FusedAdam	<b>Teacher Forcing Decay</b>		0.04
<b>Kernel</b>	3x3	<b>Input Frames</b>		5
<b>convLSTM Blocks</b>	Block 1	Block 2	Block 3	Block 4
<b>LSTM Layers per block</b>	3	3	3	3
<b>Output Channels conv2D</b>	32	48	48	32

**Table 1. List of convLSTM model parameters that were used during all training runs.** Batch size is the number of sequences run through the model before parameters are updated. In this case, batch size was limited due to GPU RAM resources available. The learning rate, or the maximum

weight change per batch, was set to 0.001 with a weight decay of 0.0003. Teacher forcing decay reduces the input images by 0.04 per epoch to eventually have the model learn in an unsupervised manner over time. Input frames of 5 means that, out of the 10 available frames, only 5 are given at a time for the sequence learning. The convLSTM layers, output channels, and blocks are related. The output channel filters from the convolution occur at the beginning of each of the LSTM cells in each LSTM layer of the first block. This means that there are 3, time sequence sets of features at 32/1024/1024 sizes in the first block that the LSTM layers are learning from. The next block contains 3, time sequence sets of features of 1536/2304/2304 sizes for the LSTM layers to learn from.

## **Results**

### *Data Preparation and Effect on Forecasting Loss and Image Quality*

The effect of data preparation is important to investigate when running a new dataset on a model to determine how much effort needs to be applied to future data before training. In this case we compared three different data preparation levels and then also added in a comparison of a non-residual model which is directly comparable to the fixed image model as we had residuals as the default set up and they were trained on the same dataset. The reference images are the 64x64 pixel images used for each dataset which are then compared to images generated by the model. The loss function compares the training dataset with the generated images while the structural similarity index (SSIM) and learned perceptual image patch similarity (LPIPS) compared the Day 9 ground truth validation images to model generated images. Examples of the compared images can be seen in Figure 3. The shadows in the original image dataset clearly influence the model generated images as they contain the same or more shadows than the ground truth image. The lighting normalized set shows increased fuzziness in both the ground truth and model generated images. The generated images of both models appear to match most closely, though the model lacking the residual function produces more blurry versions of the ground truth images compared to the model containing the residual function. At this resolution, it is difficult to pick up the difference in image quality between the 800 epochs of training and 1600 epochs of training for the control vs fixed

model. The Taxol 10nM and Taxol 50nM have some slight imperfections in the form of some faded areas and some extra dark pixels, but the extra training on the Taxol 50nM images produces more complete copies of the ground truth images.

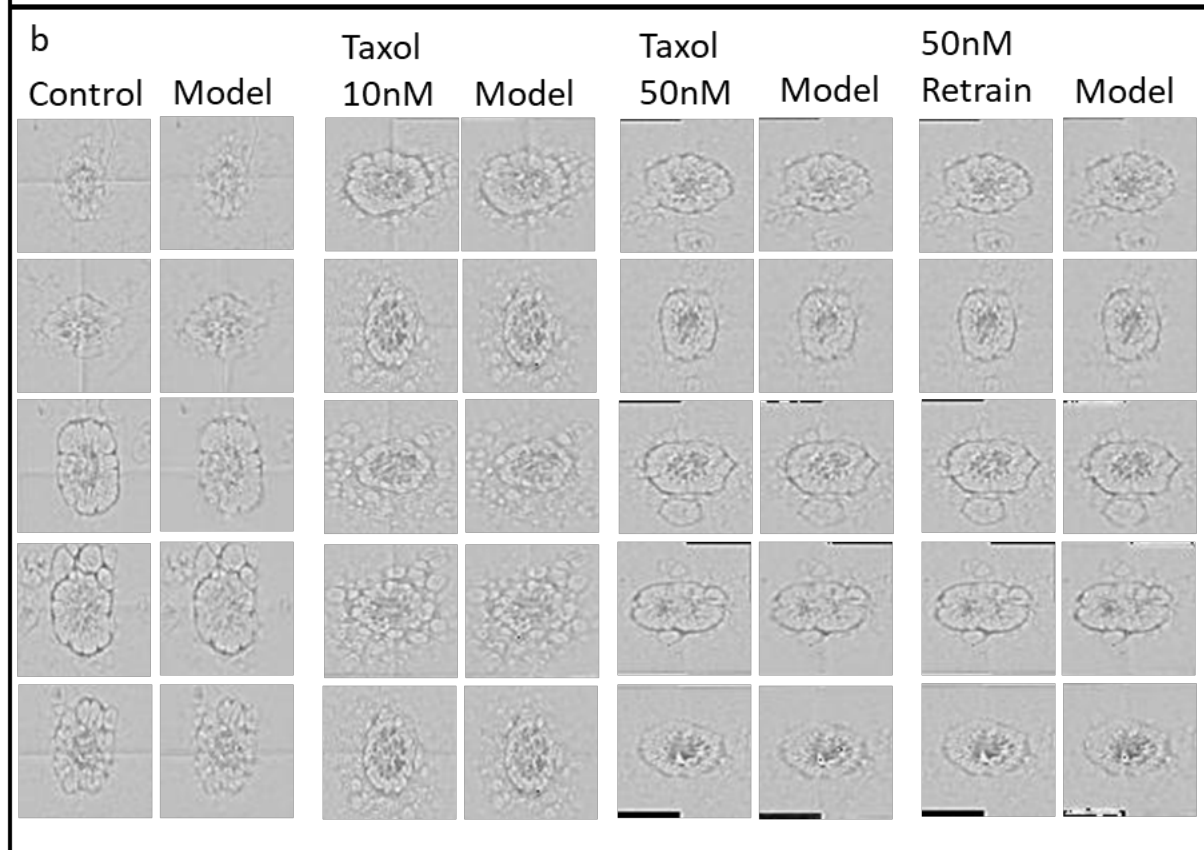
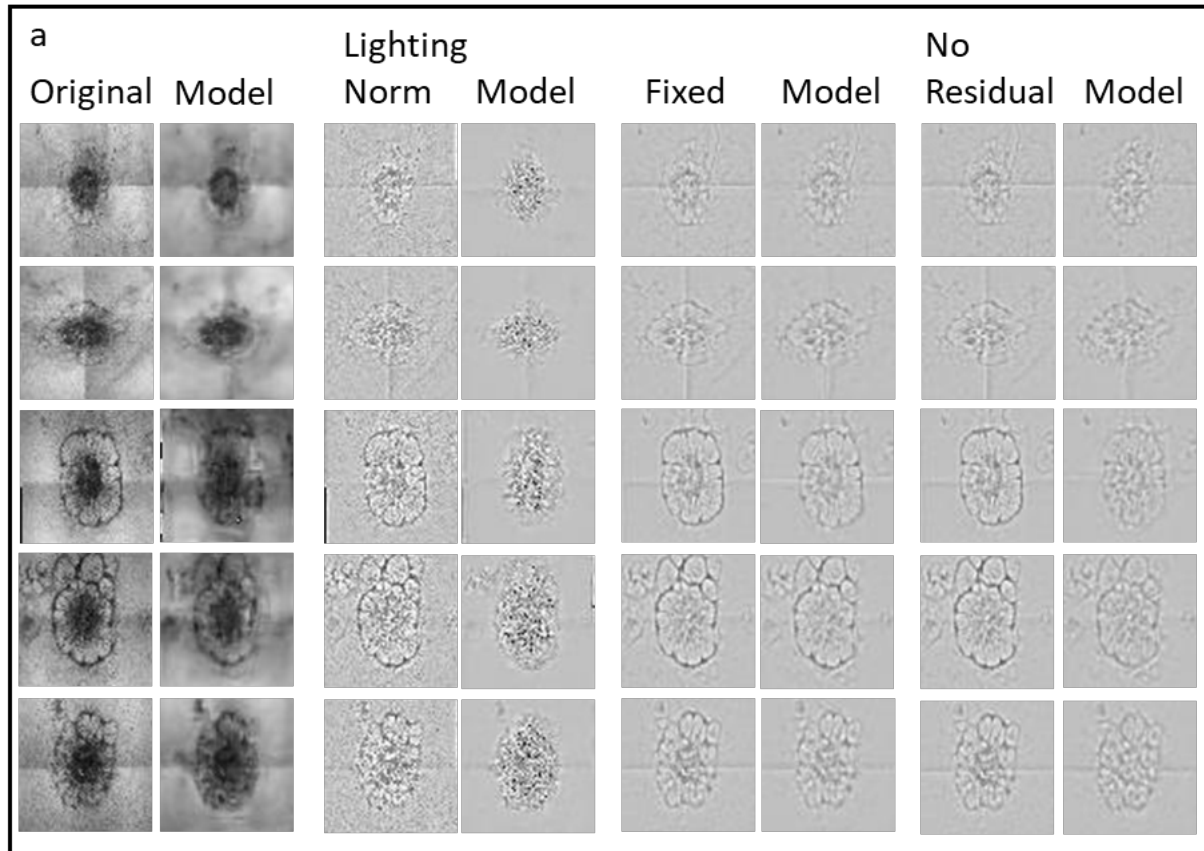


**Figure 3. Ground truth image and model generated image comparison.** (a) From left to right: Original images resized, lighting normalized images by gaussian blur function, fixed images, model images generated without residual function. The models were trained on the ground truth images on the left side of each pair of columns and the models produced the right column images. To make comparison easier, the same batch of wells all at Day 9 of cancer outgrowth were used. (b) The best performing model was chosen for extra training and then comparison of performance on Control vs Taxol 10nM treatment vs Taxol 50nM treatment. Afterwards, the model was trained an additional amount on the Taxol 50nM images.

From Table 2, we can see that the loss values for the fixed images is 2.7 times and 3 times lower than the original images and the lighting normalized images, respectively, when trained the same number of epochs. The two models performed significantly lower in SSIM and LPIPS scores as a result. The model lacking the residual function was trained more epochs because the residual function tends to allow neural networks to train faster. Interestingly, the model without the residual function performed worse by both metrics with SSIM at 12.5% lower and LPIPS at 37% higher. These scores justified the use of the model with residuals and trained the fixed images for further experiments. The model was then trained an additional 800 epochs on same training set of fixed image data which achieved an improvement of 20% on the loss, 11.8% increase in SSIM score, and a 29.2% reduction in LPIPS score. Further training is possible, but we were constrained by time as each set of 800 epochs of training required around 12 hours. The drug treatment results both had poor SSIM score due to the lack of artifact removal, but their LPIPS scores remained low, which agrees with a visual inspection of the images. Due to the worse scores, we decided to train the model on the Taxol 50nM images for 200 additional epochs and achieved SSIM and LPIPS scores that were near the control group. This shows that if the model is having difficulties with new information, additional training can be the solution.

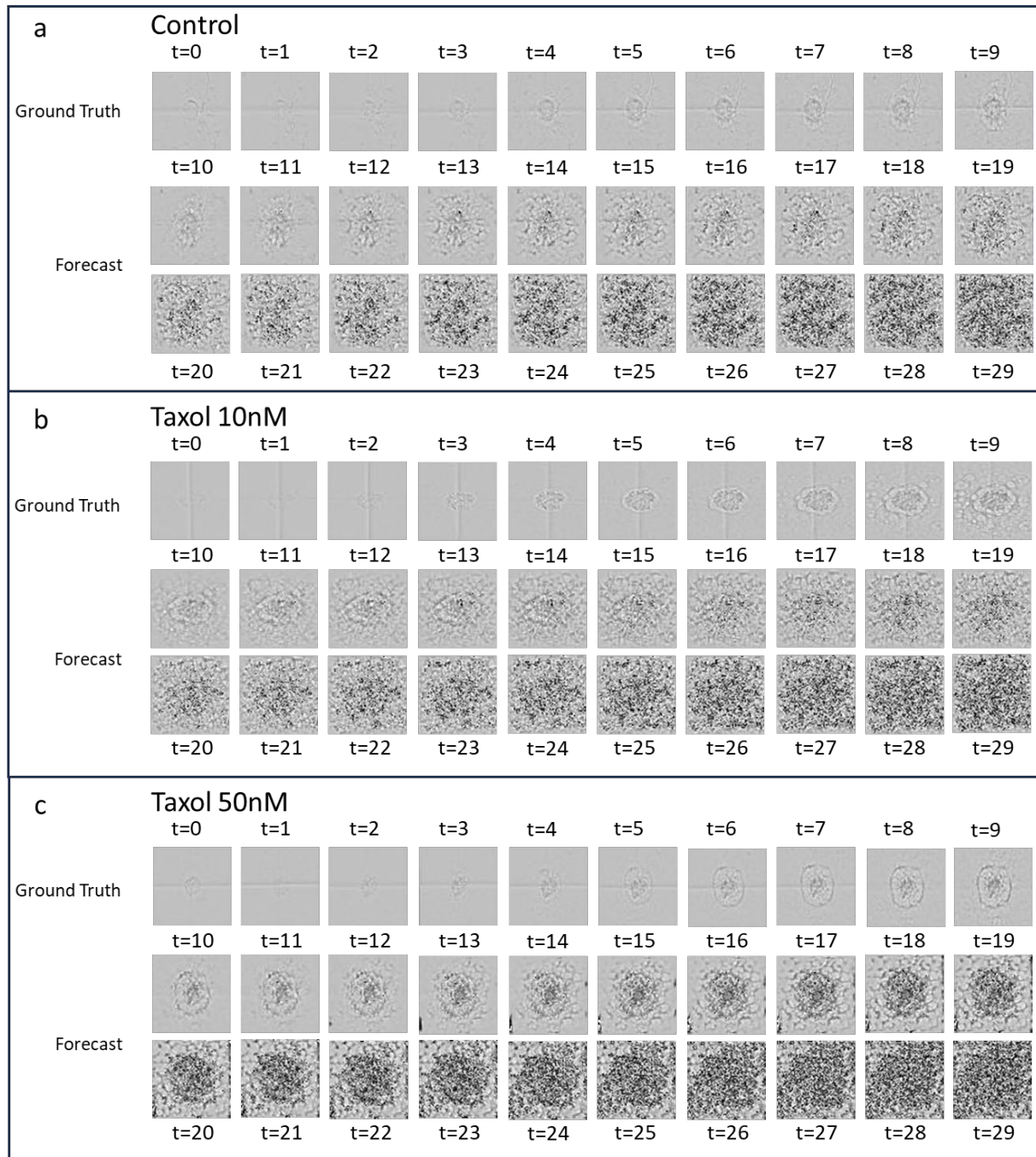
Parameters	Original Images	Lighting Normalized	Fixed Images	No Residual Function
<b>Loss</b>	0.041	0.045	0.015	0.012
<b>SSIM</b>	0.492	0.274	0.727	0.637
<b>LPIPS</b>	0.290	0.216	0.065	0.089
<b>Epochs</b>	800	800	800	1000
	Fixed Control	Taxol 10nM	Taxol 50nM	Taxol 50nM Retrain
<b>Loss</b>	0.012	0.012	0.012	0.012
<b>SSIM</b>	0.813	0.582	0.626	0.818
<b>LPIPS</b>	0.046	0.079	0.087	0.065
<b>Epochs</b>	1600	1600	1600	1600+200

**Table 2. Comparison of SSIM and LPIPS scores by data preparation, residuals, and training epochs.** The model loss is the average of the mean square and mean absolute errors when comparing the generated images to the training dataset images after the listed number of training epochs, with a lower loss denoting better performance. Structural Similarity (SSIM) index compares the luminance, contrast, and structural information of the reference image (the validation cancer outgrowth image) with the generated image (the model produced image for the same day of cancer outgrowth) and then gives a score, with a higher score denoting better performance. Learned Perceptual Image Patch Similarity (LPIPS) calculates the perceptual similarity between the two images based on distance between features generated by a separate network, VGGNet. Original images are those that have only been downsized to 64x64 pixels for training. Lighting Normalized images are those that have had the gaussian blur function applied in addition. The fixed images dataset includes all changes described in the methods section. Creating a residual function is a simple technique for LSTMs that involves adding the original image to the output of the hidden state before computing the loss which forces the models to learn the differences between the two images instead of learning the entirety of the new image. The control, Taxol 10nM, and Taxol 50nM conditions at 1600 epochs were run on the same model as the fixed image model, after it was trained for twice as long. The last category of Fixed Taxol 50nM shows the evaluation of the Taxol 50nM Day 9 image after training the 1600 epoch original model for an additional 200 epochs on a training subset of Taxol 50nM images.

#### *H460 forecasted images at 64x64 pixels*

The next experiment was to see how many days the forecasting could show before the cancer area is assumed to expand to the entire image window. In Figure 5 we show the forecasting results of the 1600 fixed model using the Control and Taxol 10nM datasets and can compare with the 1600+200 fixed and retrained model on Taxol 50nM condition forecasting. The forecasting

appears to continue with a reasonable shape compared to the ground truth for about 12-13 additional images in all the forecasting sequences. After  $t=23-24$ , the images become increasingly fuzzier until the black pixels expand to fill the entire frame. The control model performs slightly better on the control forecasting than the Taxol 10nM forecasting with some blurriness affecting the Taxol 10nM images 3-4 days earlier than the control. The retraining allows the Taxol 50nM images to stay sharper during forecasting for about as long as the control images. The forecasting model appears to be able to learn some information about the satellite cancer cell formations as the growth appears fully around each initial tumor starting and maintains similar curved patterns to those areas nearby. Also, the Taxol 50nM model appears to learn the slower migration of the drug treated cells and more heavily darkens the center compared to the spreading growth of both the control and Taxol 10nM conditions.



The area of cancer growth was measured by summing the area of dark pixels over the entire range of 30 days, and then extrapolation curves were fit to the ground truth data to compare the forecasting accuracy, seen in Figure 5. The control condition maintains about 2-3 days of growth at about the same rate as the ground truth and then continues to follow a more linear pattern. The Taxol 10nM condition immediately follows a linear pattern and deviates from the area forecast significantly. Likely, additional training could help both models with better forecasting. The Taxol 50nM condition fit best with a square polynomial extrapolation, and the forecasting model closely matched this curve for about 10 days until it forecast a slowing in the rate of growth. The model could, at this point, be better at forecasting slower growth rates which is why the Taxol 50nM condition happened to fit the forecasting much more closely than the other conditions.

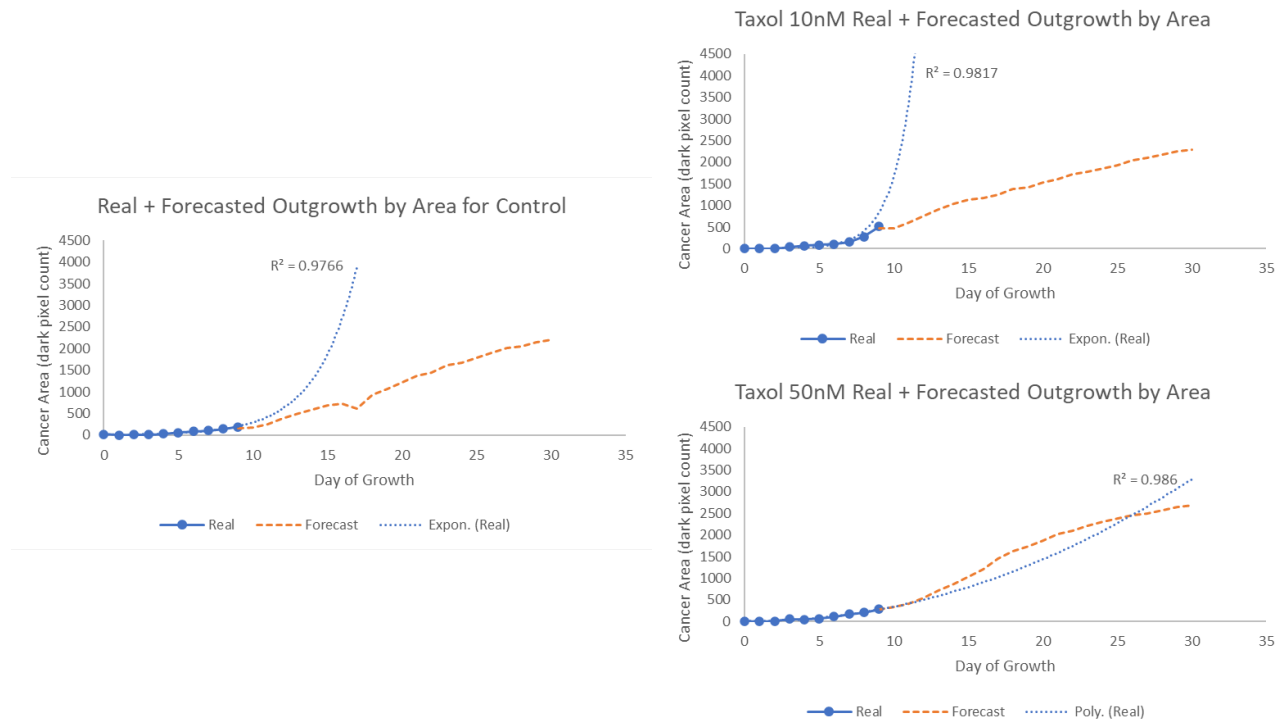


**Figure 5. Estimated cancer area growth for control, Taxol 10nM, and Taxol 50nM by dark pixel count.** The cancer outgrowth was measured by thresholding the ground truth and forecasted images to consider only the darkest pixels and then summing the area of those pixels. The blue line is the ground truth data, and the dotted orange line is the forecasted image data. Exponential curves were used to extrapolate the control and Taxol 10nM condition ground truth data, but a

polynomial square extrapolation fit best for the Taxol 50nM condition rather than exponential or linear.  $R^2$  value is in comparison to ground truth data.

### *Forecasting upscaled from 64x64 pixel trained model to 512x512 pixel images*

The last experiment was to determine if the 64x64 pixel trained model could extrapolate up to a larger image size for better visual clarity in the cancer outgrowth forecasting. The 512x512 pixel resized images were run through the model in the same manner as the 64x64 pixel images. The control and Taxol 10nM conditions used the 1600 epoch fixed image model and the Taxol 50nM condition used the 1600 + 200 epoch fixed image model retrained on the Taxol 50nM images. The results in Figure 6 show that after the ground truth Day 9 image, the control, Taxol 10nM, and Taxol 50nM models all forecast Day 10 with a lightening of the outer areas and a darkening of the denser cancer clusters in the main tumor center. Immediately after, the Day 11 forecast begins to introduce a fuzzy texture across the entire image and continues darkening the denser cancer clusters in the center. After this, the image quality continues to become more and more fuzzy until the image fades into a roughly uniform pattern. Clearly the features that are learned on the small scale cannot fully translate up to the larger image size, and so the best results would be obtained from training a model on as high of resolution images as is possible. In our case, the computer power available did not have enough GPU RAM to run any images sized larger than 64x64 pixels without sacrificing much of the convLSTM architecture.

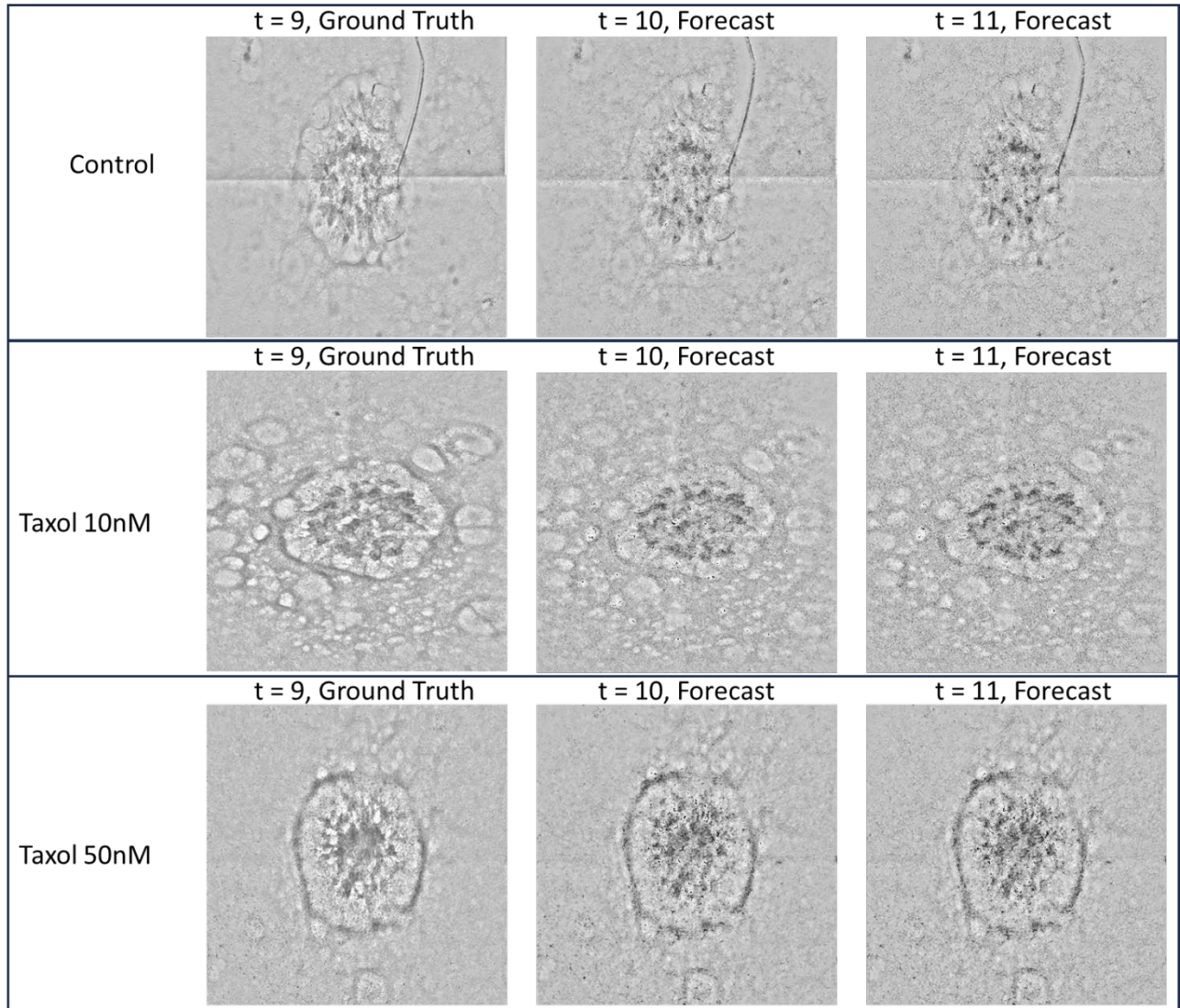


**Figure 6. Forecast 512x512 pixel images.** Day 9 is the ground truth image while Day 10, and Day 11 are model forecast images generated from the models trained on 64x64 pixel images. Control and Taxol 10nM forecast was run on the 1600 epoch fixed image model while the Taxol 50nM forecast was run on the 1600 + 200 epoch fixed model retrained on the Taxol 50nM images.

### Discussion

There are several papers on different forms of neural network architectures, usually some form of convLSTM with different modifications, but these researchers mostly study the effectiveness of these models on benchmark datasets that contain highly curated and specific datasets [24,25,26].

The challenges seen by researchers applying convLSTM to oncology applications include tiny datasets of 33 patients for tumor volume and growth prediction [19] and a very short forecasting

time of 500ms for tumor movement during MRI guided radiotherapy [27]. Part of these problems stem from the inherently messy nature of biological data and from the small sample sizes present in patient datasets since geography, privacy, and occurrence all get in the way of data collection. The present study demonstrates that in vitro models can provide curated datasets in quantities that are preferable for machine learning methods while also framing the problem in way that is easier for machines to glean information from.

Data preparation is the main method that researchers can use that improves the chances for success regarding machine learning models are learning the critical features of their data. The fact that there are papers being written to be guides and learning tools to help expand the machine learning applications for cancer analysis is a good sign for the future of cancer research [20,21,28]. From the data preparation part of this study, looking at all pieces of data after any change or transformations was applied turned out to be crucial to getting forecasting results. The resize function performed well in our initial 512x512 pixel downsize but caused some instances of severe digitization and/or unreadable images when further downsizing to 64x64 pixels and is the major reason the lighting normalization model performed significantly worse than the any other model. Additionally, we needed to remove the black and white bars left over from stitching and cropping because they were biasing the resulting overall image brightness during the gaussian blur averaging and causing learning issues when the bars would randomly appear and disappear within a sequence. Static artifacts such as superficial scratches that the cells could clearly grow over were less of a problem since the model would learn to remember its position and hold it in place throughout a forecast sequence.

There are currently no other papers forecasting accelerated cancer outgrowth in vitro, and so there is a lot of room for improvement and iteration on our model to help with lung cancer forecasting

and lung cancer drug treatment forecasting. The most effective forecasting model presented in this paper was the Taxol 50nM forecast, which most closely followed the extrapolated cancer growth curve. The images also appeared to forecast satellite growths of migrating lung cancer cells at a distance from the main tumor mass. These features are promising, as they show that the model could be used for the evaluation of therapeutic impacts on lung cancer in a matter of 9 days of incubation with the desired drug treatments. To improve upon the model, we will continue to gather more data and train the model until convergence instead of to an arbitrary epoch count. With better computing resources this will be feasible as streaming resources from Google Collaboratory comes with the problem of disconnecting, software errors on the host side, and extra time involved with adapting code to work on their platform. Another experiment to perform is to increase the training image resolution but limit the forecasting to a few days to maintain forecast image quality. These new images could be saved and then used to further train the model to extend the training sequence length with the goal of forecasting much further than just 10 to 20 days in the future.

In conclusion, the results show that forecasting accelerated cancer outgrowth over fibroblasts and drug effects on said outgrowth are both feasible when taking advantage of convLSTM machine learning.

### **Acknowledgements**

We would like to acknowledge the University of Texas at Arlington for facility support and Google Collaboratory for use of their computing power to train the models.

### **Author Contributions**

Y.T.K. was the principal investigator. A.A.G. wrote the paper. Y.T.K. and A.A.G. developed the idea and designed the experiments. J.A.S. coded the neural network and performed the data

preparation. A.A.G and J.A.S. troubleshot and trained the neural network. Y.T.K, A.A.G., A.C., G.F., A.C., S.K., and B.G. carried out the experiments and provided the data.

## References

1. Siegel, R. L., Miller, K. D., Wagle, N. S., & Jemal, A. (2023). Cancer statistics, 2023. *CA: A Cancer Journal for Clinicians*, 73(1), 17–48. <https://doi.org/10.3322/caac.21763>
2. Nicholson, A. G., Tsao, M. S., Beasley, M. B., Borczuk, A. C., Brambilla, E., Cooper, W. A., Dacic, S., Jain, D., Kerr, K. M., Lantuejoul, S., Noguchi, M., Papotti, M., Rekhtman, N., Scagliotti, G., van Schil, P., Sholl, L., Yatabe, Y., Yoshida, A., & Travis, W. D. (2022). The 2021 WHO Classification of Lung Tumors: Impact of Advances Since 2015. In *Journal of Thoracic Oncology* (Vol. 17, Issue 3, pp. 362–387). Elsevier Inc. <https://doi.org/10.1016/j.jtho.2021.11.003>
3. Modi P, Uppe A. Lung Biopsy Techniques and Clinical Significance. [Updated 2022 Jun 28]. In: StatPearls [Internet]. Treasure Island (FL): StatPearls Publishing; 2023 Jan-. Available from: <https://www.ncbi.nlm.nih.gov/books/NBK563153/>
4. Ofiara, L. M., Navasakulpong, A., Beaudoin, S., & Gonzalez, A. v. (2014). Optimizing tissue sampling for the diagnosis, subtyping and molecular analysis of lung cancer. In *Frontiers in Oncology* (Vol. 4, Issue SEP). Frontiers Research Foundation. <https://doi.org/10.3389/fonc.2014.00253>
5. Kage, H., Kohsaka, S., Shinozaki-Ushiku, A., Hiraishi, Y., Sato, J., Nagayama, K., Ushiku, T., Takai, D., Nakajima, J., Miyagawa, K., Aburatani, H., Mano, H., & Nagase, T. (2019). Small lung tumor biopsy samples are feasible for high quality targeted next generation sequencing. *Cancer Science*, 110(8), 2652–2657. <https://doi.org/10.1111/cas.14112>
6. Zhang, F., & MacRae, D. A. (2021). Application of machine learning in CT images and X-rays of COVID-19 pneumonia. In *Medicine (United States)* (Vol. 100, Issue 36, p. E26855). Lippincott Williams and Wilkins. <https://doi.org/10.1097/MD.00000000000026855>
7. Chen, J., Li, Y., Guo, L., Zhou, X., Zhu, Y., He, Q., Han, H., & Feng, Q. (2022). Machine learning techniques for CT imaging diagnosis of novel coronavirus pneumonia: a review. *Neural Computing and Applications*. <https://doi.org/10.1007/s00521-022-07709-0>
8. Akinci D'Antonoli, Tugba et al. (2020). CT Radiomics Signature of Tumor and Peritumoral Lung Parenchyma to Predict Non-small Cell Lung Cancer Postsurgical Recurrence Risk. *Academic Radiology*, Volume 27, Issue 4, 497 – 507. <https://doi.org/10.1016/j.acra.2019.05.019>
9. Lee, J., Li, B., Cui, Y., Sun, X., Wu, J., Zhu, H., Yu, J., Gensheimer, M.F., Loo, B.W., Jr., Diehn, M., Li, R. (2018). A Quantitative CT Imaging Signature Predicts Survival and Complements Established Prognosticators in Stage I Non-Small Cell Lung Cancer. *International Journal of Radiation Oncology, Biology, Physics*, 102(4), (1098-1106). <https://doi.org/10.1016/j.ijrobp.2018.01.006>
10. Jacobs, C., Setio, A. A. A., Scholten, E. T., Gerke, P. K., Bhattacharya, H., Hoesein, F. A. M., Brink, M., Ranschaert, E., de Jong, P. A., Silva, M., Geurts, B., Chung, K., Schalekamp, S., Meersschaert, J., Devaraj, A., Pinsky, P. F., Lam, S. C., van Ginneken, B., & Farahani, K. (2021). Deep learning for lung cancer detection on screening ct scans:

- Results of a large-scale public competition and an observer study with 11 radiologists. *Radiology: Artificial Intelligence*, 3(6). <https://doi.org/10.1148/ryai.2021210027>
11. Partin, A., Brettin, T. S., Zhu, Y., Narykov, O., Clyde, A., Overbeek, J., & Stevens, R. L. (2023). Deep learning methods for drug response prediction in cancer: Predominant and emerging trends. *Frontiers in Medicine*, 10. <https://doi.org/10.3389/fmed.2023.1086097>
  12. Qureshi, R., Basit, S. A., Shamsi, J. A., Fan, X., Nawaz, M., Yan, H., & Alam, T. (2022). Machine learning based personalized drug response prediction for lung cancer patients. *Scientific Reports*, 12(1). <https://doi.org/10.1038/s41598-022-23649-0>
  13. Huang, R. X., Siriwanna, D., Cho, W. C., Wan, T. K., Du, Y. R., Bennett, A. N., He, Q. E., Liu, J. D., Huang, X. T., & Chan, K. H. K. (2022). Lung adenocarcinoma-related target gene prediction and drug repositioning. *Frontiers in Pharmacology*, 13. <https://doi.org/10.3389/fphar.2022.936758>
  14. Luo R, Song J, Xiao X, Xie Z, Zhao Z, Zhang W, Miao S, Tang Y, Ran L. Identifying CpG methylation signature as a promising biomarker for recurrence and immunotherapy in non-small-cell lung carcinoma. *Aging (Albany NY)*. 2020 Jul 28;12(14):14649-14676. doi: 10.18632/aging.103517. Epub 2020 Jul 28. PMID: 32723974; PMCID: PMC7425482.
  15. Gao, Q., Yang, L., Lu, M., Jin, R., Ye, H., & Ma, T. (2023). The artificial intelligence and machine learning in lung cancer immunotherapy. In *Journal of Hematology and Oncology* (Vol. 16, Issue 1). BioMed Central Ltd. <https://doi.org/10.1186/s13045-023-01456-y>
  16. Xu, Y., Hosny, A., Zeleznik, R., Parmar, C., Coroller, T., Franco, I., Mak, R. H., & Aerts, H. J. W. L. (2019). Deep learning predicts lung cancer treatment response from serial medical imaging. *Clinical Cancer Research*, 25(11), 3266–3275. <https://doi.org/10.1158/1078-0432.CCR-18-2495>
  17. Jakobsen, E., Olsen, K. E., Bliddal, M., Hornbak, M., Persson, G. F., & Green, A. (2021). Forecasting lung cancer incidence, mortality, and prevalence to year 2030. *BMC Cancer*, 21(1). <https://doi.org/10.1186/s12885-021-08696-6>
  18. Fertig, E. J., Jaffee, E. M., Macklin, P., Stearns, V., & Wang, C. (2021). Forecasting cancer: from precision to predictive medicine. *Med*, 2(9), 1004–1010. <https://doi.org/10.1016/j.medj.2021.08.007>
  19. Zhang, L., Lu, L., Wang, X., Zhu, R. M., Bagheri, M., Summers, R. M., & Yao, J. (2020). Spatio-Temporal Convolutional LSTMs for Tumor Growth Prediction by Learning 4D Longitudinal Patient Data. *IEEE Transactions on Medical Imaging*, 39(4), 1114–1126. <https://doi.org/10.1109/TMI.2019.2943841>
  20. Diaz, O., Kushibar, K., Osuala, R., Linardos, A., Garrucho, L., Igual, L., Radeva, P., Prior, F., Gkontra, P., & Lekadir, K. (2021). Data preparation for artificial intelligence in medical imaging: A comprehensive guide to open-access platforms and tools. *Physica Medica*, 83, 25–37. <https://doi.org/10.1016/j.ejmp.2021.02.007>
  21. Willeminck, M. J., Koszek, W. A., Hardell, C., Wu, J., Fleischmann, D., Harvey, H., Folio, L. R., Summers, R. M., Rubin, D. L., & Lungren, M. P. (2020). Preparing medical imaging data for machine learning. In *Radiology* (Vol. 295, Issue 1, pp. 4–15). Radiological Society of North America Inc. <https://doi.org/10.1148/radiol.2020192224>
  22. Germain, A., Young-Tae, K. Co-culture device for in vitro high throughput analysis of cancer associated fibroblast and cancer cell interactions. *Oncology*. DOI: 10.1159/000533773

23. Preibisch, S., Saalfeld, S., & Tomancak, P. (2009). Globally optimal stitching of tiled 3D microscopic image acquisitions. *Bioinformatics*, 25(11), 1463–1465.
24. Su, J., Byeon, W., Kossaifi, J., Huang, F., Kautz, J., & Anandkumar, A. (2020). Convolutional Tensor-Train LSTM for Spatio-Temporal Learning. *Advances in Neural Information Processing Systems*, 33, 13714-13726.  
[https://proceedings.neurips.cc/paper\\_files/paper/2020/file/9e1a36515d6704d7eb7a30d783400e5d-Paper.pdf](https://proceedings.neurips.cc/paper_files/paper/2020/file/9e1a36515d6704d7eb7a30d783400e5d-Paper.pdf)
25. Desai, P., Sujatha, C., Chakraborty, S., Ansuman, S., Bhandari, S., & Kardiguddi, S. (2022). Next frame prediction using ConvLSTM. *Journal of Physics: Conference Series*, 2161(1). <https://doi.org/10.1088/1742-6596/2161/1/012024>
26. Zhou, Y., Dong, H., & el Saddik, A. (2020). Deep Learning in Next-Frame Prediction: A Benchmark Review. In *IEEE Access* (Vol. 8, pp. 69273–69283). Institute of Electrical and Electronics Engineers Inc. <https://doi.org/10.1109/ACCESS.2020.2987281>
27. Lombardo, E., Rabe, M., Xiong, Y., Nierer, L., Cusumano, D., Placidi, L., Boldrini, L., Corradini, S., Niyazi, M., Reiner, M., Belka, C., Kurz, C., Riboldi, M., Landry, G. (2023). Evaluation of real-time tumor contour prediction using LSTM networks for MR-guided radiotherapy. *Radiotherapy and Oncology*, 182.  
<https://doi.org/10.1016/j.radonc.2023.109555>
28. Wang, J., Sourlos, N., Zheng, S., van der Velden, N., Pelgrim, G. J., Vliegthart, R., & van Ooijen, P. (2023). Preparing CT imaging datasets for deep learning in lung nodule analysis: Insights from four well-known datasets. *Heliyon*, 9(6).  
<https://doi.org/10.1016/j.heliyon.2023.e17104>

## Chapter 5: Conclusions and Future Works

In vitro studies need to mimic in vivo conditions more than ever to increase the relevance of their results [1,2]. The move from 2D to 3D models is an important leap, but 3D models are much more challenging to cultivate and gain information [3,4,5]. Creating 2D devices still has its place in research if they are improving the complexity of the system and maintaining the ease of use and analysis. It is important to select an appropriate cell type to co-culture with the lung cancer cells to gain the most from the combination. Fibroblasts co-cultured with lung cancer cells directly influence their development, growth, and resistance to anti-cancer therapies and are an impactful partner when they become cancer-associated fibroblasts [6,7,8]. Besides discovering therapeutics for lung cancer, classification of the patient's lung cancer subtype is particularly important [9]. For classification, biopsies allow for direct harvesting of lung cancer tissue, but many patients receive only 46% of patients receive more than 2 biopsies with a diagnosis delay of nearly two months [10]. Therefore, biopsies efficiency can be improved by creating a more definitive lung cancer classification method. AI can help improve the subtyping of lung cancer by running large amounts of image data through CNNs that can learn features and trends in the images that are unlikely to be noticed by the human eye and more accurately predict a lung cancer subtype [11,12]. Once the patient's lung cancer is classified, it is necessary to select a treatment regime that best suits the situation. Models are being developed for prediction of cancer recurrence after various treatments such as radiotherapy and immunotherapy [13,14,15], but these lack any fine prediction for how fast and aggressively the lung cancer will recur, or if it will slowly decline over time. Developing in vitro techniques that can supplement clinical pathology is important for increasing the accuracy of classification, rapidly expanding the possible treatments for lung cancer, and forecasting therapeutic effects upon patients.

In Chapter 2, we produced devices that are printable by an off-the-shelf stereolithography 3D printer that hold magnets underneath standard size well plates to secure metallic tubes inside the wells and create an island of lung cancer among fibroblasts. Based on these studies, we noted the increased growth effects of fibroblasts on H460 lung cancer cells, demonstrating the value of these co-cultures for accelerated studies. Additionally, we performed a drug study with some common chemotherapeutics where we could calculate a comparative viability for the H460 lung cancer, and we could observe the effects that the various drugs had on the morphology of both cell lines and their resulting growth pattern differences. The broad approach of being testing therapeutics on two cell lines at the same time in addition to quantitative and qualitative analysis brings together some of the benefits of more complex lung cancer studies with the ease of analysis that the 2D studies tend to have. The experimental set up can possibly be improved by adding extra-cellular matrix (ECM) for the study of targeted treatments for the metastasis proteins that help degrade their environment, such as matrix metalloproteinases (MMPs). Additionally, fluorescently transfected cell lines are better for longer analysis if therapeutic studies farther than 72 hours are desired.

In Chapter 3, we are the first group to train a CNN model on in vitro time series images containing lung cancer outgrowth over fibroblasts with two different lung cancer cell lines, H460 (large cell carcinoma) and A549 (squamous cell carcinoma), that is capable of distinguishing between them 100% of the time at only 2 days of growth and 25 epochs of training. Our hypothesis was that the longer that each cell line grew, the model might have a greater accuracy for classification, but the model maintained a 90% or greater accuracy after the first day of growth. The study shows that a look at the macro-growth patterns could be a novel method of differentiating between different cancer cell subtypes or even cell lines. For this study, we need to expand the training lung cancer cell lines to cover at least all of the major subtypes of lung cancer including, adenocarcinoma,

small cell lung cancer, and mixed small cell lung cancer and then the model needs to be validated on patient samples with known subtype classifications to determine its applicability to a clinical setting. On top of this, the initial seeding is 5000 cancer cells per well, and we would need to tune this number with realistic numbers obtainable from biopsy samples or correlate the samples with a smaller number of starting cells with different days of growth with respect to the model.

In Chapter 4, we are the first group to develop an in vitro method of mass data collection for time series lung cancer growth that facilitated the creation of a convLSTM algorithm that is capable of forecasting lung cancer outgrowth over fibroblasts in control and drug conditions. The model was examined by the comparison of images to ground truth images and the similarity scores of SSIM and LPIPS were quite good. Currently, the forecast model is trained on the first 9 days of cancer outgrowth and accurately produces images 5 days into the future for control and 10 days into the future for the Taxol 50nM condition, with the accuracy based on the extrapolation curves of the growth from the first 9 days. Following studies need to increase computing resources for model training so the model can be both trained longer and on higher resolution images. These things should allow for even high image fidelity for the first few days of forecasting. These new images can then be saved, the model can be retrained on them, and more images can be forecast farther into the future. The model can be improved by gathering more input data and being more thorough with the artifact removal. While we removed most of the artifacts, there were still some images with black bars, bubbles, debris, and scratches that may have impacted the outgrowth forecasts.

Neural Networks are valuable for many forms of lung cancer analysis due to their ability to uncover and learn trends in vast datasets that humans are unable to learn [16,17]. Machine learning output quality is entirely dependent on the quality of the input data so framing a problem with a machine learning friendly dataset and being thorough with data preparation helps results be more reliable

[18]. The proposed models can even be expanded further to improve cancer treatments and diagnosis. The selection of the co-culture healthy cell type of fibroblasts suited the initial needs of the study but could include lung epithelial cells, endothelial cells, and macrophages among other cell types found in the lungs since they all play a different role and/or overlapping roles with each other [19]. While studying more co-culture cells, 3D growth can even be modeled as the convLSTM can handle slices of a 3D image to create a reconstructed tumor shape and volume [20]. Through a combination of one of the various organoid co-culture methods and the convLSTM, the in vitro forecasting could be taken to the point of very closely mimicking in vivo conditions. These many and varied machine learning models will significantly improve lung cancer classification and treatment regimens as the datasets grow larger and as researchers continue to learn how to best utilize these tools for diagnosis, prediction, and forecasting. Adapting the both the method of study and the machine learning algorithms is where bioengineering researchers can shine and fill in gaps in the current research space.

## References

1. Long, Y., Xie, B., Shen, H. C., & Wen, D. (2022). Translation Potential and Challenges of In Vitro and Murine Models in Cancer Clinic. In *Cells* (Vol. 11, Issue 23). MDPI. <https://doi.org/10.3390/cells11233868>
2. Manduca, N., Maccafeo, E., de Maria, R., Sistigu, A., & Musella, M. (2023). 3D cancer models: One step closer to in vitro human studies. In *Frontiers in Immunology* (Vol. 14). Frontiers Media S.A. <https://doi.org/10.3389/fimmu.2023.1175503>
3. van Zundert, I., Fortuni, B., & Rocha, S. (2020). From 2d to 3d cancer cell models—the enigmas of drug delivery research. In *Nanomaterials* (Vol. 10, Issue 11, pp. 1–30). MDPI AG. <https://doi.org/10.3390/nano10112236>
4. Abbas, Z. N., Al-Saffar, A. Z., Jasim, S. M., & Sulaiman, G. M. (2023). Comparative analysis between 2D and 3D colorectal cancer culture models for insights into cellular morphological and transcriptomic variations. *Scientific Reports*, *13*(1). <https://doi.org/10.1038/s41598-023-45144-w>

5. Jensen, C., & Teng, Y. (2020). Is It Time to Start Transitioning From 2D to 3D Cell Culture? In *Frontiers in Molecular Biosciences* (Vol. 7). Frontiers Media S.A. <https://doi.org/10.3389/fmolb.2020.00033>
6. Movia, D., Bazou, D., & Prina-Mello, A. (2019). ALI multilayered co-cultures mimic biochemical mechanisms of the cancer cell-fibroblast cross-talk involved in NSCLC MultiDrug Resistance. *BMC Cancer*, *19*(1). <https://doi.org/10.1186/s12885-019-6038-x>
7. Majety, M., Pradel, L. P., Gies, M., & Ries, C. H. (2015). Fibroblasts influence survival and therapeutic response in a 3D co-culture model. *PLoS ONE*, *10*(6), 1–18. <https://doi.org/10.1371/journal.pone.0127948>
8. Cruz-Bermúdez, A., Laza-Briviesca, R., Vicente-Blanco, R. J., García-Grande, A., Coronado, M. J., Laine-Menéndez, S., Alfaro, C., Sanchez, J. C., Franco, F., Calvo, V., Romero, A., Martin-Acosta, P., Salas, C., Garcia, J. M., & Provencio, M. (2019). Cancer-associated fibroblasts modify lung cancer metabolism involving ROS and TGF- $\beta$  signaling. *Free Radical Biology and Medicine*, *130*, 163–173. <https://doi.org/10.1016/j.freeradbiomed.2018.10.450>
9. Nicholson, A. G., Tsao, M. S., Beasley, M. B., Borczuk, A. C., Brambilla, E., Cooper, W. A., Dacic, S., Jain, D., Kerr, K. M., Lantuejoul, S., Noguchi, M., Papotti, M., Rekhman, N., Scagliotti, G., van Schil, P., Sholl, L., Yatabe, Y., Yoshida, A., & Travis, W. D. (2022). The 2021 WHO Classification of Lung Tumors: Impact of Advances Since 2015. In *Journal of Thoracic Oncology* (Vol. 17, Issue 3, pp. 362–387). Elsevier Inc. <https://doi.org/10.1016/j.jtho.2021.11.003>
10. Zhang, Y., Shi, L., Simoff, M. J., Wagner, O. J., & Lavin, J. (2020). Biopsy frequency and complications among lung cancer patients in the United States. *Lung Cancer Management*, *9*(4). <https://doi.org/10.2217/lmt-2020-0022>
11. Pfeffer, M. A., & Ling, S. H. (2022). Evolving Optimised Convolutional Neural Networks for Lung Cancer Classification. *Signals*, *3*(2), 284–295. <https://doi.org/10.3390/signals3020018>
12. Humayun, M., Sujatha, R., Almuayqil, S. N., & Jhanjhi, N. Z. (2022). A Transfer Learning Approach with a Convolutional Neural Network for the Classification of Lung Carcinoma. *Healthcare (Switzerland)*, *10*(6). <https://doi.org/10.3390/healthcare10061058>
13. Hindocha, S., Charlton, T. G., Linton-Reid, K., Hunter, B., Chan, C., Ahmed, M., Robinson, E. J., Orton, M., Ahmad, S., McDonald, F., Locke, I., Power, D., Blackledge, M., Lee, R. W., & Aboagye, E. O. (2022). A comparison of machine learning methods for predicting recurrence and death after curative-intent radiotherapy for non-small cell lung cancer: Development and validation of multivariable clinical prediction models. *EBioMedicine*, *77*, 103911. <https://doi.org/10.1016/j>
14. Li, Y., Brendel, M., Wu, N., Ge, W., Zhang, H., Rietschel, P., Quek, R. G. W., Pouliot, J. F., Wang, F., & Harnett, J. (2022). Machine learning models for identifying predictors of clinical outcomes with first-line immune checkpoint inhibitor therapy in advanced non-small cell lung cancer. *Scientific Reports*, *12*(1). <https://doi.org/10.1038/s41598-022-20061-6>
15. Kong, F., Yang, H., Wang, Q., Wei, Z., & Ye, X. (2023). A prognostic model for predicting progression-free survival in patients with advanced non-small cell lung cancer after image-guided microwave ablation plus chemotherapy. *European Radiology*, *33*(11), 7438–7449. <https://doi.org/10.1007/s00330-023-09804-9>

16. Tran, K. A., Kondrashova, O., Bradley, A., Williams, E. D., Pearson, J. v., & Waddell, N. (2021). Deep learning in cancer diagnosis, prognosis and treatment selection. In *Genome Medicine* (Vol. 13, Issue 1). BioMed Central Ltd. <https://doi.org/10.1186/s13073-021-00968-x>
17. Bhinder, B., Gilvary, C., Madhukar, N. S., & Elemento, O. (2021). Artificial intelligence in cancer research and precision medicine. In *Cancer Discovery* (Vol. 11, Issue 4, pp. 900–915). American Association for Cancer Research Inc. <https://doi.org/10.1158/2159-8290.CD-21-0090>
18. Koçak, B., Cuocolo, R., dos Santos, D. P., Stanzione, A., & Ugga, L. (2023). Must-have Qualities of Clinical Research on Artificial Intelligence and Machine Learning. In *Balkan Medical Journal* (Vol. 40, Issue 1, pp. 3–12). Galenos Publishing House. <https://doi.org/10.4274/balkanmedj.galenos.2022.2022-11-51>
19. Alfaro-Moreno, E., Nawrot, T. S., Vanaudenaerde, B. M., Hoylaerts, M. F., Vanoirbeek, J. A., Nemery, B., & Hoet, P. H. M. (2008). Co-cultures of multiple cell types mimic pulmonary cell communication in response to urban PM10. *European Respiratory Journal*, 32(5), 1184–1194. <https://doi.org/10.1183/09031936.00044008>
20. Zhang, L., Lu, L., Wang, X., Zhu, R. M., Bagheri, M., Summers, R. M., & Yao, J. (2020). Spatio-Temporal Convolutional LSTMs for Tumor Growth Prediction by Learning 4D Longitudinal Patient Data. *IEEE Transactions on Medical Imaging*, 39(4), 1114–1126. <https://doi.org/10.1109/TMI.2019.2943841>